



# Single shot ablation of monolayer graphene by spatially shaped femtosecond laser pulses

Abel Gil Villalba

## ► To cite this version:

Abel Gil Villalba. Single shot ablation of monolayer graphene by spatially shaped femtosecond laser pulses. Optics / Photonics. Université Bourgogne Franche-Comté, 2017. English. NNT : 2017UBFCD028 . tel-01816952

**HAL Id: tel-01816952**

**<https://theses.hal.science/tel-01816952>**

Submitted on 15 Jun 2018

**HAL** is a multi-disciplinary open access archive for the deposit and dissemination of scientific research documents, whether they are published or not. The documents may come from teaching and research institutions in France or abroad, or from public or private research centers.

L'archive ouverte pluridisciplinaire **HAL**, est destinée au dépôt et à la diffusion de documents scientifiques de niveau recherche, publiés ou non, émanant des établissements d'enseignement et de recherche français ou étrangers, des laboratoires publics ou privés.

# SPIM

## Thèse de Doctorat



école doctorale **sciences pour l'ingénieur et microtechniques**  
UNIVERSITÉ DE FRANCHE-COMTÉ



## Single shot femtosecond laser ablation of graphene

Ablation mono coup du graphène par impulsion laser  
femtoseconde

■ ABEL GIL VILLALBA



# SPIM

## Thèse de Doctorat



école doctorale **sciences pour l'ingénieur et microtechniques**  
UNIVERSITÉ DE FRANCHE-COMTÉ

N° X X X



THÈSE présentée par  
**ABEL GIL VILLALBA**

pour obtenir le  
Grade de Docteur de  
l'Université de Bourgogne Franche-Comté

Spécialité : **Optique**

## Single shot femtosecond laser ablation of graphene

Ablation mono coup du graphène par impulsion laser femtoseconde

Soutenue publiquement le 25 Janvier 2017 devant le Jury composé de :

JAVIER SOLIS	Rapporteur	Professeur, Instituto de Optica Daza de Valdés - Madrid
JEAN-PHILIPPE COLOMBIER	Rapporteur	Maître de conférence, Laboratoire Hubert Curien - St. Etienne
NICOLAS SANNER	Examineur	Maître de conférence, Laboratoire LP3 - Marseille
JOHN DUDLEY	Examineur	Professeur, Institut FEMTO-ST - Besançon
MARIA-PILAR BERNAL-ARTAJONA	Examineur	Directrice de recherche, Institut FEMTO-ST - Besançon
FRANÇOIS COURVOISIER	Directeur de thèse	Chargé de recherche, Institut FEMTO-ST - Besançon





"Experiment is the sole judge of scientific *truth*"

— Richard Feynman

"El ver mucho y leer mucho aviva el ingenio de los hombres"

— Miguel de Cervantes Saavedra

*Un jour cette distance ne sera qu'un lointain souvenir*



# REMERCIEMENTS

With no doubt, this doctoral thesis has been for me a learning process both in the professional and the personal. A process that has been enriched by sharing ideas and doubts with people from different places and cultures, which gave me different points of view as valid or more than mine.

Tout d'abord, un grand merci à François Courvoisier, mon directeur de thèse. Je voudrais mettre l'accent en particulier sur le fait qu'il a toujours voulu me faire confiance, encourageant mes recherches et me permettant de grandir en tant que chercheur scientifique. I really appreciated his patience, motivation, and immense knowledge. His guidance and advices helped me in all the time of research and writing of this thesis as well as in personal issues during this period. It was a pleasure working with him and I could not have imagined having a better advisor and mentor for my Ph.D study.

I thank my fellow labmates for the stimulating discussions, for the endless hours we were working together, and for all the fun we have had in the last three years. I specially would like to thank Luca Furfaro, Chen Xie, Rémi Meyer and Ismail Ouadghiri for their advices and support during all the experimental work, and for all our discussions, sometimes even about work issues !

Living abroad is not always easy but the people I meet during the past three years made me feel always like home, so I would like to thank this 'family' with whom I shared much more than working hours : José Carrión, Yannick Lefier, Antonio Baylón, Jorge Rivero and Stéphane Perrin among others. All of you have been there to support me and share your time with me, either at work, away from the Institut or even running a marathon. I also would like to acknowledge the people from FEMTO-ST Intitut which door was always open for me : Maria-Pilar Bernal, Thibaut Sylvestre, John M. Dudley, Sandrine Quarroz, Valérie Fauvez, ..., as well as the rest of the people from Besançon who welcomed me with open arms : Julien, Mathieu, Ludo, ... (merci pour le cours de français du vendredi soir !)

My gratitude is also extended to Professor Jordi Mompert and Professor Olivier Uteza, which support and confidence in me to become a research scientist was a great boost.

A special thanks to my family. Las palabras no pueden expresar el agradecimiento que siento por mi padre y mi madre, cuyo sacrificio y dedicación han contribuido en gran manera a llevarme hasta aquí. Ellos me inculcaron el valor del esfuerzo, y me enseñaron a tener paciencia y constancia en el trabajo para lograr cualquier meta. Esta tesis doctoral es el resultado final de un viaje que empezó de pequeño con visitas a museos y suscripciones a revistas de divulgación. De igual manera agradecer a mi hermano Sergio su amistad y respeto todo este tiempo, por todos momentos que compartimos ya fuese en la UAB o en el Factory y que siempre llevo conmigo, y especialmente estos ultimos años en los que a pesar de la distancia siempre he tenido su apoyo incondicional.

In final, dar cu siguranță nu în ultimul rând, trebuie să aduc mulțumiri enorme și recunoștința profunda prietenei mele iubite Ingrid, care a fost și este partenerul și sprijinul

meu, care a crezut in mine necondiționat și a crezut ca-mi pot atinge scopul, indiferent de dificultati, care m-a incurajat cu dragostea și optimismul ei.

# SOMMAIRE

<b>Introduction</b>	<b>7</b>
<b>1 Graphene properties and production</b>	<b>11</b>
1.1 Electronic properties . . . . .	11
1.1.1 Tight-binding model . . . . .	12
1.1.2 Massless Dirac fermions in graphene . . . . .	13
1.1.3 Absorption of light . . . . .	14
1.2 Optical properties . . . . .	16
1.2.1 Carrier dynamics . . . . .	17
1.2.1.1 Coulomb-induced carrier dynamics . . . . .	18
1.2.1.2 Phonon-induced carrier dynamics . . . . .	19
1.2.1.3 Coulomb- and phonon-induced carrier dynamics . . . . .	19
1.2.2 Multilayer graphene . . . . .	20
1.3 Mechanical, thermal and chemical properties . . . . .	20
1.3.1 Mechanical properties . . . . .	20
1.3.2 Thermal properties . . . . .	21
1.3.3 Chemical properties . . . . .	21
1.4 Graphene production . . . . .	22
1.4.1 Exfoliation . . . . .	22
1.4.1.1 Scotch tape technique - Micromechanical cleavage . . . . .	22
1.4.1.2 Wedge mechanical exfoliation . . . . .	23
1.4.1.3 Liquid phase exfoliation (LPE) . . . . .	23
1.4.2 Chemical growth methods . . . . .	24
1.4.2.1 Chemical vapour deposition (CVD) . . . . .	24
1.4.2.2 Plasma-enhanced CVD . . . . .	25
1.4.2.3 Reduced graphene oxide . . . . .	26
1.4.2.4 Epitaxial graphene . . . . .	26
1.4.2.5 Molecular beam epitaxy . . . . .	26
1.4.2.6 Conclusions . . . . .	27

1.4.3	Defects in graphene . . . . .	28
1.4.3.1	Zero dimensional defects . . . . .	28
1.4.3.2	One dimensional defects . . . . .	28
1.4.3.3	Defect formation . . . . .	29
1.4.3.4	Grain boundary and diffusion problems . . . . .	30
1.5	Graphene applications . . . . .	31
1.5.1	Photonics and optoelectronics applications . . . . .	31
1.5.1.1	Transparent conductors . . . . .	31
1.5.1.2	Photovoltaic devices . . . . .	31
1.5.1.3	Light-emitting devices . . . . .	31
1.5.1.4	Photodetectors . . . . .	32
1.5.1.5	Saturable absorbers and ultrafast lasers . . . . .	32
1.5.1.6	Touchscreens . . . . .	33
1.5.1.7	Optical limiters . . . . .	34
1.5.1.8	Terahertz devices . . . . .	34
1.5.1.9	Nonlinear frequency conversion . . . . .	34
1.5.2	Energy applications . . . . .	34
1.5.3	Mechanical applications . . . . .	35
1.5.4	Environmental applications . . . . .	35
1.6	Conclusions . . . . .	35
<b>2</b>	<b>Patterning of graphene</b>	<b>37</b>
2.1	Photolithography . . . . .	37
2.2	Electron beam lithography . . . . .	38
2.2.1	Scanning electron microscope followed by reactive ion etching . . . . .	39
2.2.2	Direct etching in transmission electron microscope . . . . .	39
2.3	Focused ion beam . . . . .	40
2.4	Helium ion lithography . . . . .	41
2.5	Direct laser writing . . . . .	42
2.5.1	Laser interference lithography . . . . .	45
2.5.2	Ultrafast laser patterning of graphene . . . . .	46
2.6	Conclusions . . . . .	48
<b>3</b>	<b>Experimental setup</b>	<b>49</b>
3.1	Overview of the setup . . . . .	49
3.2	Femtosecond laser system . . . . .	49

3.3	Laser beam characterization . . . . .	51
3.3.1	Pulse duration characterization . . . . .	51
3.3.2	Beam radius characterization . . . . .	53
3.3.3	Pulse energy characterization . . . . .	54
3.4	Beam shaping . . . . .	55
3.4.1	Spatial light modulator . . . . .	55
3.4.2	Bessel beam . . . . .	57
3.4.3	Hexagonal array beam . . . . .	58
3.5	Quantitative beam characterization . . . . .	62
3.5.1	Imaging of the Bessel beams . . . . .	63
3.5.2	Hexagonal array beam . . . . .	65
3.6	Types of graphene samples . . . . .	66
3.7	Sample positioning . . . . .	66
3.7.1	Hexagonal array beam . . . . .	67
3.7.2	Bessel beam . . . . .	67
3.8	Sample characterization . . . . .	68
3.8.1	Optical microscopy . . . . .	68
3.8.2	Scanning electron microscopy (SEM) . . . . .	69
<b>4</b>	<b>Single shot ultrafast laser ablation of CVD monolayer graphene</b>	<b>71</b>
4.1	Determination of the fluence ablation threshold . . . . .	71
4.1.1	Experimental procedure . . . . .	72
4.1.2	Experimental results . . . . .	73
4.1.2.1	Correlation method . . . . .	73
4.1.2.2	Contour method . . . . .	75
4.2	Deviation from threshold model at sub-micron scale . . . . .	76
4.3	Grain boundaries influence on single shot nanopatterning . . . . .	80
4.3.1	Experimental procedure . . . . .	81
4.3.2	Experimental results . . . . .	82
4.4	Influence of substrate on single shot ablation of CVD graphene . . . . .	84
4.5	Analysis of ablated spot evolution with over-threshold beam diameter . . . . .	86
4.6	External magnetic field effect on monolayer graphene laser patterning . . . . .	88
4.6.1	Magnet description . . . . .	89
4.6.2	Experimental procedure . . . . .	90
4.6.3	Results and conclusions . . . . .	91
4.7	Graphene nanostructuring with higher order Bessel beam . . . . .	94



4.8 Conclusions . . . . .	95
<b>5 Conclusions and perspectives</b>	<b>97</b>

# INTRODUCTION

Since its isolation in 2004 [1], graphene and related materials have attracted tremendous attention for being the base for next generation technologies. We have read in scientific journals that this new material could change our world.

Graphene is a perfect two dimensional (2D) carbon atom sheet. It is the first truly 2D material produced at ambient conditions. In graphene, carbon atoms are arranged in an hexagonal honeycomb lattice. Graphene layers stacked on top of each other form graphite.

The interest in this material is due to its outstanding electrical, mechanical and chemical properties. Graphene is the lightest material known with a weight of around  $0.77 \text{ mg/m}^2$  [2]. Graphene is also the strongest material known, 200 times stronger than similar thickness sheet of steel. It has a very low Joule effect, which means it heats less than other materials when conducting electrons. A large electronic mobility at room temperature has been determined, and ballistic transport covering distances in the range of several micrometers before scattering. Its linear dispersion relation at the Dirac point (where the conduction band and the valence band are in contact) makes it an excellent material to study fundamental physics in lab conditions. It is a transparent, with a linear absorption of 2.3%, zero-gap semiconductor with a tunable bandgap. In addition, graphene flexibility and elasticity make it an ideal candidate for future applications such as wearable devices. After all this amazing characteristics it is astonishing to discover that graphene could be easily produced at home and only in one minute. Surprisingly, the first graphene kit to isolate this material was as simple as a pencil and a scotch tape. However, this method only allowed to produce small random flakes of graphene in the order of tens of microns, and to produce high quality large graphene sheets more complex chemical techniques have been developed.

Although the large-area production of pure monolayer graphene was a serious technological hurdle to advancing graphene technology, nowadays graphene films in the order of  $50 \text{ cm} \times 50 \text{ cm}$  are achievable. A major challenge at the moment is to develop fast low cost techniques to nanopattern graphene, which is necessary for a large number of potential applications.

Graphene is expected to have applications in many different fields. Specially, graphene has potential to revolutionize existing products in the fields of electronics and optoelectronics. Chips, microprocessors and transistors are being created with graphene which duplicate the current speed and capability in half the size. However, these products are not yet being produced on a large scale. Outstanding lighting applications could be developed due to its photosensitivity and high conductivity. These properties turn graphene in a top research material for lighting and organic LED applications. Graphene is shaking up the screens industry for devices, smartphones and flexible OLEDs. Indeed, these past years, the number of patents related to graphene submitted by companies in the sector of screens has increased rapidly. Currently, transparent and flexible screens made from graphene are produced by research groups, so flexible watches and smartphones made from graphene could be a matter of time.

It has also a great potential as a key component in solar cells, and low cost solar cells made from graphene are almost ready to break into market. Graphene will have possible applications in other fields such as coatings, batteries and energy storage, automotive industry or rubber and plastics. In 2014 global market for graphene was \$9 million, most of it in research. Market forecasts speak of an annual growth of 40%, reaching \$220 million by 2026, with the estimation that the largest sectors will be applications in composites, energy applications and graphene coatings [3].

As mentioned above, graphene is a promising material for future technologies. There has been almost only a decade from its discovery, however, there are still several problems to be solved before graphene is present in our daylife. Patterning of graphene at micro- and nanometric scale is required for a large amount of potential applications, from photovoltaics to water filtering.

Ultrafast lasers have the ability to accurately depositing a high energy density in confined regions near the surface of a material over a short time. Laser irradiation inducing changes in local chemistry, local crystal structure and local morphology has been largely reported [4, 5]. Due to the capability of laser to precisely control where in the material and at what rate the energy is deposited, ultrafast lasers have emerged as a powerful tool for fundamental research, but also for industrial applications.

Ultrashort pulses are characterized by a pulse duration in the order of the picoseconds or less ( $< 10^{-12}$  s), allowing to investigate fast-evolving processes in materials and chemical system and to elucidate highly nonlinear processes in atomic, molecular, plasma, and solid-state physics.

Since the first laser material processing experiment in 1967 [7], laser has become a powerful tool in materials processing industry. Laser material processing is based in laser ablation, which is the process of removing a substrate by direct laser energy absorption. Laser ablation onset takes place above a certain fluence threshold which depends on the material properties, microstructure and morphology, the presence of defects, the absorption mechanisms and the laser parameters like wavelength and pulse duration. Various processes can occur during the laser ablation depending on laser processing parameters such as wavelength, fluence or pulse duration. In our research we focused in ultrafast laser ablation, when excitation time is shorter than thermalization time. In this case, direct ionization and formation of dense electron-hole plasma occurs leading to athermal phase changes, direct bond-breaking and explosive disintegration of the lattice due to Coulomb explosion.

Precise laser ablation is achieved by controlling the laser's spatial intensity profile. This precise control allows confinement of the deposited energy to the desired region of the target material. Several methods have been developed to control the spatial intensity profile of the laser beam including selective apertures, multi-apertures beam integrators like micro-lens arrays or field mapping using refractive, reflective or diffractive optics such as spatial light modulators.

In this context, the aim of our research is to determine the possibilities of ultrafast laser patterning of graphene at sub-micron scale.

In the first chapter we introduce the theoretical background on graphene properties, particularly its optical properties, which will mostly rule our experiments. Graphene production techniques developed in the past decade are presented with its advantages and drawbacks with special remark on the generation of graphene defects as a result of production methods.

Chapter 2 gives an overview on the existing methods to pattern graphene available nowadays, with special interest in direct laser patterning, since ultrafast laser offers attractive potential for material processing as mentioned above. The different methods are discussed and their strengths and limitations are exposed together with the best resolution achieved using each technique.

Chapter 3 describes the experimental setup and the technical background required to perform the experiments in this thesis. We provide a complete description of beam shaping, beam characterization, sample processing and post processing characterization is given. This chapter also describes the different types of graphene sample used in our experiments.

Chapter 4 presents the results of the complete set of experiments performed to determine the possibilities and constraints of ultrafast laser patterning of CVD monolayer graphene. The conclusions of this research could have strong implications for industrial scale production of CVD graphene-based devices for future applications. First we use non-diffractive shaped beams to determine the ablation fluence threshold in CVD monolayer graphene at sub-micron scale. A highly precise characterization of the ablation fluence threshold is required to control laser material processing at such a small scale. Then, single shot ultrafast laser ablation of graphene was investigated under different parameters. Two different underlying substrates were studied, glass and quartz. We evaluated the influence of graphene morphology and the presence of defects in laser ablation at sub-micron scale. We carried out an experiment to determine the characteristics of graphene patterned under an external magnetic field. Finally, graphene nanostructuring with different fluence distributions was investigated.



# GRAPHENE PROPERTIES AND PRODUCTION

Although the behaviour of a single layer of carbon atoms, nowadays called graphene, was theoretically described back in 1947 [8], it was only experimentally realized in 2004 [1] and then attracted scientific community attention. This attention comes from its outstanding properties which could lead to a large number of potential applications in a wide range of fields.

This chapter gives a general overview on graphene. First we present the properties of graphene, which determine the fundamental mechanisms of the interaction between graphene and ultrafast lasers. An overview of the optical, electronic, mechanical, thermal and chemical properties is given. Then we discuss the different techniques existing to produce graphene, and the advantages and drawbacks of each one, with special interest on the CVD method since all samples used in the experiments of this thesis were produced with using that method, which is the most suitable for large areas graphene production nowadays. The characteristics of defects present in graphene due to production techniques are exposed as they will appear as a key parameter to control laser graphene patterning at submicron scale. Also we review potential applications of graphene in different fields, from optoelectronics to environmental sustainability, and we show that for large number of those applications, patterning of the graphene sheet at submicron scale will be required.

## 1.1/ ELECTRONIC PROPERTIES

Graphene is a crystal lattice of carbon atoms arranged in a honeycomb structure as shown in Fig. 1.1. Here we describe the derivation of the graphene structure from a quantum-mechanical point of view, following reference [10]. The primitive cell of graphene contains only one atom. Graphene has a triangular Bravais lattice defined by vectors

$$\vec{a}_1 = \frac{a}{2}(3, \sqrt{3}) \quad \vec{a}_2 = \frac{a}{2}(3, -\sqrt{3}) \quad (1.1)$$

where  $a \approx 1.42$  is the nearest neighbour distance. The honeycomb lattice contains two sub-lattices, A and B, each atom from sublattice A being surrounded by three atoms of the sublattice B, and vice versa. As shown in Fig. 1.1, the nearest neighbours distance are defined by the vectors

$$\vec{\delta}_1 = \frac{a}{2}(1, \sqrt{3}) \quad \vec{\delta}_2 = \frac{a}{2}(1, -\sqrt{3}) \quad \vec{\delta}_3 = \frac{a}{2}(-1, 0) \quad (1.2)$$

The reciprocal lattice is also triangular, with lattice vectors

$$\vec{b}_1 = \frac{2\pi}{3a}(1, \sqrt{3}) \quad \vec{b}_2 = \frac{2\pi}{3a}(1, -\sqrt{3}) \quad (1.3)$$

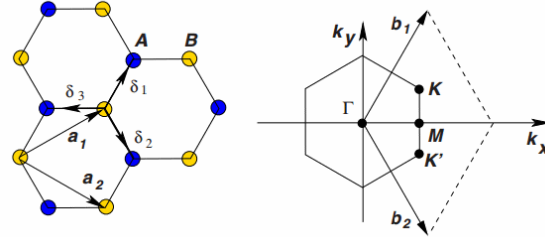


FIGURE 1.1 from [9]. Honeycomb lattice made out of two interpenetrating triangular lattices (left) and its corresponding Brillouin zone (right). The Dirac cones are located at K and K' points.

The lattice is formed by covalent bonds. Each carbon atom has 3  $sp^2$  electrons ( $\sigma$  bonds) which are stable and not reactive, in the  $xy$ -plane separated by angles of  $120^\circ$ , and two  $p$  electrons ( $\pi$  bonds) which are unstable and reactive, with the  $p$  orbital perpendicular to the  $xy$ -plane. The  $sp^2$  hybridized states ( $\sigma$  states) form occupied and empty bands with a gap, whereas  $\pi$  states form a single band with a conical self-crossing point in K (and symmetrically at K'). Points K, K' and M of the Brillouin zone have special high symmetry as illustrated in Fig. 1.1. They are described by the wave vectors

$$\vec{K} = \left(\frac{2\pi}{3a}, -\frac{2\pi}{3\sqrt{3}a}\right) \quad \vec{K}' = \left(\frac{2\pi}{3a}, \frac{2\pi}{3\sqrt{3}a}\right) \quad \vec{M} = \left(\frac{2\pi}{3a}, 0\right) \quad (1.4)$$

This conical points are the origin of the unique properties of graphene. It was firstly described by Wallace in 1947 following a simple tight-binding model [8].

### 1.1.1/ TIGHT-BINDING MODEL

In the nearest-neighbour approximation for the  $\pi$  states, with the hopping parameter  $\gamma_0$  (nearest neighbour hopping energy), the electron states basis contains two  $\pi$  states belonging to atoms of the two different sublattices A and B. In the nearest-neighbour approximation, hopping processes take place only between the different sublattices, not within themselves. The tight-binding Hamiltonian is described by the 2x2 matrix

$$\widehat{H}(\vec{k}) = \begin{pmatrix} 0 & \gamma_0 S(\vec{k}) \\ \gamma_0 S^*(\vec{k}) & 0 \end{pmatrix} \quad (1.5)$$

where  $\vec{k}$  is the wave vector and

$$S(\vec{k}) = \sum_{\delta} e^{i\vec{k}\cdot\vec{\delta}} = 2 \exp\left(\frac{ik_x a}{2}\right) \cos\left(\frac{k_y a \sqrt{3}}{2}\right) + \exp(-ik_x a) \quad (1.6)$$

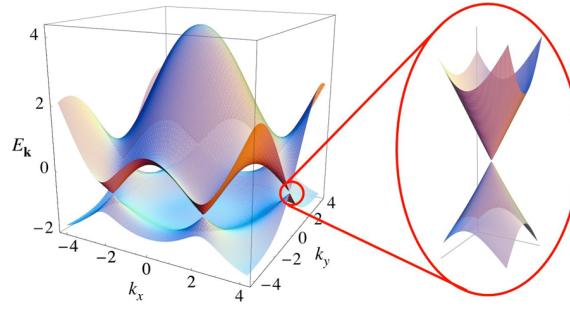


FIGURE 1.2 from [9]. Electronic dispersion in the honeycomb lattice. Left : energy spectrum (in units of  $\gamma_0$ ) for values of  $\gamma_0 \sim 2.8$  eV and  $\gamma'_0 \sim -0.2 \gamma_0$ . Right : zoom in of the energy bands close to one of the Dirac points.

Energy eigenvalues are defined by

$$E(\vec{k}) = \pm \gamma_0 |S(\vec{k})| = \pm \gamma_0 \sqrt{3 + f(\vec{k})} \quad (1.7)$$

where

$$f(\vec{k}) = 2 \cos(\sqrt{3}k_y a) + 4 \cos\left(\frac{\sqrt{3}}{2}k_y a\right) \cos\left(\frac{3}{2}k_x a\right) \quad (1.8)$$

and the sign  $\pm$  corresponds to the description of the valence band (+) and the conduction band (-).

From the previous indicated values of  $K$  and  $K'$ , resulting in  $S(\vec{K}) = S(\vec{K}') = 0$ , which means band crossing at these points.

Fig. 1.2 shows graphene band structure has a maximal energy at the  $\Gamma$  point and a saddle-point at  $M$  point of the first Brillouin zone. In addition, valence band and conduction band are crossing at  $K$  and  $K'$  points, meaning graphene is a zero-band gap semiconductor or a semimetal, in which the Fermi surface consist of only six points, so called Dirac points. By expanding Eq. 1.8 close to the Dirac points it results in a unique linear energy dispersion

$$E(\vec{k}) = \hbar v_F |\vec{k}| \quad (1.9)$$

where  $v_F = \gamma_0 \sqrt{3}a/2\hbar = 0.96 \cdot 10^6 \text{ m/s}$  is the Fermi velocity with  $\gamma_0 = -2.84$  eV. Estimated values from the experimental data for  $\gamma_0$  are typically in the range from -2.7 to -3.3 eV [11, 12]. It is due to this characteristic curvature-free band structure close to the Dirac point that electrons and holes in graphene behave as massless, i.e. their effective mass is zero, with a velocity approximately 300 times smaller than the speed of light.

In addition, graphene shows electrons mobilities up to  $\mu = 10^6 \text{ cm}^2/\text{Vs}$ , which combined with its near-ballistic transport at room temperature makes it an ideal candidate for nanoelectronic applications [13].

### 1.1.2/ MASSLESS DIRAC FERMIONS IN GRAPHENE

In undoped graphene the Fermi energy is the energy at the crossing Dirac points, with a filled valence band and an empty conduction band, so graphene is considered a gapless semiconductor or semimetal. What makes the difference between graphene and other



gapless semiconductors or semimetals, is its high electron-hole symmetry. In a realistic case, with a certain doping level, the Fermi energy will be close to the conical points energy.

The effective Hamiltonian describing the electron and hole states in this regime around the K and K' points in the perturbation theory [14] follows the next equation

$$\hat{H}_K = -i\hbar v_F \vec{\sigma} \nabla \quad (1.10)$$

where  $\vec{\sigma}$  are the Pauli matrices. This Hamiltonian is a two-dimensional equivalent to the Dirac Hamiltonian for massless fermions [15, 16], but instead of the speed of light  $c$  there is a parameter  $v_F$ .

This similarity between ultrarelativistic particles and electrons in graphene makes graphene an ideal material to study quantum relativistic effects - 'CERN on one's desk'.

Electron and hole states in graphene are chiral (which is the same as helical in the case of massless particles), as it should be in any case of massless Dirac fermions [15], and it determines relativistic properties of graphene such as Klein tunnelling, where unimpeded penetration of relativistic particles through a high and wide potential barrier takes place.

### 1.1.3/ ABSORPTION OF LIGHT

The goal of our research is to establish the advantages and possible drawbacks of graphene laser processing at sub-micron scale. Light absorption will be a key parameter in the interaction between laser beam and graphene sheet.

In the following paragraph, we derive light absorption coefficient by a graphene monolayer and we follow the approach of reference [10]. The electric field is described via the vector potential  $\vec{A}(t) = \vec{A}e^{-i\omega t}$

$$\vec{E}(t) = -\frac{1}{c} \frac{\partial \vec{A}}{\partial t} = \frac{i\omega}{c} \vec{A} \quad (1.11)$$

The Hamiltonian of Dirac electrons in presence of an electric field in the pseudospin (i.e. in one of the two AB sublattices) space, can be described as

$$\hat{H} = v\vec{\sigma}(\hat{\vec{p}} - \frac{e}{c}\vec{A}) = \hat{H}_0 + \hat{H}_{int} \quad (1.12)$$

where  $\hat{H}_{int}$  is the Hamiltonian of the electron-photon interaction inducing transitions from occupied hole state  $\psi_h(\vec{k})$  to an empty electron state  $\psi_e(\vec{k})$  with same wave vector  $\vec{k}$ .

Before continue we need to calculate the density of states,

$$\rho(E) = 2 \int \frac{d^2k}{(2\pi)^2} \delta(E - E(\vec{k})) \quad (1.13)$$

where the integration is over the Brillouin zone of the honeycomb lattice. The factor 2 takes into account the spin degeneracy. For  $E \rightarrow 0$ , the contribution comes only from the vicinity of the K and K' points and  $E = E(|\vec{q}|)$  (where  $\vec{q} = \vec{k} - \vec{K}$  and  $\vec{k} - \vec{K}'$  respectively) depends, to a first approximation (i.e. neglecting trigonal warping, that is the triangular deformation in the band structure when far enough of the Dirac points), only on the modulus of the wave vector

$$\rho(E) = 2 \cdot 2 \int_0^\infty \frac{dq}{2\pi} q \delta(E - E(q)) = \frac{2}{\pi} \frac{q(E)}{|dE/dq|} \quad (1.14)$$

Since for monolayer graphene close to the Dirac point  $E_{e,h} = \pm \hbar v k$ , the density of states can be described as

$$\rho(E) = \frac{2}{\pi} \frac{|E|}{\hbar^2 v^2} \quad (1.15)$$

when  $E \rightarrow 0$  close to the neutrality point, the density of states vanishes linearly as shown in Fig.1.3.

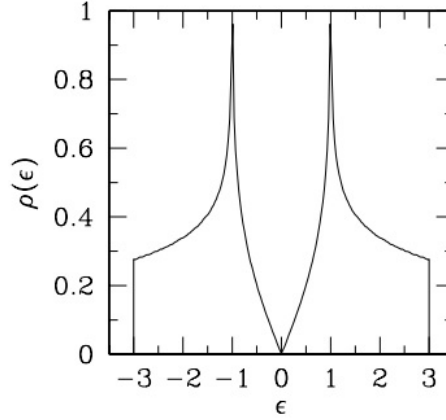


FIGURE 1.3 from [9]. Density of states per unit cell as a function of energy (in units of  $\gamma_0$ ) computed from the energy dispersion.

The matrix element of the interaction hamiltonian is

$$\langle \psi_h | \widehat{H} | \psi_e \rangle = \frac{e v}{2 w} (E_y \cos \psi \mp E_x \sin \psi) \quad (1.16)$$

where the sign  $\mp$  corresponds to the K and K' valleys respectively and  $\psi$  is the polar angle of the  $\vec{k}$  vector.

The square matrix element average over  $\psi$  results on

$$|M|^2 = \overline{|\langle \psi_h | \widehat{H} | \psi_e \rangle|^2} = \frac{e^2 v^2}{8 w^2} |\vec{E}|^2 \quad (1.17)$$

Assuming the photon propagates perpendicular to the graphene plane, then  $\vec{E} = (E_x, E_y, 0)$  and from Landau and Lifshitz lowest order of perturbation theory [17], the absorption probability per unit time is

$$P = \frac{2\pi}{\hbar} |M|^2 \rho\left(\epsilon = \frac{\hbar \omega}{2}\right) \quad (1.18)$$

where  $\epsilon = \frac{\hbar \omega}{2}$  is the final state. By introducing Eqs. 1.16 and 1.17 in previous equation we obtain

$$P = \frac{e^2}{4 \hbar^2 w} |\vec{E}|^2 \quad (1.19)$$

The absorption energy per unit time is

$$W_{abs} = P \cdot \hbar \omega = \frac{e^2}{4 \hbar} |\vec{E}|^2 \quad (1.20)$$

From [18], the incident energy flux in cgs units is

$$W_{inc} = \frac{c}{4\pi} |\vec{E}|^2 \quad (1.21)$$

From previous equations, the absorption efficiency is

$$\eta = \frac{W_{abs}}{W_{inc}} = \frac{\pi e^2}{\hbar c} = \pi \alpha \simeq 2.3\% \quad (1.22)$$

where it arises one of the main interesting characteristics differentiating graphene from most other materials : constant light absorption. Because of this feature, graphene has potential applications in broadband ultrafast photonics as it will be further detailed. It is interesting to remark the possibility of direct visualization of the fine-structure constant  $\alpha$  in the light absorption. This light absorption value is constant for  $\frac{\hbar\omega}{2} > E_F$  ( $E_F \neq 0$  for doped graphene as shown in Fig. 1.4). For smaller photon energies, the absorption efficiency is zero because the transition is forbidden by Pauli principle.

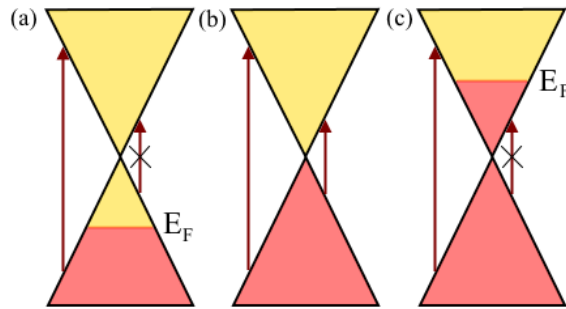


FIGURE 1.4 Interband optical transitions between filled states (red) and empty states (yellow) in (a) p-doped, (b) undoped graphene and (c) n-doped. Graphene doping level varies the permitted transitions

## 1.2/ OPTICAL PROPERTIES

After an optical excitation, the absorption of a graphene layer can be defined by the absorbance

$$\alpha(\omega) = \frac{\frac{\omega}{c_0 n_B} \text{Im}[\chi_{gr}(\omega)]}{|1 + i \frac{\omega}{2c_0 n_B} \chi_{gr}|^2} \quad (1.23)$$

where  $\chi_{gr}$  is the 2D optical susceptibility and  $n_B$  is the background refractive index. The frequency-dependent conductivity is defined as

$$\sigma(\omega) = -i\omega\epsilon_0\chi_{gr}(\omega) \quad (1.24)$$

The absorption of graphene is characterized by a frequency independent value in the near-infrared region as illustrated in Fig. 1.5. The conical intersection described in the section above has not an infinite depth, which makes a deviation from perfectly flat absorption.

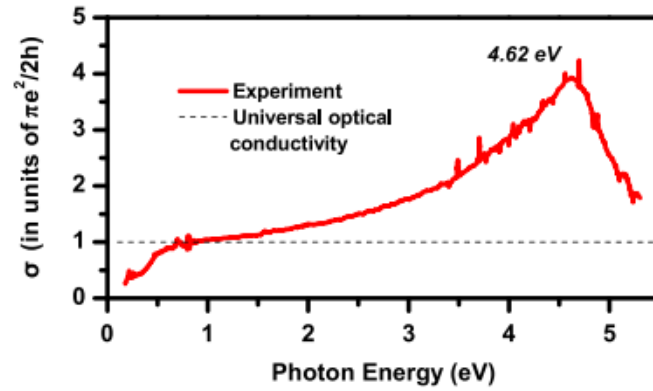


FIGURE 1.5 from [19]. Experimental optical conductivity (solid line) and the universal optical conductivity defined in the previous section (dashed line) of monolayer graphene in the spectral range of 0.2 - 5.5 eV. The experimental peak energy is 4.62 eV. Note the deviation of the optical conductivity from the universal value at low energies is attributed to spontaneous doping [20].

### 1.2.1/ CARRIER DYNAMICS

Optical excitation of graphene produces anisotropic non-equilibrium of the carrier system followed by a carrier density redistribution by two different channels : carrier-carrier scattering and carrier-phonon scattering. Carrier and phonon occupation is difficult to measure. Experimentally, free-electron densities are measured by differential transmission. Pump-probe experiments allow to access to the differential transmission spectra which is related to the pump-induced change in the occupation of the probed carrier states.

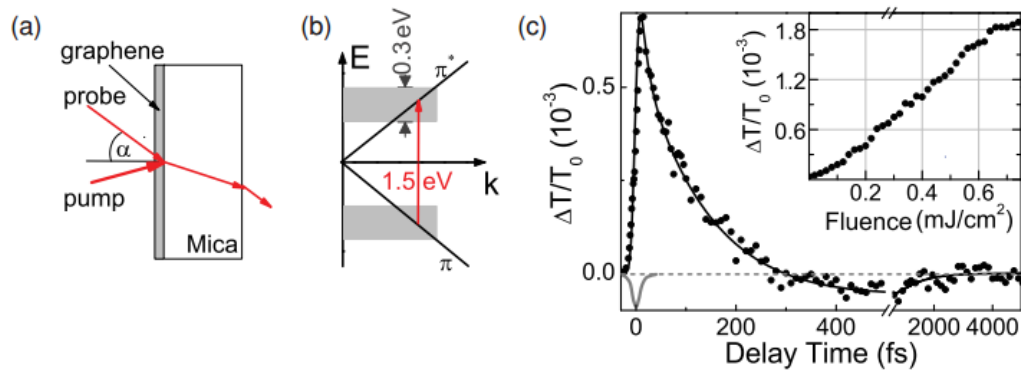


FIGURE 1.6 from [23]. (a) Graphene layer on mica structure. Incident probe light hits the surface at an angle  $\alpha = 35^\circ$ . (b) Linear band structure of graphene, arrow indicating pumped and probed optical transitions at the same wavelength. (c) Spectrally integrated transmission change (points) as a function of pump-probe delay. Solid line : biexponential fit. Gray line : cross correlation of pump and probe pulses. Inset : linear dependence of the maximum transmission change on pump fluence.

Assuming isotropic carrier distribution, the differential transmission spectrum can be des-

cribed as

$$\frac{\Delta T}{T_0}(\tau, \omega) \propto [\rho_{K_i}^{(p)} - \rho_{K_i}(-\infty)] \quad (1.25)$$

where  $\rho_{K_i}^{(p)}$  is the carrier occupation with  $K_i$  corresponds to the momentum at pump energy. Fig. 1.6 shows the relative differential transmission after ultrashort 7 fs duration pump excitation at 800 nm. Time-resolved experiments have determined that after optical excitation there is an increase of the transmission due to absorption bleaching, which comes from Pauli blocking [21, 22]. Then there is a transmission decay and the absorption increases due to the carriers redistribution. There are two types of relaxation processes leading to the carriers redistribution in graphene : Coulomb-induced and phonon-induced processes.

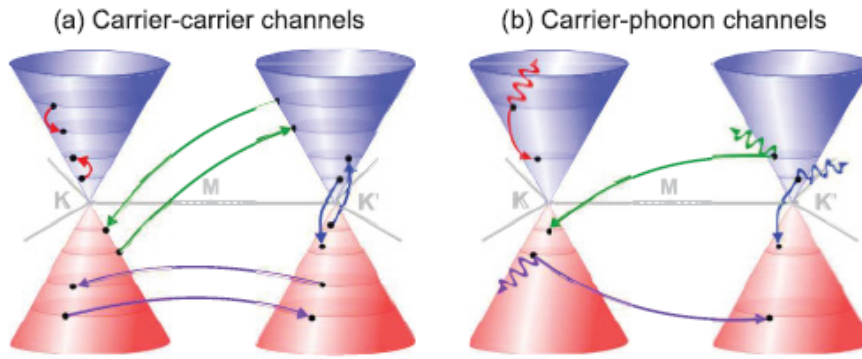


FIGURE 1.7 from [24]. (a) Coulomb- and (b) phonon-induced scattering channels along the linear band structure of graphene. Intra- and interband as well as intra- and intervalley processes are taken into account.

### 1.2.1.1/ COULOMB-INDUCED CARRIER DYNAMICS

Coulomb-induced scattering leads to ultrafast thermalization of the electronic system into a hot Fermi distribution after tens of femtoseconds, but this redistribution is anisotropic. After 200 fs, the carrier distribution is fully thermalize into a isotropic distribution. Intervalley relaxation channels are negligible for Coulomb-induced relaxation. However, Auger processes have an important role in transitions between conduction and valence band. Due to efficient impact ionization they lead to carrier multiplication increasing the density of carriers even after the optical excitation is finished. The temperature of carriers and the Coulomb-induced relaxation time depends on the pump fluence. Higher fluence leads to more scattering partners resulting in more efficient Coulomb-induced channels and, as a consequence, faster dynamics and higher temperature of the thermalized distribution. Fig. 1.7(a) illustrates two Coulomb-induced processes at the Dirac cone : left Dirac cone in (a) shows an intraband channel in which an excited carrier relaxes towards a lower excited state in the conduction band by exciting another carrier in the conduction band to a higher energetic state, and right Dirac cone in (a) illustrates an interband channel where carrier relaxes from the conduction towards the valence band by exciting a carrier from the valence to the conduction band.

### 1.2.1.2/ PHONON-INDUCED CARRIER DYNAMICS

In tens of femtoseconds phonon-induced scattering relaxation leads the carrier distribution towards the K point. Dynamics determined by scattering of excited carriers towards lower energetical states accompanied by phonon emission. Once the carriers are close to the Dirac point, the interband processes become important. Phonon-induced relaxation channels leads to an energy transfer between the carriers and the lattice. Two different processes are possible : an excited carrier scatters to energetically lower state emitting a phonon, or the absorption of a phonon exciting a carrier to a higher energy. If the phonon momentum is large enough, phonon-induced relaxation channels can bridge two different valleys within the band structure of graphene, so intra- and intervalley processes can be differentiated. Fig. 1.7(b) shows relaxation channels involving phonon emission.

Two different phonon modes can be distinguished : longitudinal and transversal. Longitudinal modes scatter across the Dirac cone contributing to isotropic carrier distribution, and transversal modes which scatter along the Dirac cone contributing to a faster thermalization of the excited carriers.

### 1.2.1.3/ COULOMB- AND PHONON-INDUCED CARRIER DYNAMICS

Both relaxation channels compete with each other. Combined dynamics is not simply the sum of the single contributions. Fig. 1.8 illustrates the angle-averaged carrier distribution as a function of carrier energy and relaxation time. Two different relaxation times have been observed experimentally [21, 22].

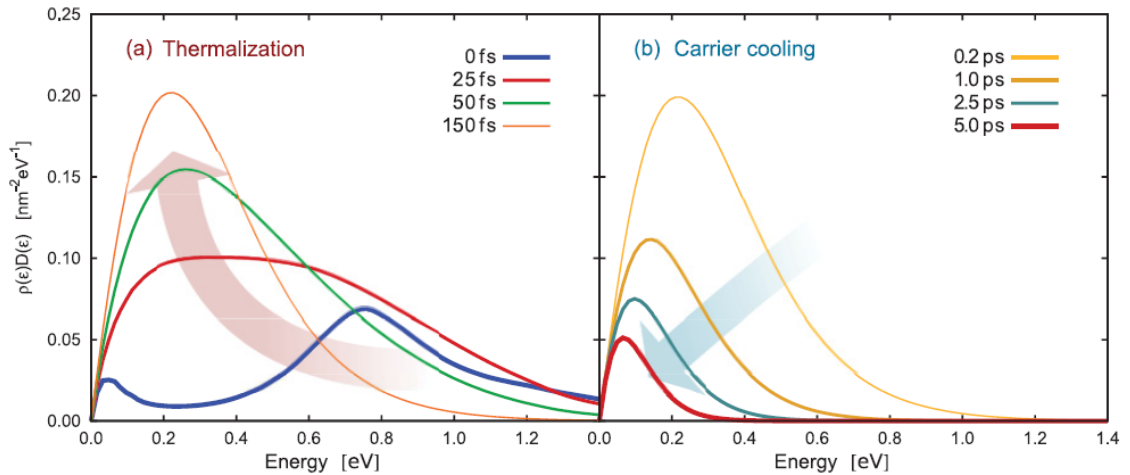


FIGURE 1.8 from [24]. Temporal evolution of the angle-averaged carrier distribution  $[\rho_k$  weighted by the density of states  $D(\omega)]$  as a function of energy. The relaxation dynamics is determined by Coulomb- and phonon-induced intra- and interband scattering channels. It is characterized by (a) an ultrafast thermalization followed by (b) cooling of the optically excited carriers.

First, a fast one of  $\sim 100$  fs corresponding carrier-carrier intraband collisions leading to rapid carrier thermalization to form a hot Fermi-Dirac carrier distribution as shown in Fig. 1.8(a). Coulomb relaxation channels are predominant during this process, although carrier-phonon scattering in steps of 150 - 200 meV also brings the carriers towards the

Dirac point. The carriers at this moment are in equilibrium among each other, but they are still in non-equilibrium with the lattice since the temperature of the carriers is much higher than the temperature of the lattice. Then the carrier distribution cools down due to intraband phonon scattering, transferring the energy from the carrier system to the lattice with a slow relaxation time in the order of the picoseconds corresponding to interband relaxation due to electron-hole recombination as illustrated in Fig. 1.8(b). Due to this characteristic carrier dynamics, graphene shows saturable absorption, i.e. at high optical intensities the photo-generated carriers block further absorption as shown in Fig. 1.9.

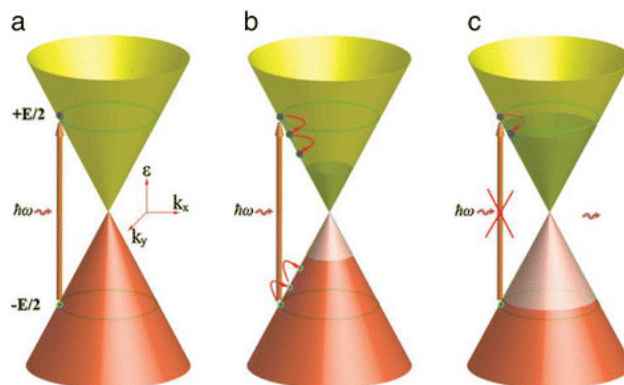


FIGURE 1.9 from [25]. Processes of saturable absorption in graphene. (a) Optical interband excited by incident light. (b) The photogenerated carriers redistribute a Fermi-Dirac distribution. (c) Further absorption is blocked under sufficient intensity of incident light.

### 1.2.2/ MULTILAYER GRAPHENE

In this section we give a brief summary of the main optoelectronic characteristics of multilayer graphene compared to monolayer graphene.

Multilayer graphene, in contrast to single layer, turns to be a gapless semiconductor with nonlinear band touching. Bilayer and trilayer graphene were described to have parabolic and quadratic band touching, respectively [26, 27]. Experimental results showed carrier mobility in single layer greater than in multilayer graphene due to the linear dispersion [28]. However, carrier transport measurements showed single layer is much more sensitive to impurities due to reduction in the screening effect produced by the stacking of several layers leading to larger mobility variation.

For few graphene layers, the absorption increases linearly up to adding a 2.3 % absorption per layer. The optical absorption in multilayer graphene was reported to be dependent on the stacking orientation [29].

## 1.3/ MECHANICAL, THERMAL AND CHEMICAL PROPERTIES

### 1.3.1/ MECHANICAL PROPERTIES

Graphene is the strongest material ever tested [30]. Experiments in free standing monolayer graphene membranes by nanoindentation in an atomic force microscope as shown in Fig. 1.10 have measured a tensile strength, which is the capacity to withstand loads tending to elongate the material before breaking, of 130 GPa. It has a Young modulus,



which characterizes the stiffness of the material on the order of 1TPa, i.e. in the same order of magnitude as diamond. It is well known the example exposed by the Nobel laureate for graphene discovery André Geim, in which a graphene sheet of 1 square meter area could hold a 4 kg cat. That graphene sheet would have a weight of only 0.77 mg, showing the extreme lightness of graphene, about 1000 times lighter than the same paper surface.

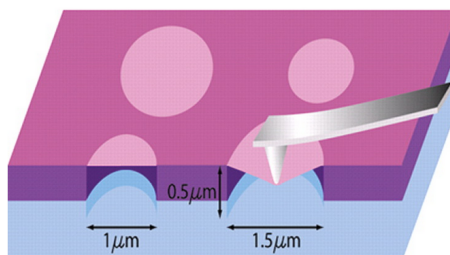


FIGURE 1.10 from [30]. Schematic of nanoindentation test on suspended graphene membrane.

### 1.3.2/ THERMAL PROPERTIES

Graphene shows 100-fold anisotropy in heat flow between in-plane and out-of-plane directions. The high thermal conductivity in the in-plane direction is due to covalent  $sp^2$  bonding between carbon atoms where the bonding energy is  $E \sim 5.9$  eV. The out-of-plane conductivity is limited by Van der Waals coupling, with a much weaker bonding energy of  $E \sim 50$  meV.

Graphene thermal properties are determined by the lattice vibrational modes (phonon) dispersion. It has been measured a thermal conductivity of 2000 - 4000 W/mK in suspended graphene [31, 32, 33], which is much higher compared to the diamond thermal conductivity of 2000 W. In addition, isotropic ballistic thermal conductance has been demonstrated in graphene.

In-plane conductivity decreases when in graphene sheet is in contact with a substrate, which can have an important role for applications. This behaviour is expected from phonon propagation, for example on  $SiO_2$  substrate, due to coupling and scattering of all graphene phonons with the substrate vibrational modes [34].

### 1.3.3/ CHEMICAL PROPERTIES

Graphene is a highly inert form of carbon. However, every single carbon atom in graphene is available for chemical reactions from two sides, due to its 2D structure. It has been shown that graphene edge atoms have a special chemical reactivity and presence of defects on graphene sheet can potentiate chemical reactivity [35].

To further extent graphene potential applications, functionalization of graphene is crucial. Graphene solubility has been improved by attaching different chemical functional groups to its basal plane. Charge carrier type and concentration have been modulated via surface transfer doping by coating it with various metal films or organic molecules.

Graphene is highly sensitive to air, in particular to humidity. In chemical vapor deposited graphene on  $SiO_2$  it has been reported an extreme sensitivity to water vapour, with water molecules acting as p-dopants which could lead to electronic devices to be properly encapsulated to ensure stable operation [36].



## 1.4/ GRAPHENE PRODUCTION

The high mobility and optical transparency of graphene, in addition to its flexibility, robustness and environmental stability, attracts enormous interest for applications. The main focus has been on fundamental physics and electronic devices, but graphene great potential is expected to be in photonics and optoelectronics, where the combination of its unique optical and electronic properties can be fully exploited. However, the rise of graphene applications such as solar cells, light-emitting devices, touch screens or photodetectors, depends on two main technological challenges : large uniform graphene layer production and graphene patterning at micro- and nanoscale.

In this section the different production methods will be exposed and their advantages and drawbacks regarding potential applications will be compared.

Graphene production techniques can be classified in two main groups : exfoliation techniques and chemical growth methods.

### 1.4.1/ EXFOLIATION

Exfoliation methods produce graphene with the lowest number of defects and the highest electron mobility. The basis of those procedures consist of peeling off graphene layers from a bulk material.

#### 1.4.1.1/ SCOTCH TAPE TECHNIQUE - MICROMECHANICAL CLEAVAGE

This technique allowed Konstantin Novoselov and Andre Geim to isolate pure graphene for the first time [9]. This procedure consisted in depositing a flake of graphite on a piece of scotch tape. The graphite was peeled off repeatedly on the adhesive tape. Once there was an homogenous layer of graphite, the thinnest flakes were transferred onto  $\text{SiO}_2$  pressing gently with the scotch tape. The monolayers of carbon atoms could be imaged under a simple optical microscope. Fig ; 1.11 shows optical microscope transmission and reflection contrast images of graphene flakes transferred onto Corning glass. Since the absorption of each layer of graphene is 2.3% and the total absorption increases linearly up to approximately 10 layers it is possible to determine the number of layers for each flake using an optical microscope.

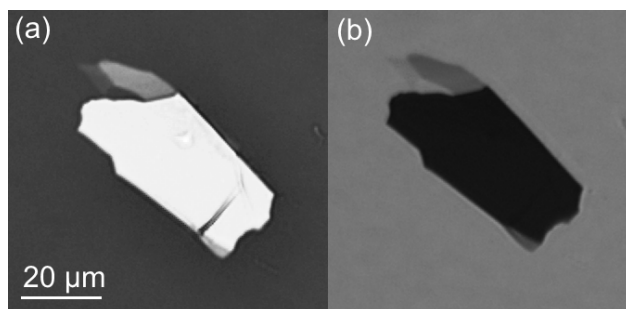


FIGURE 1.11 (a) Reflection and (b) transmission image of graphene flakes produced by scotch tape method under x40 magnification optical microscope. Different grayscale color correspond to a different number of graphene layers.

Resulting exfoliated graphene using this method exhibit a high crystal quality with low number of defects. However, graphene flakes obtained, with a maximum size in the order of tens of micrometers, have irregular shape and are too small for technological applications. Small size of flakes allows for testing graphene properties but to produce large-scale devices large graphene sheets are required.

#### 1.4.1.2/ WEDGE MECHANICAL EXFOLIATION

This method to synthesize few layers of graphene uses an ultra-sharp single crystal diamond wedge to penetrate into a bulk of highly ordered pyrolytic graphite (HOPG) and cleave a stack of several layers of graphene. The cleaving procedure is supported by ultrasonic oscillations along the wedge. Using this technique separation, folding and shearing of graphene layers is possible [37]. However, areas of only a few micrometers can be achieved with this method, which is not compatible with industrial production of graphene [38].

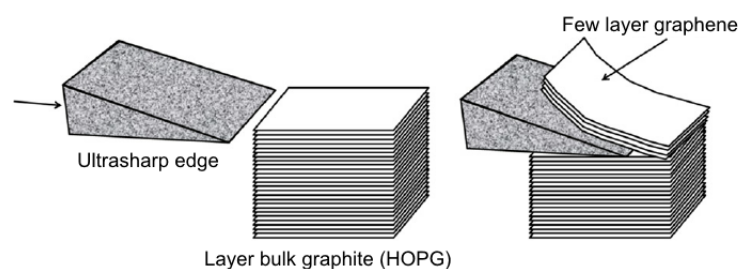


FIGURE 1.12 from [37]. Schematic diagram for wedge-based mechanical exfoliation of a few layers of graphene.

#### 1.4.1.3/ LIQUID PHASE EXFOLIATION (LPE)

Liquid phase exfoliation of graphite by ultrasonic technique is a straightforward process to produce clean graphene sheets ready for organic functionalization. It consists of three steps : chemical wet dispersion of graphite in a solvent, exfoliation by ultrasonic wave treatment and purification. This method has been demonstrated to be effective in dispersing graphene in solvents and also allows to incorporate additives during the sonication process such as antioxidants [39], polymers [40] and surfactants [41], increasing the functionality of the resulting graphene layers.

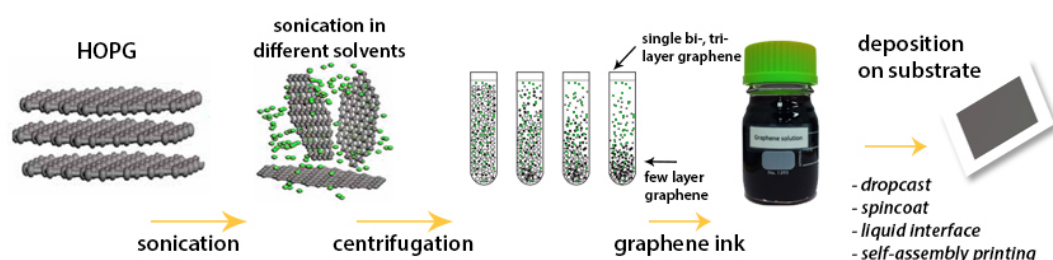


FIGURE 1.13 from [46]. Schematic liquid phase exfoliation technique to produce graphene.

LPE has been considered one of the most promising methods for industrial production of graphene due to its low cost and scalability. LPE has been investigated using graphite oxide, natural graphite and graphite intercalation compounds. However, there are still some disadvantages to be solved such as the use of large quantity of acid and oxidizing agents in the case of graphite oxide which requires time-consuming washing steps [42], very low yield production of graphene for natural graphite [43] or the use of poisonous chemical agents and dangerous chemical reactions when using graphite intercalation compounds [44, 45].

#### 1.4.2/ CHEMICAL GROWTH METHODS

While exfoliation produces graphene with nearly ideal electrical and mechanical properties which is excellent for fundamental research, their size, thickness and uniformity are not controllable, which is a large disadvantage for technological applications [47]. Graphene flakes, which have a size in the order of tens of microns, are randomly distributed on the substrate not covering it completely. Exfoliation methods cannot be used to produce a continuous graphene film and chemical methods are needed to growth graphene from carbon atoms [48].

##### 1.4.2.1/ CHEMICAL VAPOUR DEPOSITION (CVD)

CVD graphene production consists of two steps, a pyrolysis to form pure carbon from a compound material followed by the creation of the graphene layer from the dissociated atoms.

A metallic substrate such as copper is placed into a furnace and heated to  $\sim 1000^{\circ}\text{C}$  under low vacuum. Hydrogen and methane are then introduced in the furnace. A reaction between methane and the surface of the metal substrate is catalyzed by hydrogen, causing carbon atoms from methane to be deposited onto the surface of the metallic substrate through chemical adsorption. Various catalyst of elemental metals are typically used to reduce the reaction temperature because the pyrolytic decomposition of precursors would require temperatures up to  $2500^{\circ}\text{C}$  without catalyst.

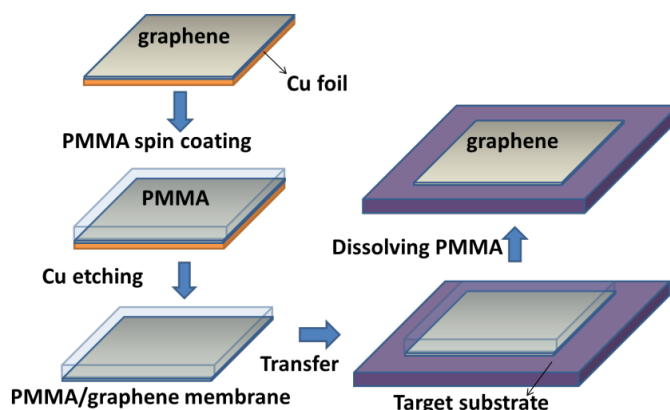


FIGURE 1.14 from [49]. Schematic diagram of the transfer process to an arbitrary substrate.

Once the carbon atoms are deposited onto the metallic substrate, the furnace is quickly cooled down, what crystallizes the carbon layers into a continuous layer of graphene on the metallic substrate.

CVD produced graphene carries a considerable number of impurities due to the different materials required in the procedure. It has been shown, however, that such impurities can be minimized by controlling the growth of the film as function of time and Cu substrate thickness [52]. CVD graphene has polycrystalline structure due to monocrystalline growth at each nucleation seed, and as a result grain boundaries are formed in graphene when monocrystalline islands join during the growth process. Difference in local electrical, mechanical and optical properties due to the polycrystalline nature of graphene synthesized by CVD method was reported [53, 54, 81, 75]. In addition, CVD graphene tends to form wrinkles as shown in Fig. 1.15 due to the difference in thermal expansion between graphene and the copper substrate, but wrinkle formation has been minimized by proper annealing. Absence of wrinkle formation in graphene transferred to strongly hydrophobic substrates was also demonstrated [51].

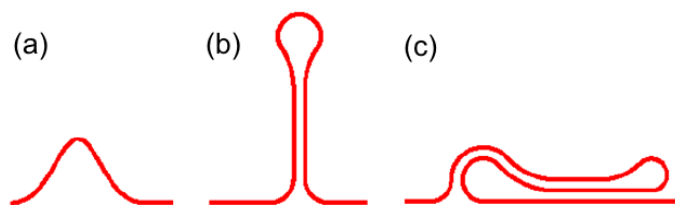


FIGURE 1.15 from [50]. Three different wrinkle morphologies : (a) simple ripple geometry, (b) standing collapse wrinkle, and (c) folded geometry wrinkle.

CVD method is of special interest since it is possible to produce a continuous graphene layer as large as the underlying metal substrate, i.e. now on the order of  $1 \text{ m}^2$ . In addition, it has been shown that graphene films produced by CVD are predominantly single-layer, with less than 5 % of the area having few layers [52].

An important advantage of CVD among other techniques is the ability to transfer the graphene layer to another substrate. Once the graphene/copper foil has been removed from the furnace and cooled down, a polymer such as polymethyl methacrylate (PMMA) can be spincoated onto the graphene surface. By using an etchant as ferric chloride, the copper foil can be removed. Then the graphene/polymer foil can be attached to another substrate and finally the polymer can be removed by a solvent such as acetone. The result is a graphene layer attached to the target substrate.

#### 1.4.2.2/ PLASMA-ENHANCED CVD

It is possible to produce areas up to several  $\text{mm}^2$  of single layer graphene with this procedure. As mentioned before, during CVD process,  $\text{H}_2$  and  $\text{CH}_4$  are introduced into the chamber at  $1000^\circ\text{C}$  under low vacuum, and takes advantage of the catalytic influence of copper and hydrogen. However, methane has a higher activation temperature for the catalytic reaction which produces significant substrate evaporation, inducing defects in the resulting graphene sheets.

Main advantage of plasma-enhanced CVD procedure is the shortening of the proces-

sing time which allows for a much smaller evaporation of the substrate [58]. On the other hand, it has been determined a high number of defects due to the energetic particles of the plasma interacting with the growing surface [59].

This method allows graphene synthesis from hydrogen/methane gas mixture on copper substrate which can be transferred onto  $\text{SiO}_2$  or other substrates.

#### 1.4.2.3/ REDUCED GRAPHENE OXIDE

The goal of this method is to obtain graphene from graphite oxide. The final product is called reduced graphene oxide (rGO) instead of simply graphene, to differentiate between both, since in rGO despite the reduction process there still remain some oxygen functional groups. Production of rGO is a multistep procedure. The starting material is graphite oxide, which is a compound of carbon, hydrogen and oxygen atoms. It is obtained by oxidizing graphite, usually with a mixture of sulphuric acid, sodium nitrate and potassium permanganate. Graphite oxide is dispersed in a base solution, such as water, and the water intercalation between the individual atomic layers combined with sonication leads to graphene oxide (GO). Sonication is a time-efficient method, however, it is highly damaging the lattice structure which deteriorates GO properties compared to those in pristine graphene. A final step needs to be carried out to obtain rGO. Several chemical, thermal and electrochemical methods have been proposed, but they are complex and time consuming. Some of these methods are to expose GO to hydrogen plasma for few seconds, directly heating GO to temperatures above  $1000^\circ\text{C}$  or treating GO in a hydrazine hydrate at  $100^\circ\text{C}$  for 24 hours. In addition, all these methods produce damage in graphene structure. New methods under investigation are trying to solve these problems. Recently, large scale production of highly conductive rGO sheets by solvent-free low temperature reduction which exhibits excellent conductivity and a high surface area has been reported [60].

#### 1.4.2.4/ EPITAXIAL GRAPHENE

When heating silicon carbide (SiC) at temperatures above  $1100^\circ\text{C}$  in ultra-high vacuum, the silicon sublimates from the surface and carbon rich surface nucleates into epitaxial graphene layer [61]. Main drawback of this procedure is the poor quality of graphene produced in ultrahigh vacuum because of the high sublimation rates at low temperature. Several methods have been developed to control the rate at which silicon sublimates, such as supplying silicon in a vapor phase compound [62] or flowing an inert gas over the hot SiC surface [63], which leads to increasing complexity and cost in epitaxial graphene production.

#### 1.4.2.5/ MOLECULAR BEAM EPITAXY

In molecular beam epitaxy (MBE) the substrate is heated typically to  $500 - 600^\circ\text{C}$ , then precise beams of atoms are directed to the substrate. The atoms land and reach the substrate surface, condensing and forming a crystallographic structure. Graphene layers have been grown by MBE in the carbon face of SiC substrate [64]. Growth of single layer graphene nanometer size by solid carbon source molecular beam epitaxy on hexagonal boron nitride (h-BN) with a high lattice quality, less than a 2 % mismatch to ideal graphene lattice, has been also demonstrated [66]. Unlike exfoliation or CVD, where graphene layer

transfer onto substrate is imposed, graphene on SiC can be directly used for electronic applications. In MBE, the structure, thickness and electronic properties are determined by the carbon flux, the substrate temperature and the carbon sources used. In addition, different molecular beam epitaxy procedures leads to different graphene characteristics : carbon molecular beam epitaxy with  $C_{60}$  produces AB staked graphene, whereas growth with graphite filament results in non-Bernal stacked graphene layers [65]. Low quality graphene was reported in SiC molecular beam epitaxy on h-BN substrate due to complex graphene growth process involving various deposition characteristics of a multitude of carbon species, such as atomic carbon and carbon dimers [68]. Optimization of the molecular beam composition has been suggested to increase the quality of graphene films.




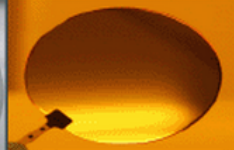
Method	Mechanical exfoliation	Reduced graphene oxide	Epitaxial growth in SiC	CVD based graphene growth
Size	10 - 100 $\mu\text{m}$	> 15 cm	< 10 cm	> 50 cm
Mobility	best	bad	high	high
Transfer	yes	yes	no	yes
Applications	no	yes	little	most
Scalable	no	yes	not yet	yes
				

FIGURE 1.16 from [67]. Comparison between four representative methods to obtain graphene films.

#### 1.4.2.6/ CONCLUSIONS

In this section we presented the two main types of methods to produce graphene : exfoliation and chemicals methods. Graphene produced by exfoliation methods has very good quality, with a high electron mobility and a low presence of defects. However, graphene layer size and uniformity over a substrate is difficult to control. Graphene flakes are in the order of tens of microns. Larger films are achievable using liquid phase exfoliation, but it shows a low yield production and it involves a large amount of harmful chemicals. On the other hand, although graphene produced by chemical methods presents a larger amount of impurities due to the different materials required in the process lowering the final quality of graphene, it is possible to produce larger continuous films. Epitaxial graphene and graphene produced by molecular beam epitaxy have a poor quality and its improvement would increase its cost and complexity. Obtaining reduced graphite oxide a costly multistep procedure producing a graphene sheet with oxygen functional groups wich leads to lower graphene quality. CVD graphene, even if the number defects and impurities is high, its quality is high enough to be used in photonics and optoelectronics applications. In addition this method allows to produce graphene sheets in the order of 1  $\text{m}^2$ . In conclusion, CVD method rises as the most convenient for industrial scale production of graphene-based devices. This is the reason to focus our research in laser patterning in CVD monolayer graphene.



### 1.4.3/ DEFECTS IN GRAPHENE

The electronic and mechanical properties of graphene samples with high perfection of the atomic lattice are outstanding, such as ballistic electronic propagation with high carrier mobilities. However, during the crystal growth or processing, structural defects can be generated which obviously deteriorate the performance of graphene-based devices. Non-controlled defects is a main disadvantage for future graphene-based devices, however, the study and control of the deviations from perfect graphene can be useful for some applications through precisely engineered-defect devices. In addition, the presence of defects has a direct effect on the local topology of graphene, breaking its planarity into a wavy surface.

Defects in single layer graphene can be classified in different categories depending on its dimension [69].

#### 1.4.3.1/ ZERO DIMENSIONAL DEFECTS

Point defects, which are zero-dimensional, typically consist in vacancies or interstitial atoms. In this category there are the Stone-Wales defects, where no carbon atom is missing but four carbon hexagons rearrange into two pentagons and two heptagons due to the  $90^\circ$  rotation of one C-C bond.

Typical defect in any crystalline structure is one lattice atom missing, called single vacancy. In a single vacancy takes place a Jahn-Teller distortion, where the missing atom initially leads to a degenerated electronic ground state. However, a change in the geometrical configuration removes the degeneracy reducing the total energy of the system. Single vacancies in graphene have a energy formation of 7.5 eV. This high energy prevents the presence of a considerable point defects in thermal equilibrium reducing the generation of defects in graphene at room temperature.

Multiple vacancies, such as double vacancies are built by the adhesion of two single vacancies or by removing two neighbouring atoms. In the double vacancy case, the hexagonal structure is reorganized into pentagons and octagons.

Other types of zero-dimensional defects are adatoms, which can be a carbon or a foreign atoms, which form locally a three-dimensional structure. In the case of substitutional impurities, a foreign atom is substituting one or several carbon atoms of the lattice, making it interesting for application requiring doped graphene.

#### 1.4.3.2/ ONE DIMENSIONAL DEFECTS

One-dimensional defects have been identified in graphene [70]. Usually this line defects are separating two domains with different lattice orientations. This happens for instance in graphene grown on metal surfaces [70, 71]. At the edge of a graphene layer the carbon atoms can be both free or passivated with an hydrogen atom.

Graphene simplest edge structures are zigzag and armchair configurations as shown in Fig. 1.17(c). In the case of any intermediate edge structure, such as a missing carbon atoms or the attachment of a chemical group, it is considered a defective edge.

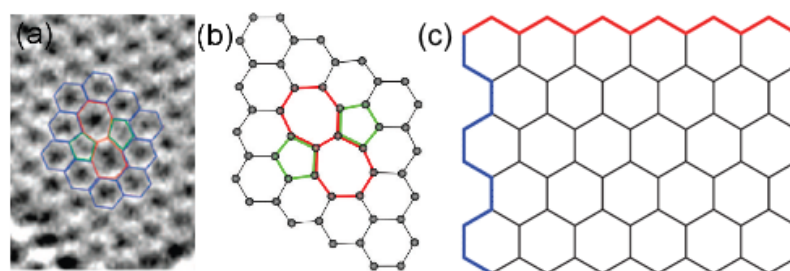


FIGURE 1.17 from [69]. Stone-Wales defect, formed by rotating a carbon-carbon bond by  $90^\circ$ . (a) Experimental TEM image of the defect ; (b) its atomic structure as obtained from density functional theory (DFT) calculations. (c) Zigzag (red) and armchair (blue) edge configurations of graphene [72].

#### 1.4.3.3/ DEFECT FORMATION

There are three main mechanism leading to graphene defect formation. Particle irradiation is a process in which a layer of graphene is irradiated with electrons or ions generating the ballistic ejection of a carbon atom, with the subsequent vacancy generation [73, 74]. The energy threshold needed to transfer to the carbon atom to leave its lattice position is 18-20 eV. Ion irradiation methods, such as focused ion beam (FIB) can be very convenient to produce graphene defect engineered devices, where defects are implemented in a controlled manner in graphene to change its properties. There exist also chemical methods generating vacancies since the reaction of a carbon atom with another chemical species can lead to the loss of the carbon atom, however, graphene is highly inert so there is a limited number of reactions generating a defect. The last mechanism responsible of defects generation is the crystal growth, where vacancies appear at the boundaries of different crystallly oriented grains since its nucleation and growth does not take place uniformly [75]. This mechanism will be explained in more details in the next section.

The presence of defects changes the properties of graphene locally. Chemical properties are affected by defects since graphene reactivity is enhanced. Chemical groups can attach easily to defects and it can have interesting applications such as local functionalization of graphene samples or development of electrical contacts with metal electrodes. As an example, selective deposition of metal by atomic layer deposition has been identified in CVD graphene's line defect [76].

Defects also have a strong effect on electronic properties. The bond length between atoms are different in the presence of defects compared to perfect graphene. Point defects induce an increase of the electronic density of states near the Fermi level and local bandgap opening [77, 78]. In the case of line defects, localized electronic states appear along the line. Next section will detail the effects of grain boundaries on electronic structure.

The influence of defects on the mechanical properties of graphene is under investigation, pressure tests have shown that cracks initiate at grain boundaries and propagate along the boundary or deflects into the graphene island depending on the environmental conditions [79]. However, indentation tests directly on grain boundaries have demonstrated that they are almost as strong as pristine graphene [80].



#### 1.4.3.4/ GRAIN BOUNDARY AND DIFFUSION PROBLEMS

Although no impact due to grain boundaries on patterning graphene when using particle beam or UV lithography has been reported, for our research it was of special interest to focus on the possible effects those structural defects could have in laser processing of graphene at sub-micron scale.

All the samples used in our investigations are produced by CVD. As mentioned in section CVD, it is a method that allows to fabricate large-scale graphene samples, however, it makes its polycrystallinity almost unavoidable. During the crystal growth using this method they appear line defects, i.e. grain boundaries.

Scanning tunneling microscopy measurements have shown direct relation between mismatch angle and the electronic properties of the grain boundaries in CVD graphene.[81]. Atomic-resolution imaging below 1 nm shows grain boundaries are originated mainly by pentagons and heptagons pairs. Theoretical calculations following the density functional theory model show that the lines consisting on heptagons and pentagons pairs (point defects) increase the reflectivity of incident electronic wave packets [75].

Investigations on the evolution of electronic wave packets through grain boundaries of different structure using numerical solution of the time-dependent Schrödinger equation have shown there are two main parameters controlling the energy dependence of the transport : the misorientation angle between two adjacent grain boundaries and its atomic structure [81].

Although there is a consistent theoretical description on how charge carrier transport between single-crystal domains could be affected by scattering across grain boundaries, the five order of magnitude difference between grain boundary size and the atoms present in it are the reason for the few experimental results up to now.

Electrical measurements on individual grain boundaries have shown an improvement up to one order of magnitude of the electrical conductance in the case of better interconnected boundaries [83] suggesting that CVD graphene with good connection between grain boundaries may present a uniform high electrical conductance.

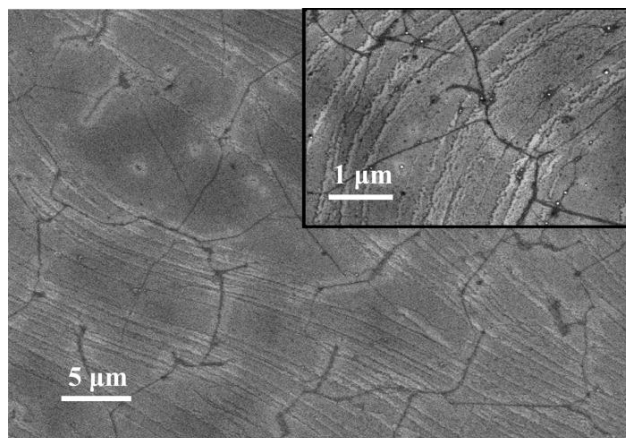


FIGURE 1.18 from [82]. SEM image of graphene layer by CVD graphene shows the formation of wrinkles and individual grain domains with grain boundaries as darker lines.

## 1.5/ GRAPHENE APPLICATIONS

Due to its outstanding electrical, optical, thermal and mechanical properties, graphene is regarded as a revolutionary material with potential applications in a wide range of fields from photovoltaics to environmental sustainability. In this section we will focus on photonics and optoelectronics applications, where nanopatterning is needed for a large number of applications. We also discuss potential applications in other fields, some of them requiring graphene structuring at sub-micron scale.

### 1.5.1/ PHOTONICS AND OPTOELECTRONICS APPLICATIONS

#### 1.5.1.1/ TRANSPARENT CONDUCTORS

Most optoelectronic applications require a material with a low sheet resistivity  $R_s$  and a high transparency. Nowadays, the majority of transparent conductors are semiconductors based, such as doped indium oxide ( $\text{In}_2\text{O}_3$ ) [84], tin oxide ( $\text{SnO}_2$ ) [85] or zinc oxide ( $\text{ZnO}$ ) [86] and their combinations. The main material currently used is Indium Tin Oxide (ITO), which is a n-type doped semiconductor where the tin atoms act as n-type donors. ITO in glass has shown a  $T \sim 80\%$  and a  $R_s = 10 \Omega/\text{cm}$  (how it was historically defined). Disadvantages regarding ITO are its high cost due to indium scarcity, its sensitivity to acidic and basic environment, the complex processing requirements. In addition, ITO brittleness confers a limited flexibility which may be a problem for flexible displays and touchscreens. Graphene has been determined to have a larger transparency than ITO [85, 86]. In the case of no doping, ideal intrinsic graphene has a  $R_s = 6 \text{ k}\Omega/\text{cm}$  and  $T \sim 97.7\%$ , and only transparency is better in graphene than in ITO. But typically, in exfoliated graphene the number of intrinsic carriers is  $n \geq 10^{12} \text{ cm}^{-2}$  which reduces  $R_s$ , achieving values similar than in ITO [87].

#### 1.5.1.2/ PHOTOVOLTAIC DEVICES

Currently most photovoltaic devices are silicon based, and efficiencies up to 25 % have been reported [88]. Organic cells are cheaper but they have a lower efficiency. Other common type of solar cells are dye-sensitized solar cells.

Graphene can have multiple functionalities in solar cells : transparent conductor, photoactive material, charge transport channel or it can act as a catalytic counter electrode material.

Yong et al. have reported [89] an efficiency of  $\sim 12\%$  in solar cells using graphene as a photoactive element. Incorporating graphene into the nanostructured  $\text{TiO}_2$  photoanode has been determined to enhance charge transport, and by preventing recombination it leads to an internal photocurrent efficiency improvement [90].

#### 1.5.1.3/ LIGHT-EMITTING DEVICES

Organic light-emitting diodes (OLEDs) consist of an electroluminescent layer in between two charge injecting electrodes, from which at least one has to be transparent. OLEDs have a wide range of application in televisions and display screens such as computer screens, mobile phones or digital cameras. Usually indium tin oxide (ITO), having a work function of 4.4 - 4.5 eV, is used as transparent conductor film. Its efficiency is decreased

due to its diffusion into the active OLED layer[91].

Graphene has a work function of 4.5 eV, similar to ITO. Graphene production methods are cheaper, and it shows a high flexibility. These characteristics make graphene an ideal candidate for OLEDs anodes.

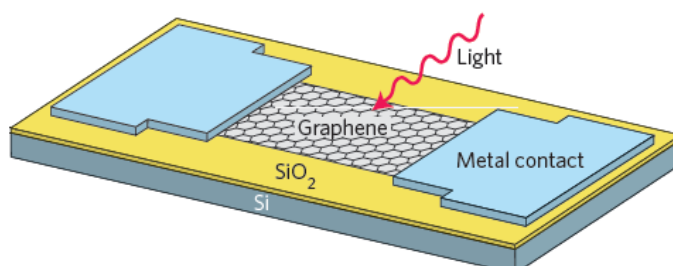


FIGURE 1.19 from ref. [21]. Schematic of a graphene-based photodetector.

#### 1.5.1.4/ PHOTODETECTORS

Photodetectors are based on the photoelectric effect, where the absorbed photon energy is converted into electrical current. Photodetectors have a wide range of applications such as remote controls, DVD players, CCD cameras or photodiodes in a fiber optic connection.

The spectral bandwidth of a photodetector is limited by the material's absorption. The broad absorption band of graphene, from UV to THz, is one of the main advantages of graphene-based photodetectors (GPDs). Also its intrinsic high carrier mobility provides a fast response time [21].

The maximum possible operating bandwidth is limited by the transit time, i.e. the finite duration of the photogenerated current, which would overpass the current photodetectors state of the art with values up to 1500 GHz [92].

A single layer of graphene has a poor absorption of 2.3 %, which could limit graphene-based photodetector performance. However, theoretical calculations demonstrated that a single sheet of doped graphene, patterned into a periodically array of nanodisks with a diameter of 60 nm and a 120 nm periodicity shows a 100 % light absorption [93]. In the case of RC-limited GPDs, operating bandwidth of 640 GHz has been reported [92].

#### 1.5.1.5/ SATURABLE ABSORBERS AND ULTRAFAST LASERS

There is a need for non-linear optical and electro-optical properties materials for most photonics applications. Of special interest are ultrafast laser sources, which have been used in a large range of applications, from basic research to industrial scale material processing.

Solid-state laser are the most common ultrashort pulses sources. One of the modelocking techniques is the insertion of a saturable absorber in the laser cavity, where a nonlinear element enables continuous wave.

Nonlinear material requirements for a good performance saturable absorber are a fast response time, broad wavelength range, low optical loss, low cost and easy integration into the optical system.

Typically, ultrafast lasers are based on semiconductor saturable absorber mirrors [94], but they have a narrow tuning range and their fabrication process is complex [95].

Single-wall carbon nanotubes (SWNTs) have been used as saturable absorber due to its simpler and cost-effective fabrication process, however, their tunability is depending on the diameter of the nanotubes.

Graphene saturable absorbers (GSAs) have several advantages over previously used materials. The linear dispersion of Dirac electrons allows for an electron-hole pair in resonance for any excitation. Its ultrafast carrier dynamics, together with its large absorption band and the Pauli blocking makes it an optimum material as ultrabroadband saturable absorber. In addition, there is no need of bandgap engineering or diameter control like in the case of other materials.

Ultrafast lasers have been reported based on graphene-polymer composites [95], CVD graphene films [96, 97], reduced graphene oxide flakes [98, 99] and functionalized graphene [100]. Their operating wavelength was  $\sim 1 \mu\text{m}$ . The most common experimental scheme is to sandwich a GSA between two connectors with a fiber adaptor [95, 99].

#### 1.5.1.6/ TOUCHSCREENS

A touchscreen is an input device layered on top of a visual display that can detect the presence and location of a touch. Since it is a very intuitive and allows a quick interaction with the device it has a large amount of applications, such as cell phones or digital cameras.

There are several kinds of touchscreens but the most common are the resistive and capacitive touchscreens.

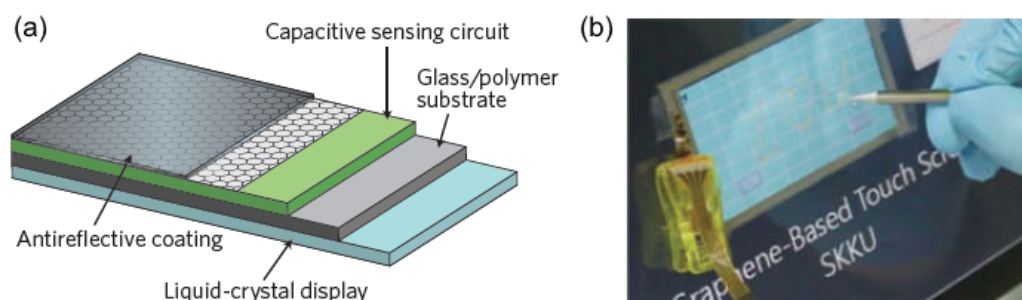


FIGURE 1.20 from ref.[21]. (a) Schematic of a capacitive touchscreen. (b) Resistive graphene-based touch screen.

Resistive touchscreens consist of a conductive substrate, a liquid crystal display front panel and a transparent conductor film (TCF) [101]. When pressing a resistive touchscreen, the front-panel film contacts with the bottom TFC and the coordinates of the contact point are calculated. ITO is mainly used for TCF but it has several limitations due to its cost, brittleness, chemical durability and wear resistance. The use of graphene TFC satisfy all those requirements.

Capacitive touchscreens consist of an insulator such as glass coated with ITO [101]. As the human body is a conductor, when touching the screen it will generate an electrostatic field distortion that can be measured as a capacitance variation. The replacement of ITO by graphene TFC can improve the performance and reduce the production cost.

### 1.5.1.7/ OPTICAL LIMITERS

Optical limiters are devices with a high transmittance for low intensities and reduced transmittance for high intensities. Main applications are in optical sensors and eye protection, since above a certain incident energy threshold the retina can be damaged. Passive optical limiters are simple, cheap and compact, but they are limited because they can not provide protection over the entire visible and near infrared range.

Graphene-based optical limiters absorb light energy converting it into heat, generating microplasmas and bubbles, which results in a reduced transmission.

### 1.5.1.8/ TERAHERTZ DEVICES

THz range is extremely interesting for biomedical imaging, spectroscopy and security. Graphene plasma waves has been determined to be in the THz range [103], which makes graphene a suitable material for THz generation and detection. THz sources based on optical and electrical pumped graphene has been proposed [103]. Experimental demonstration of terahertz emission [104] and amplification [105] in optically pumped graphene has opened the possibility of efficient graphene-based THz source devices. Recent research shows a strong absorption in THz regime in nanopatterned graphene field effect transistor, offering possible applications in far-infrared photodetectors [106]. In addition, the tunability of its electronic and optical properties could allow the development of graphene devices such as modulators, filters, polarizers, beamsplitters and switches working in the THz range.

### 1.5.1.9/ NONLINEAR FREQUENCY CONVERSION

Second-harmonic generation has been reported in graphene films for pulses of 150 fs at 800 nm showing, however, a low conversion efficiency [107]. Four-wave mixing of near-infrared wavelengths has been shown in single- and multilayer graphene [108].

## 1.5.2/ ENERGY APPLICATIONS

In recent years, graphene has been shown to be an efficient base material for energy storage devices. Graphene has been used in lithium-ion batteries, electrochemical capacitors (EC) or novel magnesium-ion batteries. Of special interest are graphene-based electrochemical energy-storage devices. EC can rapidly charge and discharge, but typically they have less energy per unit of volume than conventional batteries. In conventional capacitors, which are made of two layers of conductive material separated by an insulator, the capacitance depends on the surface area of the conductors, the distance between conductors and the electrical permittivity of the insulator. In the case of supercapacitors, a cell coated with porous carbon material is immersed in an electrolyte solution. Graphene is ideal as porous carbon material due to its high surface area ( $2630 \text{ m}^2/\text{g}$ ) and since it is essentially just graphite, it is ecologically friendly, unlike most other energy storage devices. Theoretical capacitance upper-limit of graphene is  $550 \text{ F/g}$ . Experimental results showed capacitances ranging from  $100 \text{ F/g}$  to  $230 \text{ F/g}$  [109]. Energy densities comparable with Ni metal hydride battery have been reported with the advantage that graphene-based capacitors can be charged in tens of seconds [110]. Graphene-based supercapacitors open the possibility of flexible wearable devices [112].



### 1.5.3/ MECHANICAL APPLICATIONS

Graphene has impressive mechanical properties such as low density but a high resistance to compression, superior strength and extremely high in-plane stiffness. Brittle fracture of graphene sheet at critical stress of 130 GPa was reported [30], the highest ever measured in a material. Considering this properties, mechanical applications are being developed. Corrosion-resistive coatings made of graphene are possible thanks to the conduction of the charges responsible for material corrosion. The enhancement of fracture toughness due to graphene inclusion in nanocomposites is expected to produce new functionalities. After a deformation, typically heat, a shape memory (SM) material has the capacity to return to its original shape. Polyurethane (PU) is the most common SM material. Graphene/PU composite material results in a enhanced shape memory, thermal and mechanical properties [113].

Since it has been demonstrated that one-dimensional line defects, such as grain boundaries, can produce decrease on the intrinsic tensile strength of polycrystalline graphene [80], it is expected that defect-engineering by nanopatterning of graphene can offer new functionalities for future mechanical applications. Nowadays, carbon fiber is incorporated into aircraft production since it is strong and light. Graphene is even stronger and lighter and is expected to emerge as a main structural material for aerospace.

### 1.5.4/ ENVIRONMENTAL APPLICATIONS

Water filtering has emerged as an outstanding application of graphene. It has been demonstrated that nanometer-scale pore in single layer free-standing graphene can effectively filter NaCl salt from water. Desalination performance has been determined as a function of pore size, chemical functionalization and applied pressure [136]. Graphene water permeability is several order of magnitude higher than conventional reverse osmosis membranes. Sub-micron scale patterning of graphene is required to develop efficient water filtering devices. Nanopores smaller in the order of 1 nm allow nanoporous graphene to withstand pressures exceeding ten times the typical pressures for seawater reverse osmosis [137, 138].

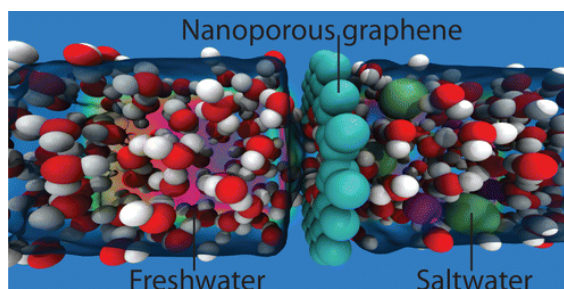


FIGURE 1.21 from ref.[136]. Schematic of a graphene desalination membrane.

## 1.6/ CONCLUSIONS

In this chapter we presented the theoretical background on graphene. We described the main properties of graphene, focusing in optical and electronic properties, which appears to be the most promising for future technologies. Describing a simple tight-binding model,

we showed graphene is a gapless semiconductor with a linear dispersion relation, from where emerges its uniqueness optical and electronic properties. The linear absorption light in graphene is approximately 2.3 % in the infrared for monolayer graphene. Carrier dynamics relaxation shows two timescales (sub-100 fs and  $\sim$  few ps) after light excitation due to different intraband and interband processes. Due to its linear dispersion relation monolayer graphene has a better mobility than multilayer, making single layer graphene an ideal 2D material candidate for optoelectronic applications. Monolayer graphene also the highest tensile strength tested and one of the highest thermal conductivity. We decided to focus our research in single monolayer graphene due to all this characteristics which could lead to outstanding potential applications.

Next step was to consider the best graphene production method. There are mainly two types of methods : exfoliation and chemical methods. The first ones produce graphene with high mobility and few defects, however, dimension and uniformity are not controllable. Methods allowing production of larger areas of graphene are required for industrial scale of graphene based devices. Chemical methods offer an optimum solution. Even if those methods produce a higher number of defects, CVD graphene combines a quality compatible with the optoelectronics applications requirements with production of graphene continuous sheets up to 1 m<sup>2</sup>, so we focused our research on the study of CVD monolayer graphene.

Finally we investigated the state-of-the-art on graphene-based applications, from transparent conductors for touchscreens to saturable absorbers or energy storage applications and we concluded that a technique to pattern sub-micron features in large graphene sheet at fast speed will be a requirement for industrial scale production of most of this devices.

## PATTERNING OF GRAPHENE

In this chapter we describe the state-of-the-art of the techniques to pattern graphene. Concerning graphene devices production, once production of large areas of graphene is achievable, the next requirement to manufacture graphene-based applications at industrial scale is to develop a fast, easily reconfigurable, low cost patterning method. In previous chapter we showed most potential applications, specially in optoelectronics, need patterning and slicing graphene at sub-micron scale. Our motivation is to develop a sub-micron patterning technique to allow a fast lab-to-fab transfer. In the following we present the different methods to structure graphene at sub-micron scale, comparing its strength and disadvantages regarding industrial scale production of graphene-based devices.

### 2.1/ PHOTOLITHOGRAPHY

Photolithography, also called optical lithography or UV lithography, is a microfabrication process to create patterned structures in a substrate. The basis of photolithography is the transfer of a geometric shape patterned on a mask to the final substrate.

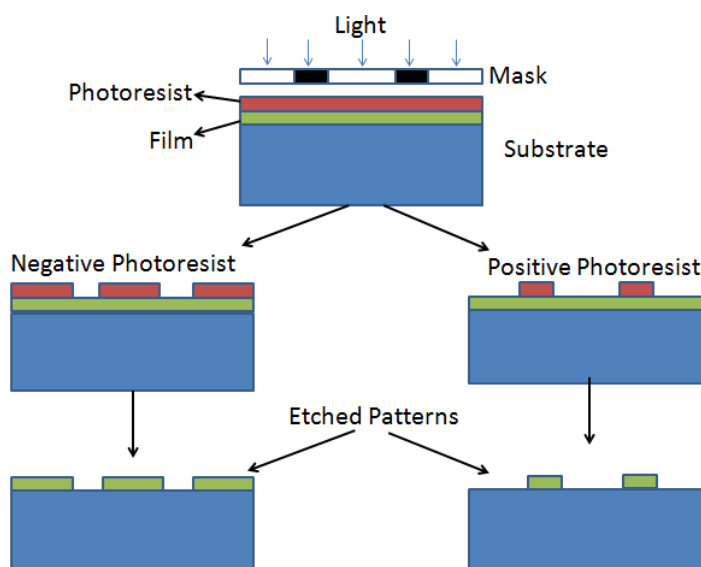


FIGURE 2.1 from [142]. Scheme of the chemical etching (photolithography) process.



The process goes back to 1796 when it was developed as a printing method using ink, metal plates and paper. Modern photolithography uses UV light to image the mask on the substrate using a photoresist layer.

UV lithography requires multiple steps. First the surface has to be cleaned, and during the procedure atmospheric dust has to be minimized, meaning that the complete procedure has to be done in a clean room. Then an adhesion promoter is applied on the surface to enhance its adherence followed by the spin coating of the photoresist on the surface. After a pre-processing backing and the precise mask alignment, the sample is exposed to UV light.

As shown in Fig.2.1, there are two types of photoresist, positive photoresist in which areas exposed to UV light become more sensitive to certain chemical agents, called developers, and negative photoresist, in which exposed areas photopolymerize and become insoluble to the developer.

Once the pattern on the mask has been imprinted onto the photoresist, it is developed, i.e., exposed areas of photoresist are removed (or non-exposed for negative photoresist). Post processing backing and cleaning are required. Next step is etching, where a liquid (wet) or plasma (dry) chemical agent removes the substrate which is not covered by the remaining photoresist. Finally, using a chemical agent that lowers the resist adhesion, it is completely removed from the substrate, which has the desired pattern imprinted on it.

Typical features in photolithography are in the range from 1 to 10  $\mu\text{m}$  [141]. Minimal feature size of  $\sim 250$  nm has been reported on graphene oxide flakes by extreme-UV lithography with a  $\sim 50$  nm illumination wavelength [143]. As shown in Fig. 2.2, uniform graphene nanoribbons of 18 nm wide and 30 nm high were patterned along few microns in highly ordered pyrolytic graphite, which could allow fabrication of functional devices [144]. However, it is a multiple step method which requires vacuum and harmful chemical, making it time consuming, i.e. more than 30 minutes per patterned wafer, and expensive, and as a result not compatible with industrial scale production of graphene-based devices.

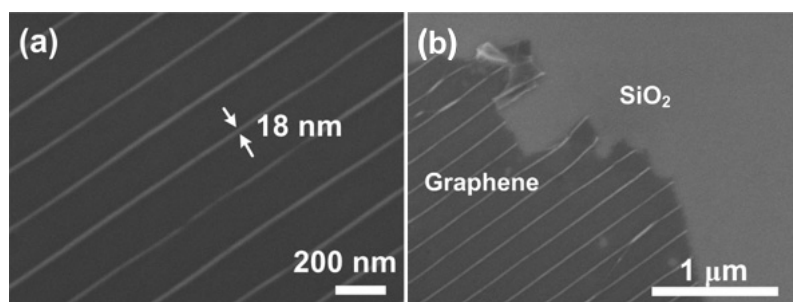


FIGURE 2.2 from [144]. SEM images of (a) UV nanoimprinted graphene nanoribbons array transferred onto  $\text{SiO}_2$  wafer and (b) a layer of graphene sheet attached to graphene nanoribbons array.

## 2.2/ ELECTRON BEAM LITHOGRAPHY

Electron beam lithography arises from early scanning electron microscopes. The working principle consist of scanning a focused electron beam on a surface covered with an electron-sensitive film, called resist. The solubility of the resist changes chemically when exposed to the e-beam, and as a result micro- and nanostructures can be patterned in the resist using software tools. By etching processes, those structures can be transferred

from the resist to the substrate material.

One of the main advantages of e-beam systems is that the resolution is limited by the wavelength of the electrons, which is much smaller than the wavelengths used in optical lithography, so smaller features can be achieved [145]. The maximum resolution is limited by the wavelength as follows

$$d = \frac{\lambda}{2n \sin \alpha} \approx \frac{\lambda}{2NA} \quad (2.1)$$

and the higher the electron energy, the shorter its de Broglie wavelength

$$\lambda_e \approx \frac{h}{\sqrt{2m_0 E (1 + \frac{E}{2m_0 c^2})}} \quad (2.2)$$

On the other hand, e-beam lithography is a multistep process, which requires chemicals, e.g. resist and developing. It is a point-to-point patterning system, making it unefficient for large areas patterning. The interaction between electrons and the resist can produce scattering effects, overexposing certain resist areas and leading to an undesired pattern. Nevertheless, nowadays this technique plays a major role in nanopatterning industry [146].

There are two different categories in e-beam lithography. Conventional e-beam lithography uses scanning electron microscope (SEM) with electron energies up to 30 keV. In transmission electron microscope (TEM) electrons have typical energies in the order of 200 keV, and inherently a higher resolution.

### 2.2.1/ SCANNING ELECTRON MICROSCOPE FOLLOWED BY REACTIVE ION ETCHING

Electron-beam lithography is a common tool for patterning graphene both suspended and on insulating substrates. The most common technique is oxidative plasma etching, which is performed while protecting the desired patterned graphene features with a lithographic mask, allowing patterning in the nanometric range.

Nano-etching of suspended monolayer graphene into nanodevices with resolution down to 7 nm for line-cuts has been achieved using e-beam lithography followed by reactive ion etching. High electronic quality of those nanodevices was confirmed by 2D Raman mapping and transport measurements [147].

Since most graphene applications benefit of its electronic properties, it is crucial to understand the effect of electron irradiation on graphene and graphene devices. In addition, such studies are of interest for future graphene applications of graphene under extreme conditions such as in the presence of charged particles in space. Exposure of graphene to e-beam causes a negative shift of the charge neutral point due to n-doping in graphene caused by the interaction of the energetic electrons with the graphene substrate. In addition, carrier mobilities and minimum conductivity decrease indicating the creation of defects in graphene [148].

### 2.2.2/ DIRECT ETCHING IN TRANSMISSION ELECTRON MICROSCOPE

In a transmission electron microscope (TEM), an image of the sample is formed from the interaction of the electrons transmitted through the specimen. In TEM lithography, those electrons are used to pattern the substrate. TEM lithography has a higher resolution than

SEM lithography because electrons have higher energy. TEM lithography allowed for monolayer graphene interconnections of less than 5 nm [149]. Nanopores of  $\sim 5$  nm diameter in graphene were also reported [151] with a production time of 1 minute per nanopore, which is not time efficient for large areas patterning.

This maskless resist-free electron beam patterning technique is more suitable for nanopatterning at industrial scale. However, maskless lithography using TEM suffers from a relative high cost [150].

## 2.3/ FOCUSED ION BEAM

Ion irradiation is one of the most versatile methods in many areas of material science, specially on modification and construction of nanodevices. Focused ion beam (FIB) is a technique commonly used in semiconductor industry for material ablation. The principle of FIB is similar to the scanning electron microscopy but it uses ions, Gallium ions usually, instead of electrons. A FIB consists of a vacuum chamber, a liquid metal ion source, an ion column, detectors, gas delivery system and a translation stage for the sample.

The  $\text{Ga}^+$  primary ion beam hits the sample ejecting surface material. Removed material can be either secondary ions or neutral atoms. Secondary electrons are also produced by the primary ion beam. Those secondary ions or electrons can be collected to form an image.

Using low current primary ion beam, material removal down to 5 nm diameter is possible [153, 154]. Gallium is the most common liquid metal ion source because its melting point, volatility and vapour pressure are very low. In addition, emission characteristics enable high angular intensity with a reduced energy spread.

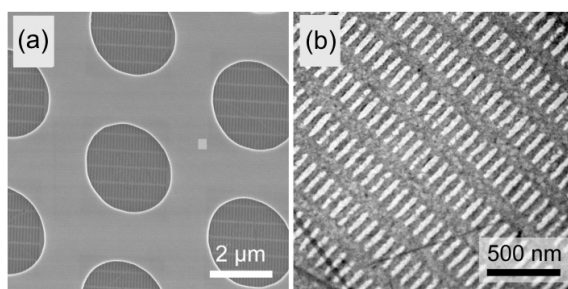


FIGURE 2.3 from [155]. (a) SEM image of TEM grid showing an array of holes with diameters of  $2.5 \mu\text{m}$ . Graphene layer covers the whole area and is suspended over the holes. Visible dark stripes correspond to patterned graphene at a dose of  $4.96 \text{ pC/nm}^2$ . (b) TEM image of pattern written at a dose of  $15.2 \text{ pC/nm}^2$  showing completely removed graphene in white.

Using a FIB source with small ion current and a fast dwell time (fast writing speed), low damage was produced in graphitic structures (few graphene layers). Due to the suitable dwell time, it was possible to write a periodic pattern onto a graphene sheet. In ref. [156] patterning on graphene was performed with a writing speed which could go down to 100 ns per dot and with minimum beam diameter of 7 nm.

Pore size fabrication limited to just below 10 nm with a typical engraving time in the range of milliseconds per spot has been reported in graphene [157]. FIB allows for a high resolution but it is a point-to-point patterning procedure which requires vacuum, which makes it

a costly and not time efficient method for mass production patterning of graphene devices. In ref. [155] suspended graphene sample was patterned over an area of  $30 \times 30 \mu\text{m}^2$  with slits of 100 nm width and 500 nm in about 1 minute, meaning that patterning  $1 \text{ mm}^2$  graphene sheet would require more than 18 hours. In addition, it has been shown that during the the  $\text{Ga}^+$  ions bombardment of graphene layers, ion implantation and backscattering occurs in the sample, resulting in undesired effects such as decrease in the carriers mobility. However, potential future development of FIB technologies could still be promising for industrial microfabrication.

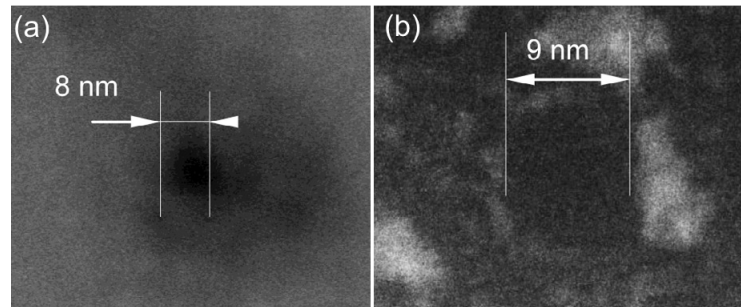


FIGURE 2.4 from [157] SEM images of (a) an 8 nm drilled pore in a mechanically exfoliated graphene flake and (b) a 9 nm drilled pore on CVD growth graphene sheet.

## 2.4/ HELIUM ION LITHOGRAPHY

Scanning Helium ion beam lithography has emerged as a promising fabrication technique for high-resolution nanostructures at high pattern density.

It can be used in imaging applications for materials that would charge under electron beam. Similar to FIB, it performs milling and sputtering, however it shows several advantages respect focused ion beam typically using Gallium ions. Helium ion beam has an ultimate resolution of less than 0.5 nm [158]. In addition, milling and sputtering of soft and fragile materials at low rate are possible.

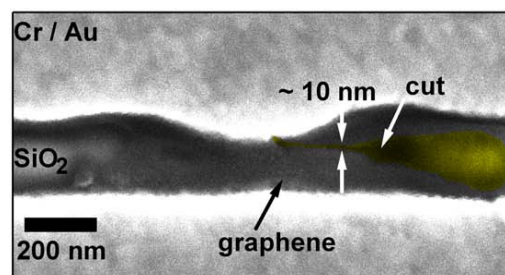


FIGURE 2.5 from [162]. Helium ion microscope image (with false color) of a suspended graphene device after etching with minimum feature sizes of about 10 nm (color online).

Helium ion beam working principle is based on the field ionization of Helium ions using a cryogenically cooled tungsten tip. Helium ion beam is a powerful lithography tool because of its high brightness, low energy spread and sub-nanometric beam size.

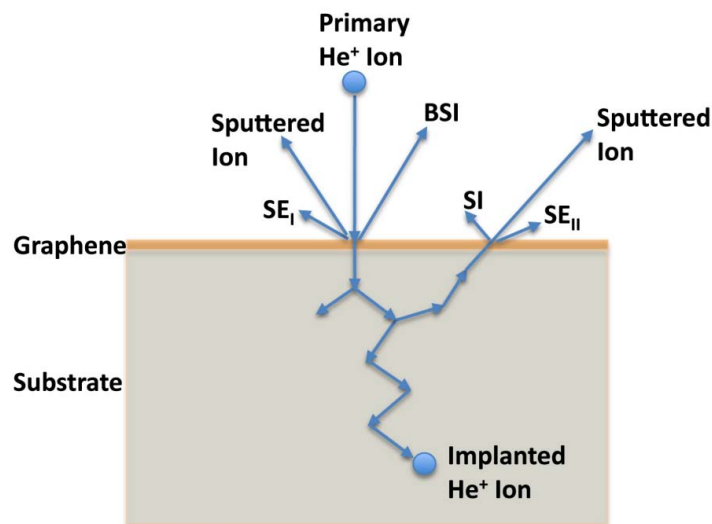


FIGURE 2.6 from [161]. Schematic of the interactions of primary energetic He ions with a graphene layer on SiO<sub>2</sub> substrate, showing the production of secondary electrons (SE<sub>I</sub> at the primary beam and SE<sub>II</sub> at the secondary scattered ion exiting the surface), back scattered ions and secondary ions.

Helium ion lithography fabrication procedure is similar to focused ion beam. Studies in graphene have shown minimum patterned diameters down to 15 nm [161] and minimal etched features size around 10 nm [162]. It has also been reported the application of Helium ion lithography for fabricating functional graphene nanoconductors supported directly on a silicon dioxide layer [163].

## 2.5/ DIRECT LASER WRITING

Direct laser processing of materials is based on laser ablation, which consist on removing material from a solid by irradiating it with a laser beam. The ablation process depends on optical properties of the material, the laser wavelength and its pulse energy and duration. A wavelength with a minimum absorption depth will ensure a high energy deposition in a small volume. Depending on the energy flux of the laser beam, different processes can take place. For low energy flux, the material is heated producing changes in its properties such as its refractive index. By increasing the energy flux the material evaporates or sublimates. If the energy flux is even higher, the material is directly converted into plasma.

After ultrashort pulse excitation, a semiconductor follows a sequence of relaxation stages before going back to equilibrium. Four different regimes can be distinguished : carrier excitation, thermalization, carrier removal and thermal and structural effects. Fig.2.8 illustrates the timescale of the processes within each regime. Fig. 2.9 shows some of the processes that takes place in a typical direct-gap semiconductor. This processes are not a single event sequence but rather they overlap in time.

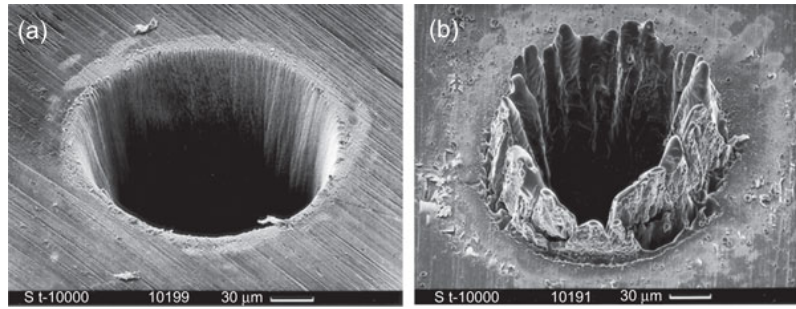


FIGURE 2.7 from [164]. Comparison between (a) femtosecond and (b) nanosecond pulse ablated hole in steel.

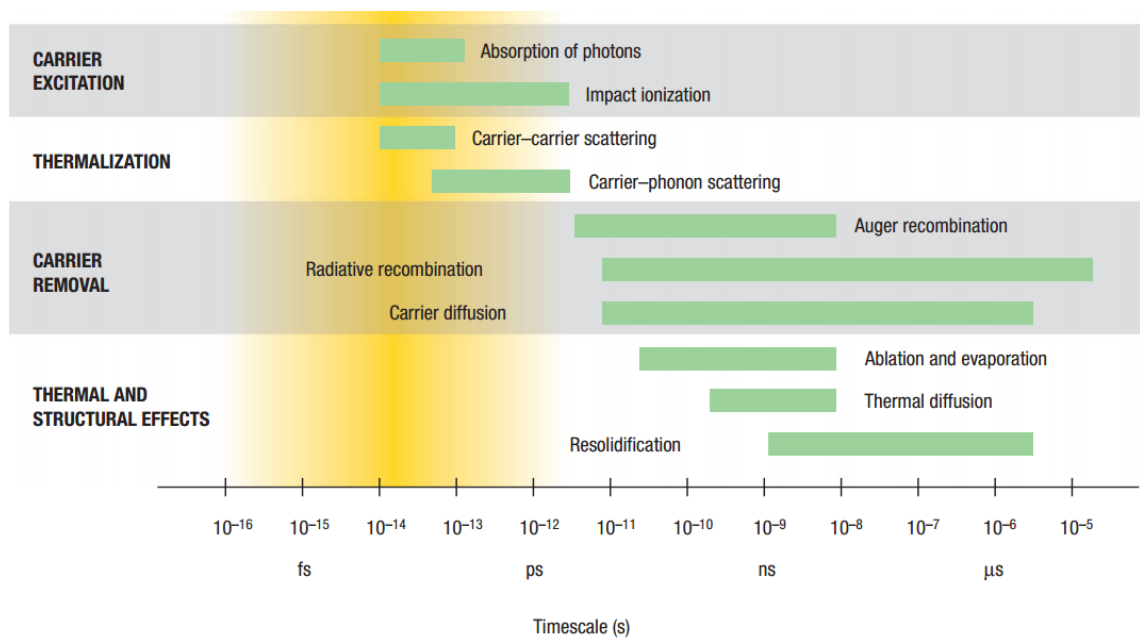


FIGURE 2.8 from [165]. Timescales of various electron and lattice processes in laser-excited solids. Each green bar represents an approximate range of characteristic times over a range of carrier densities from  $10^{17}$  to  $10^{22}$   $\text{cm}^{-3}$ . Yellow colored region corresponds to optical excitation duration in the range  $\sim 1 - 100$  fs

When an optical pulse excites valence band electrons, depending on the photon energy, single or multiphoton absorption occurs. Multiphoton absorption is important when the bandgap is larger than the photon energy or if single photon is not available because of band filling. Absorption by free carriers increase the energy of the electron-hole plasma, or the energy of the initially free electron in a metal. Although this absorption does not increase the carrier density, if the energy of the electrons in the conduction band is high enough above the bandgap it can lead to impact ionization, in which case the carrier density is increased. Assuming the thermalization of the carrier distribution is very fast and that the temperature of the electron and the lattice can be characterized, the thermalization process was modelled as a two temperature diffusion problem [164]. After excitation, the carriers thermalize by carrier-carrier and carrier-phonon scattering in a timescale of few hundred femtoseconds. The different scattering relaxation channels for graphene were described in detailed in section 1.2. It takes several picoseconds before the carriers and



the lattice reach thermal equilibrium. However, although the carriers and the lattice are in equilibrium, there is an excess of free carriers which are removed by electron-hole recombination or diffusion of the carriers out of the excited region.

Short pulse duration maximizes the peak power and minimize thermal conduction to surrounding material. Ultrafast ablation process deposits locally enough energy to have sublimation meanwhile the surrounded material has not been heated, allowing for a more precise and clean patterning than longer pulse durations. As shown in Fig. 2.7, the characteristics of the patterned feature have a strong dependence on the pulse duration. For pulses in the nanosecond range heat diffusion produces melting and creation of burr making it a non reproducible process. The process is also less reproducible because it is highly sensitive to the presence or absence of structural defects. In ultrafast lasers the pulse duration is in the order of the picosecond or shorter. Since the pulse duration is shorter than the energy relaxation time between electrons and the lattice ions, energy can be delivered with a high precision without plasma/screening effects [166, 168]. Sub-100-nm sized photomodified regions have been achieved [169].

The rise in electron density with intensity is generally so fast that there is a threshold over which the avalanche takes place and below which almost no electrons are created. This allows to define the fluence threshold, which is the incident energy per surface unit needed to have ablation in a certain material as shown in Fig. 2.10.

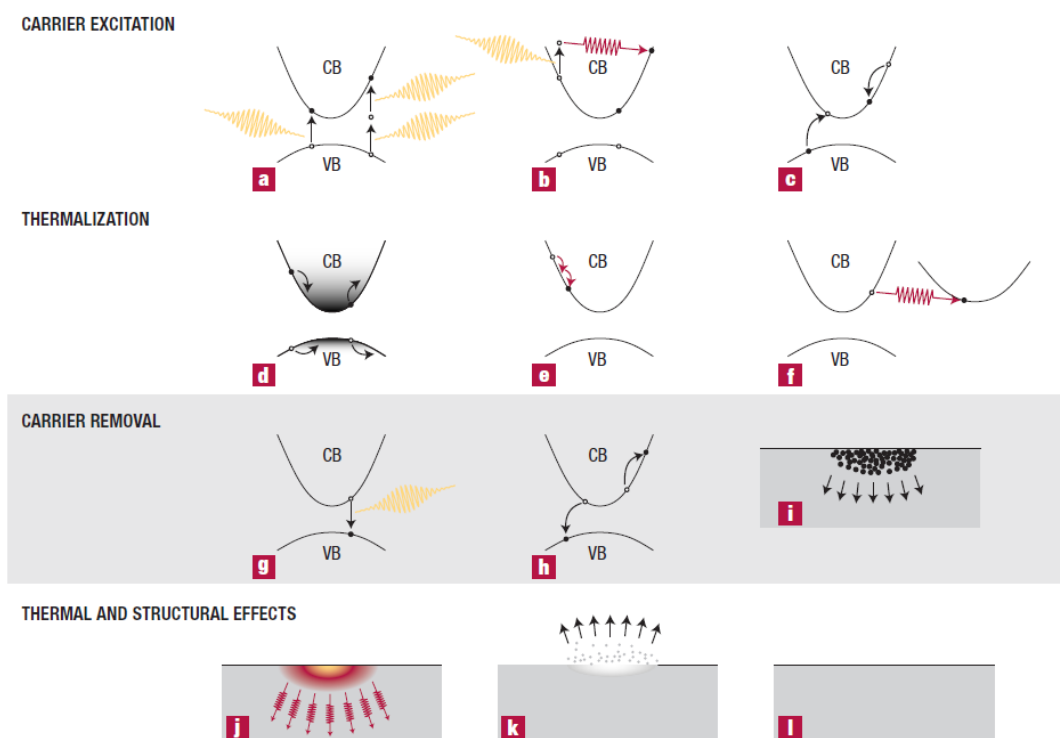


FIGURE 2.9 from [165]. Electron and lattice excitation and relaxation processes in a laser-excited direct gap semiconductor. CB is the conduction band and VB the valence band. (a) Multiphoton absorption. (b) Free-carrier absorption. (c) Impact ionization. (d) Carrier distribution before scattering. (e) Carrier-carrier scattering. (f) Carrier-phonon scattering. (g) Radiative recombination. (h) Auger recombination. (i) Diffusion of excited carriers. (j) Thermal diffusion. (k) Ablation. (l) Resolidification or condensation

Direct laser patterning can operate in both pulsed laser or continuous wave configuration. In the first case, light is emitted in the form of optical pulses. In the latter, the laser is continuously pumped and emitting light. Scanning multishot system has been used typically in laser patterning of structures, however, interference laser lithography has emerged as a promising tool for patterning a complete structure in the order of tens of microns with a single shot [167], thus avoiding shot-to-shot fluctuations or positioning mismatch due to the scanning displacement from point to point.

Our motivation to focus on ultrafast laser processing is to achieve a fast lab-to-fab transfer. Industrial fabrication speed target is  $\sim 10$  cm/min for a linear scan [170]. Ultrafast laser writing of waveguides in Gorilla glass has been already achieved at speeds of  $\sim 200$  mm/s. At this point parallel fs laser processing can have a major role increasing the patterned area in the same time scale.

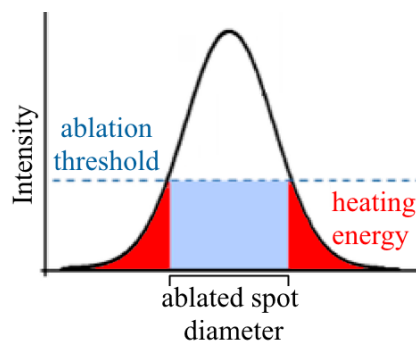


FIGURE 2.10 Schematic ablation threshold in a typical gaussian intensity laser distribution.

### 2.5.1/ LASER INTERFERENCE LITHOGRAPHY

Writing multiple features at a time with the previously described methods typically requires the use of a mask. Laser interference lithography is a simple, quick process over a large area that allows multispot lithography of periodically patterned subwavelength structures at a time without using a mask [171].

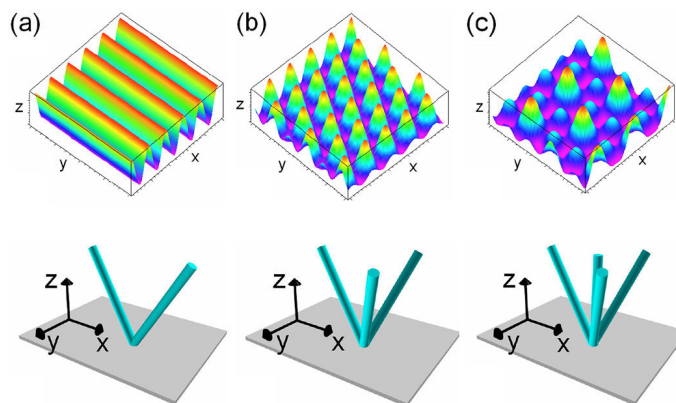


FIGURE 2.11 from [172]. Calculated intensity distribution for (a) two-beam, (b) three-beam, and (c) four-beam interference patterning. The geometrical configurations of the beams necessary to achieve the displayed geometries are also shown.



Laser interference lithography is based on the interference of several coherent beams generating a periodic intensity pattern. As shown in Fig.2.11, two beams interference produce a grating structure, meanwhile three beam interference generate a hexagonal lattice of patterned structures [167]. Interference laser lithography has been already used in nano-electronics, photonic crystals, metamaterials, optical trapping, subwavelength optical elements and biomedical structures [173]. Regarding graphene, it has been reported patterning of graphene scaffolds with pores sizes of  $\sim 500$  nm with laser interference lithography [174].

### 2.5.2/ ULTRAFAST LASER PATTERNING OF GRAPHENE

To understand the importance of ultrafast pulses in materials processing it is necessary to understand the interaction processes between light and matter, the plasma relaxation mechanisms and specially their timescales.

As we describe in Chapter 1, for short pulses there is no equilibrium between the excited electron gas and the lattice vibration during the laser illumination, and as a result the electrons can be highly excited before the coupling with the lattice takes place cooling down the electron gas, and finally a small amount of the incident energy is diffused into the surrounding lattice, which minimizes the thermal effects and allows for a shock-, burr-, and crack-free material removal.

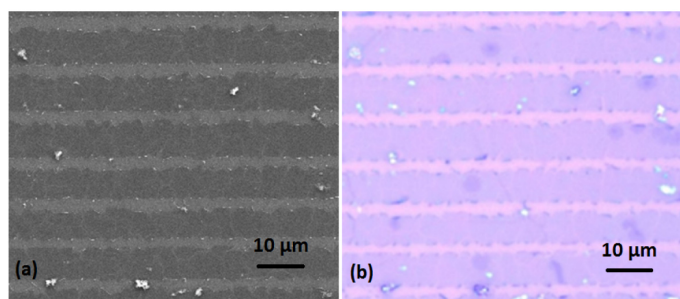


FIGURE 2.12 from [177]. (a) SEM and (b) optical microscope images of a femtosecond laser ablated stripes on a single layer of graphene. Lighter regions are ablated parts.

Single-shot damage threshold of  $I_{th} \sim 3 \cdot 10^{12}$  W/cm<sup>2</sup> has been reported in CVD grown monolayer graphene by using laser pulse excitation ranging from 50 fs to 1.6 ps [196]. Above this threshold, corresponding to a fluence of  $\sim 200$  mJ/cm<sup>2</sup>, a single laser pulse cleanly ablated graphene. Degradation of the lattice over multiple exposures was determined below this threshold.

Two regimes are used in multishot to increase the damage. If the repetition rate is high enough, in the order of 1 MHz repetition rate for femtosecond pulses, the process is called cumulative heat regime, and the heat accumulation effects leads the temperature of the illuminated region to go higher inducing a larger diameter over which the softening is overcome [175]. In repetitive regime the repetition rate is lower and same ablation or damage is expected from pulse to pulse, however the ablation threshold decreases due to incubation processes.

Direct laser writing of microribbons having 5  $\mu$ m width and several mm length in CVD graphene have been reported [176]. No amorphous carbon formation with laser patterning was determined by Raman microscopy.

Nanoscale patterning of CVD graphene without substrate damage has been reported [177]. By adjusting both, the laser fluence around single-pulse ablation threshold of graphene, and the translation speed so there are only a few overlapping pulses at a certain point, 400 nm ablation channels were achieved along 100  $\mu\text{m}$ , showing that ambient conditions maskless nanometer size resolution and periodic structures can be reproduced without substrate damage in a controllable way on graphene single layer.

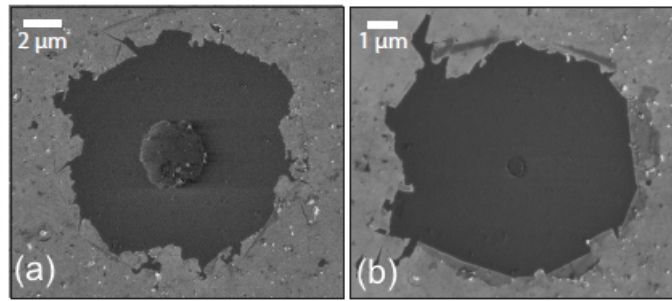


FIGURE 2.13 from [193]. SEM images of (a) microdisk and (b) nanodisk obtained from ablation by 20 superimposed vortex Bessel beam exposures.

Micro- and nanodisks shown in Fig. 2.13 with diameters ranging from 650 nm to 4  $\mu\text{m}$  were fabricated in CVD monolayer graphene using vortex Bessel beams in single- and multishot regime [193]. It was experimentally reported a decrease in the ablation threshold depending on the number of pulses. Ultrafast laser ablation in multishot regime needs to take into account certain considerations. After the arrival of the first pulse, due to the presence of defects some regions are more absorbing and nano-antenna effects can take place at those points producing a threshold lowering known as incubation process. Plasma expansion in air can affect to the next incoming pulse leading to plasma shielding.

Using shaped laser beams, such as  $\text{TEM}_{01}$ , and scanning the graphene sample allowed for shaping graphene beyond diffraction limit [179]. With this method graphene nanoribbons down to  $\sim 35$  nm were patterned on exfoliated graphene flakes as illustrated in Fig.2.14, in this procedure local heating burns graphene causing oxidation and conversion into  $\text{CO}_2$ .

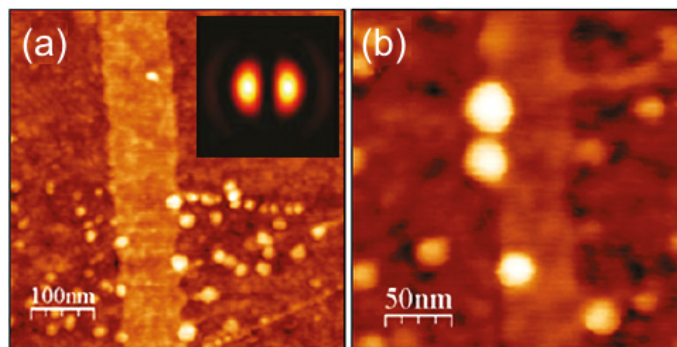


FIGURE 2.14 from [179]. AFM images of graphene nanoribbons of (a) 80 nm and (b) 35 nm width. The inset shows schematically the  $\text{TEM}_{10}$  laser beam profile used for patterning.

Beam shaping of ultrafast pulses based on multiple beam interference open the door to massive parallelization, allowing patterning of structures over an extended area in single pulse regime. Large area single-shot patterning has several advantages, such as a patterning speed compatible with industrial scale fabrication, minimizing of positioning error and pulse-to-pulse fluctuations, as it is described in more detail in the next chapter.

## 2.6/ CONCLUSIONS

In this chapter we presented the state-of-the-art in patterning graphene techniques. These techniques include lithography using light, electrons or ions, and direct laser writing.

Lithography has become one of the most powerful processes in the electronics and optoelectronics research and industry. Photolithography, sometimes called optical lithography, in which the substrate covered with the resist is exposed to UV light through a mask plate where the desired pattern is engraved has a resolution limit determined by the wavelength of the light used. Minimal features of  $\sim 50$  nm were reported [139]. However, for some applications better resolution is needed, so a different type of lithography which is based on particle irradiation was developed. In addition, optical lithography is a time consuming multistep procedure incompatible with large scale production. Irradiated particles can be electrons or ions, since the wavelength corresponding to electrons is shorter than light used in photolithography and it has higher intrinsic resolution. Using of a focused beam of particles allows for precise control of the irradiated zone, so no mask is needed to block light illuminating certain areas. This techniques have a precision down to few nanometers, but graphene quality is decreased and it is a point-to-point procedure not convenient for large areas patterning.

Using conventional electron-beam lithography using scanning electron microscope (SEM) a maximum resolution of tens of nanometers was reported[140]. The transmission electron microscope (TEM) electron beam has a higher resolution but a low time efficiency.

Finally we considered laser patterning. Due to its characteristics including maskless, non-contact, dry patterning, and also the possibility of high reproducible large area patterning at sub-micron scale, laser patterning has emerged as a key-enabling tool. Of special interest is ultrafast laser patterning, due to its high peak power and low thermal effects in the surrounding area. In addition, the use of parallel laser processing allows large area patterning with a single laser pulse.

Unlike multistep lithography, this laser method is a single step laser ablation process, making it an ideal candidate for patterning at industrial scale. These characteristics motivated us to focus on single shot ultrafast laser as an appropriate solution for the nanoscale patterning required to produce graphene-based devices at industrial scale.

## EXPERIMENTAL SETUP

This chapter gives the background and technical description of the experimental setup. First, the ultrafast laser system used in the presented experiments is briefly described. Secondly, the beam shaping methods used to generate Bessel beams and hexagonal array of beams are discussed. The experimental beam characterization technique is explained in detail. It includes the pulse energy characterization and pulse intensity distribution imaging, which is crucial to our methods to determine graphene ablation threshold. Different types of samples investigated are described together with the positioning procedure and the laser processing techniques applied. Finally, sample post-processing characterization methods used are presented.

### 3.1/ OVERVIEW OF THE SETUP

The beam forming part of the experimental setup is schematically represented in Fig. 3.1. The interference beam generated after the SLM is demagnified at a 4f system. The setup also includes a spatial Fourier filtering. In the case of no sample, the beam intensity along propagation is determined by calibrating the response of a high-dynamical range (16 bits) CCD camera after another 4f system.

The experimental setup consists in a beam forming section where the gaussian pulse output from the laser amplifier is transform into the desired beam distribution, a sample observation system allowing in-situ visualization of the sample alignment and processing processes, a sample positioning system for precise sample-to-beam positioning, and finally a beam characterization setup to determine the fluence beam distribution along propagation.

### 3.2/ FEMTOSECOND LASER SYSTEM

We used a Ti :Sapphire regenerative amplifier laser system which amplifies individual laser pulses that are separately produced in a mode-locked Ti :Sapphire laser. As illustrated in Fig.3.2, the laser system is composed of a seed oscillator (Mai Tai), a pump laser (Empower), and an amplifier system (Spitfire), all of them from Spectra Physics. The system also comprises the Timing and Delay Generator (TDG) control unit, which provides the timing needed to synchronize the Pockels cell to the passage of the pulse through the amplifier.

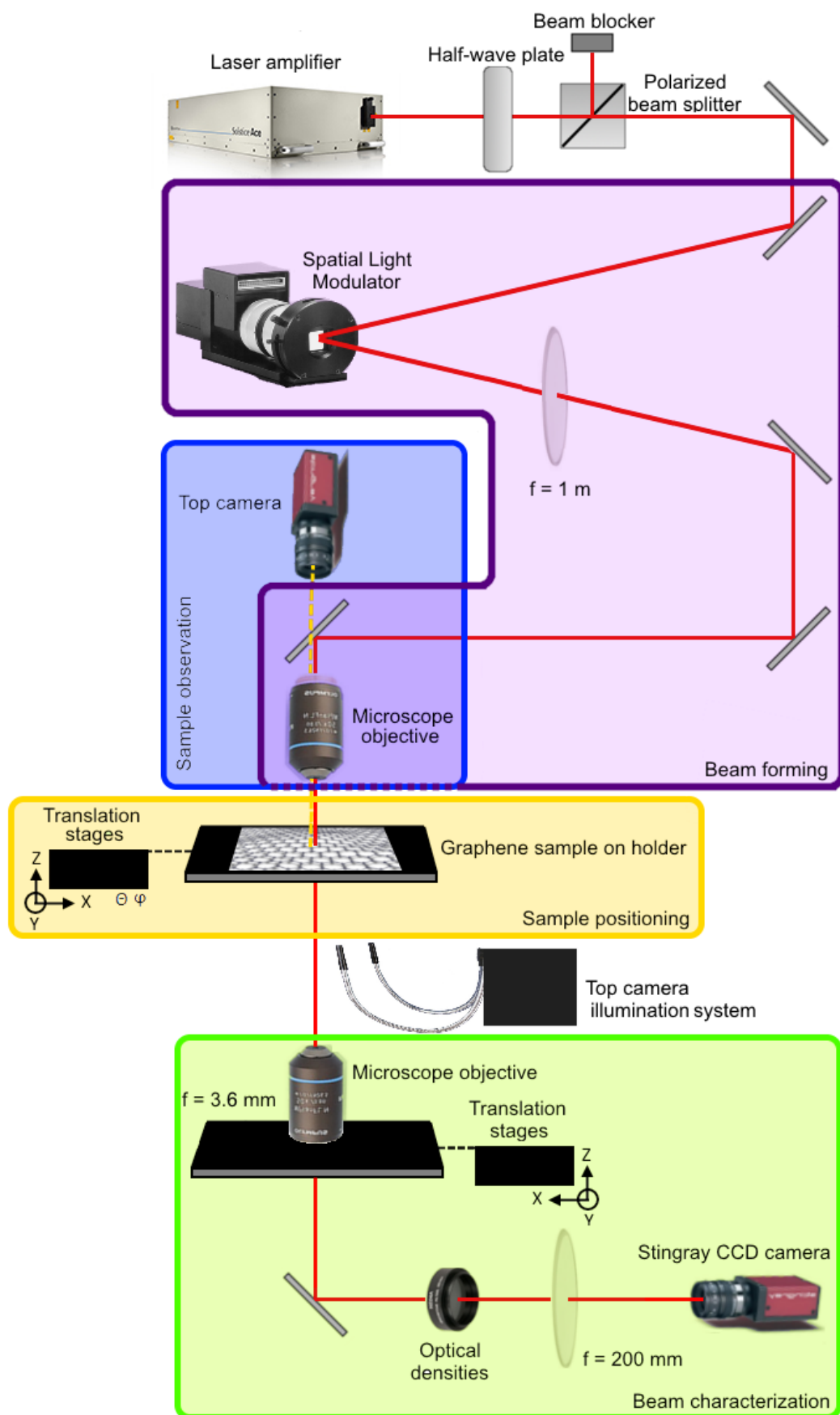


FIGURE 3.1 Scheme of experimental setup used to image the beam in air removing the graphene sample and to pattern the graphene sheet.

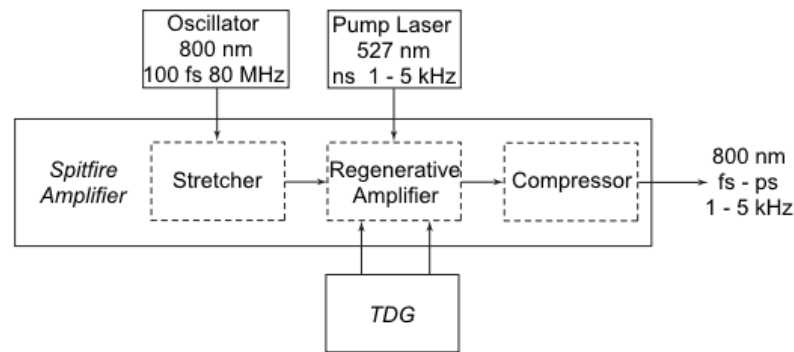


FIGURE 3.2 Block diagram for the laser system.

First, the oscillator (Mai Tai) produces femtosecond pulses at low energy by mode-locking. The oscillator is pumped by a diode laser at 532 nm. Output pulses are produced at a repetition rate of 80 MHz, with a central wavelength of 800 nm and pulse duration of 100 fs. To increase the peak power of the ultrashort output pulses of the oscillator, the pulses are sent to the Spitfire which amplifies them by chirped pulse amplification. Chirped pulse amplification consists in three steps, in order to avoid nonlinear effects in the amplifier crystal such as self-focusing. First, The pulse arriving from the oscillator is initially stretched in time to decrease its peak power reducing the probability of damaging the Ti :Sapphire amplifier crystal. Second step is pulse amplification in a regenerative cavity. It consists of a slave Ti :Sa laser, pumped by nanosecond pump. This Q-switch pump laser delivers an average output up to 45W at 527 nm, with a repetition rate of 1 kHz and 5 kHz. The pump laser (Empower) transfers a synchronous energy pulse to the Ti :Sapphire crystal just before the arrival of the seed pulse. As a result, the seed pulse generates stimulated emission in the excited crystal leading to the amplification of the stretched pulse. The last step is to compress the stretched amplified pulse back to femtosecond pulse duration. An external Pockels cell with a polarizer is used as pulse picker allowing for precise controlled operation in single-shot mode and removes the low-intensity leakage from the regenerative cavity.

### 3.3/ LASER BEAM CHARACTERIZATION

In our experiments, precise control of the incident energy and its intensity spatial distribution are critical parameters to determine the ablation threshold and to control patterning of graphene. The beam was characterized following three steps : knife edge measurement of the Gaussian beam before the beam shaping system, pulse energy characterization at the sample position and beam imaging along its propagation axis.

#### 3.3.1/ PULSE DURATION CHARACTERIZATION

We proceed to a frequency-resolved optical gating (FROG) measurement to determine the pulse duration. FROG technique consist on splitting the pulse in two and then overlapping them in a non-linear medium allowing spectrally resolving the signal pulse in an autocorrelator-type system.

We performed the FROG measurement using a Phazzler from FASTLITE. In the



Phazzler, all the linear operations are performed by the Dazzler ultrafast pulse shaper instead of using beam splitters, mirrors, translations stages and gratings. As shown in Fig.3.3, the Dazzler is an acousto-optic programmable dispersive filter which relies on a longitudinal interaction between an acoustic wave and an optical wave in the bulk of a birefringent crystal. The acoustooptic signal, which can be considered static in front of the light pulse, causes diffraction of the laser beam. The pulse duration at the output of our laser system could be tuned by changing the grating pair separation in the amplifier.

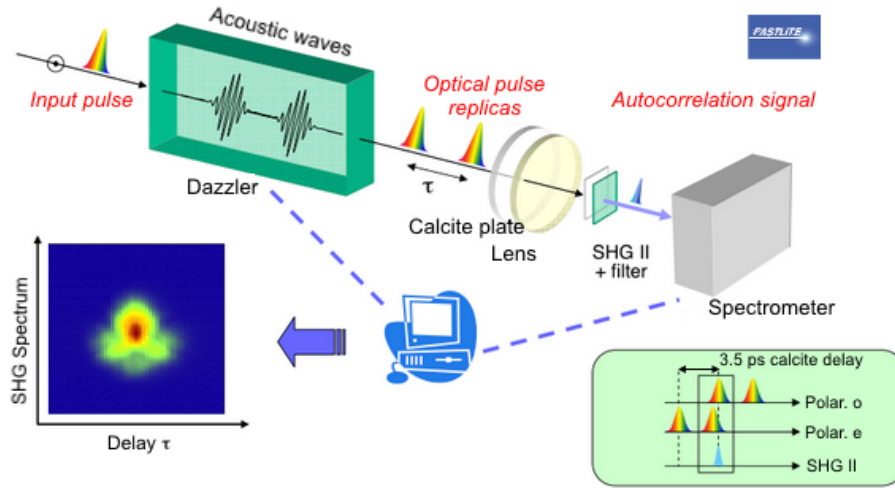


FIGURE 3.3 Scheme of the Phazzler FROG working principle.

The FROG measurement illustrated in Fig.3.4 was done for grating pair separation values within a range of 6 mm and pulse durations from 130 fs to 3 ps were determined.

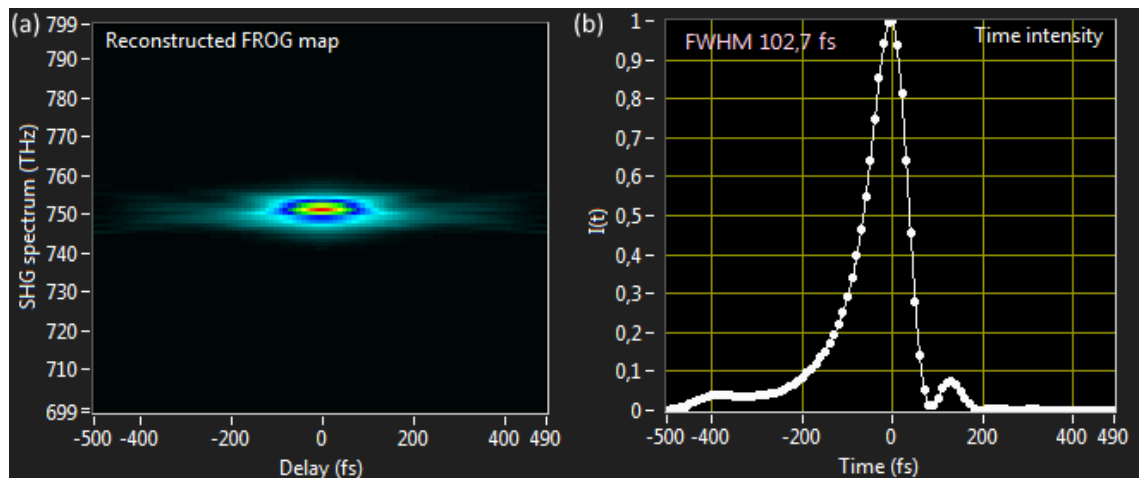


FIGURE 3.4 (a) Experimental FROG trace and (b) reconstruction of the pulse for pulse duration of 100 fs.

Optical elements produce dispersion in the ultrashort pulse, since we wanted to have a maximum compression of the pulse at the sample position, a two-photon absorption measurement was done to characterize the dispersion of the different optical elements

in the setup, such as microscope objectives. After the dispersion characterization the pulse could be over compressed at the laser system output in order to compensate for the dispersion along the optical path.

### 3.3.2/ BEAM RADIUS CHARACTERIZATION

The measurement of the transverse profile of the laser beam was done by the knife edge method. It allowed us to determine the initial beam waist arriving to the SLM.

The knife edge consist in recording the total power of the beam as a knife edge (blade) is translated through the beam perpendicular to its propagation direction by using a calibrated translation stage. The gaussian beam is focused by a lens and after the focus plane a photodetector measures the power. The whole beam needs to be incident into the photodiode as illustrated in Fig. 3.6. The measured power goes from its maximum value when the beam is not covered to its minimal when the blade covers the whole laser beam. A correlation between the measured power and the knife edge position can be obtained. By fitting the measured data to the next equation the beam waist can be retrieved,

$$P = P_0 + \frac{P_{max}}{2} \left( 1 - \operatorname{erf} \left( \frac{\sqrt{2}(x - x_0)}{w} \right) \right) \quad (3.1)$$

where  $P_0$  is the background power,  $P_{max}$  is the maximum power corresponding to completely uncovered beam,  $x_0$  is a position with the half of the real power,  $\operatorname{erf}$  is a standard error function, and  $w$  is the beam radius.

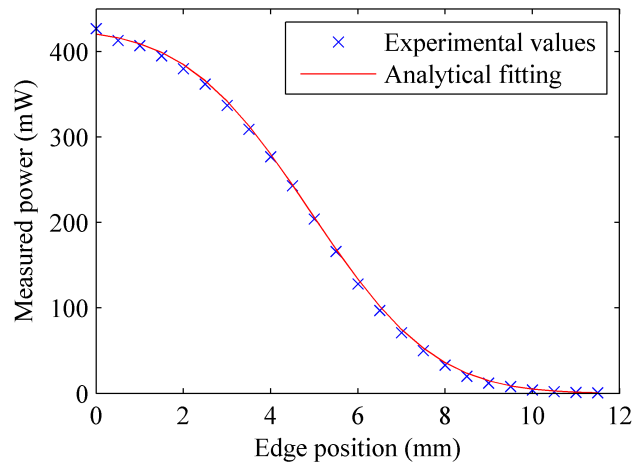


FIGURE 3.5 Experimental power values (blue) and fitting corresponding to a beam waist value of 4.50 mm.



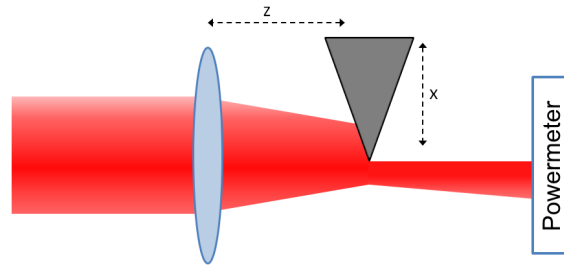


FIGURE 3.6 The principle of knife edge method.

### 3.3.3/ PULSE ENERGY CHARACTERIZATION

Accurate characterization of the pulse energy is imperative to control laser processing of any material. A Pockels cell is an electro-optic device acting as a voltage-controlled waveplate based in the Pockels effect, a linear electro-optic effect where the refractive index of a material is modified as a function of the applied electric field. By placing a Pockels cell, containing an electro-optic crystal, followed by a half wave plate between the Ti :Sapphire amplifier laser output and the experimental setup input, the pulse energy arriving to the setup can be precisely controlled by the voltage applied to the Pockels cell. We characterized the pulse energy by placing a power meter at the sample position and modulating the applied command voltage at the Pockels cells between 0 V and 4.5 V, which is the accessible range in our setup. No optical density filter was placed in the optical path during the power characterization. We implemented a Matlab code which records the measured power after each step increase in the Pockels cell voltage.

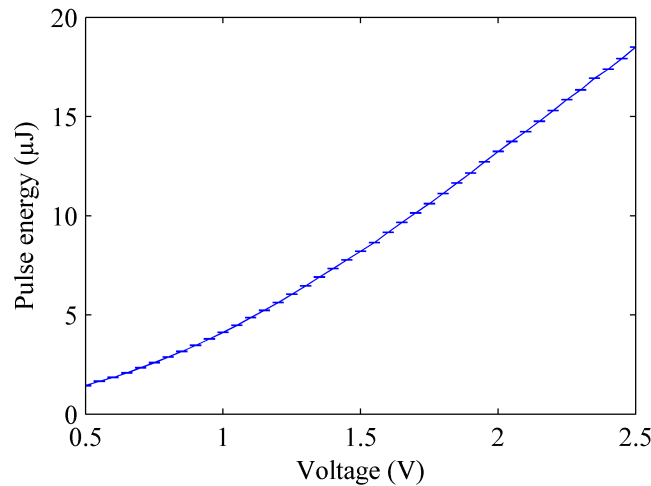


FIGURE 3.7 Typical pulse energy characterization at the sample site as a function of the applied command voltage at the Pockels cells.

In order to increase the range of available pulse energies, optical filters can be used. By setting a fixed voltage and measuring the power placing different optical densities we characterized the ratio between filters as shown in Table 3.1

Figure 3.7 shows the power measurement for voltage between 0.5 V and 4.0 V with no optical density corresponding to a pulse energy range from 1.4  $\mu\text{J}$  to 18.5  $\mu\text{J}$ . The range

of accessible pulse energies by using different optical densities allows us to go further down to pulse energies of 4 nJ.

Independently, the pulse to pulse energy variation was characterized at less than 2% with a photodiode used in the linear regime.

Optical Density	Transmission ratio
10	0.148
20	0.036
30	0.009

TABLE 3.1 Ratio between measured powers with different OD compared with the measurement without filters.

### 3.4/ BEAM SHAPING

Applications in many different fields require a specific intensity beam distribution at a certain plane along its propagation. Such applications include laser-material processing, laser-material studies, fiber injection systems, optical data and image processing, lithography or medical applications. In our experiments, it is very convenient since beam shaping consists in transforming a Gaussian beam in any other type of shaped beam by redistributing its irradiance and phase. Laser interference lithography using multiple-beam interference allows producing a huge number of interference patterns with different geometries.

There are several methods to shape laser beams using refractive, reflective or diffractive optics. In our experiments we use phase only modulation with a reflective Spatial Light Modulator (SLM). It allows us to generate different types of intensity beam distributions at the plane of interest, where later the sample to be patterned will be placed.

We use two different beam shapes according to which suits best to determine the properties or phenomena we want to investigate : a cylindrically-symmetric "non-diffracting" Bessel beam and a "non-diffracting" hexagonal array beam.

#### 3.4.1/ SPATIAL LIGHT MODULATOR

The SLM is an active optical element allowing the modulation of light both in phase and amplitude. There are different SLM configurations, where light can be modulated in transmission or in reflection. In this section we focus on the last ones since reflective SLM is used in the presented experimental results.

The active surface of the SLM consist of a pixel matrix. Each pixel is made up of liquid crystal between two surfaces, a transparent frontal and a reflective back one. In the market it is possible to find SLM using a variety of liquid crystals, although the most common is nematic liquid crystal.

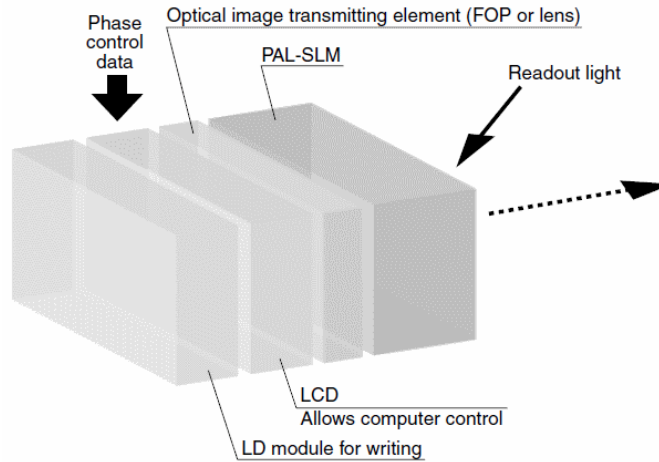


FIGURE 3.8 Schematic SLM configuration.

The SLM working principle takes advantage of the property of molecules in liquid crystal by which they are orientable under an electric field. The anisotropic shape of the molecules induces a birefringence, depending on the applied voltage on the crystal.

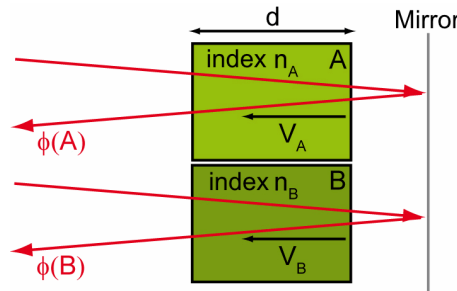


FIGURE 3.9 from [181]. Schematic phase modulation principle using a SLM showing the difference in phase produced by two adjacent pixels.

As an example we consider two adjacent pixels where we apply two different tensions, which produce two different crystal orientations. As a result, the incident beam propagates in medias with different refractive indices,  $n_A$  and  $n_B$ . The different phase  $\phi_{A/B}$  after the reflection on the pixels, causes a different optical path  $\delta$ , with  $\phi_{A/B} = \frac{2\pi\delta}{\lambda}$  and  $\delta = 2d(n_A - n_B)$  and  $d$  is the pixel thickness. An arbitrary phase modulation can be applied by adapting the tensions on the SLM pixel matrix.

The discretized phase is quantified over 8 bits which results in a total of 256 grey levels, corresponding to a minimal phase variation of  $\delta\phi \geq 0.02 \text{ rad}$ . If the phase distribution exceed  $2\pi$ , then we use the wrapping operation :  $\phi \rightarrow \phi[2\pi]$  because  $e^{i\phi} = e^{i\phi+2\pi}$ .

One of the main advantages of using SLM compared to other beam shaping systems is the ease to change its configuration parameters. It is extremely convenient in our studies since we work with three different beam shapes : Bessel beam order zero and order one, and a multi-spot hexagonal array intensity distribution.

On the other hand, very high intensities incident onto the SLM screen could damage it, so in that case other beam shaping systems would be more appropriate, for instance using real axicons to generate Bessel beams. In the intensity range of our experiments it

is not a limitation since we are far below the SLM damage threshold.

The SLM used in our experiments is Hamamatsu X8267. The technical characteristics are in Tab.3.2. Fig.3.9 shows schematically the SLM phase modulation.

TABLE 3.2 Technical characteristics of the SLM serie X8267.

Features	Value
Active cell	20 mm-side square
Number of pixels	768 by 768
Pixel size	26 $\mu\text{m}$ -side square
Quantification level	256 (8 bits)
Numerical aperture	0.1
Phase modulation level	2.4 $\pi$

### 3.4.2/ BESSEL BEAM

Non-diffractive beams such as Bessel beams maintain a constant intensity distribution along its propagation axis. The transverse electric field of an infinite Bessel beam along its propagation can be expressed as

$$E(r, \phi, z) = A_0 J_n(k_r r) \exp(ik_z z) \exp(\pm i n \phi) \quad (3.2)$$

where  $r, \phi$  and  $z$  are the radial, azimuthal and longitudinal components respectively [182].  $A_0$  is the amplitude of the electric field,  $J_n$  is the  $n^{\text{th}}$  order of the Bessel beam,  $k_r$  and  $k_z$  are the radial and longitudinal components of the wave vectors, which are related by  $k = \sqrt{k_r^2 + k_z^2}$ . In the case of zero-th order Bessel beam, with  $n = 0$ , the electric field can be expressed as :

$$E(r, \phi, z) = A_0 J_0(k_r r) \exp(ik_z z) \quad (3.3)$$

Since ideal Bessel beam would have an infinite transverse extension and an infinite energy, they can not be generated experimentally. Only 'apodized' versions can be generated, which still have the property of an invariant lobe size. These quasi-bessel beams will be referred to as "Bessel beams" in the rest of this document. Bessel beams can be generated by different methods, such as the use of an axicon or SLM. In our experiments Bessel beams were generated by implementing a phase mask on the SLM which introduces a phase mask corresponding to an axicon with the required characteristic angle.

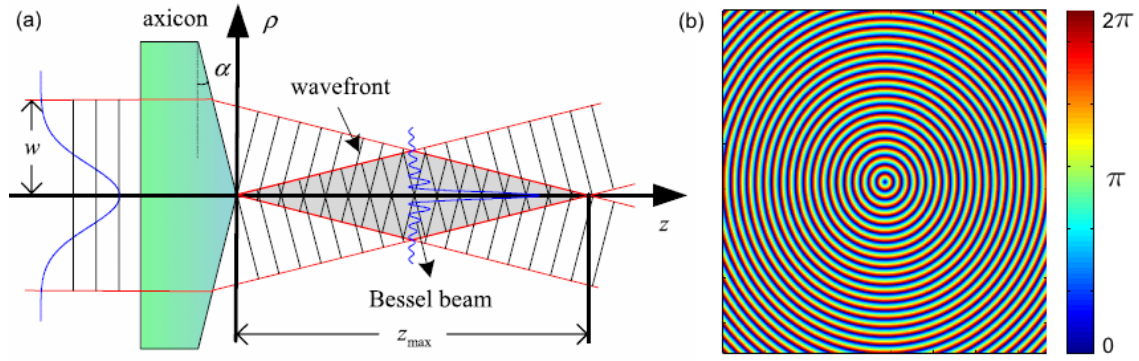


FIGURE 3.10 (a) from [183] schematic of a quasi-Bessel beam generation with an axicon. (b) Phase mask implemented in the SLM in order to generate a zeroth-order Bessel beam from an incident gaussian beam. The color scale has 256 levels corresponding to phase shift values between 0 and  $2\pi$ . No tilt term is applied in this phase mask.

Once the phase mask is applied at the SLM, the beam deviates towards the propagation  $z$ -axis with a certain conical angle and creates a cylindrically-symmetric interference field, i.e. a zero-th order Bessel beam in the case  $n = 0$ . Of special importance is the conical angle, i.e. the angle between the light outgoing the SLM (or real axicon) and the longitudinal propagation axis  $z$ . It will determine the length of the Bessel zone, which is the region along the which the beam interference generates the Bessel beam, and the lobe diameter. The intensity peak along propagation is described [184] by Eq. 3.4.

$$I(z) = \frac{8\pi P_0 z \sin^2 \theta}{\lambda_0 w_0^2} \exp\left[-2\left(\frac{z \sin \theta}{w_0}\right)^2\right] \quad (3.4)$$

The transverse intensity in the main lobe can be approximated by

$$I(r, r) = I(z) \left| J_0\left(r \frac{2\pi}{\lambda} \sin \theta\right) \right|^2 \quad (3.5)$$

As it will be shown in next sections, the intensity peak position is a key parameter in our experiments.

### 3.4.3/ HEXAGONAL ARRAY BEAM

In our experiments concerning multispot ablation with a single shot at sub-micron scale, we need to implement on the SLM a phase mask with a set of parameters generating an interference pattern array with a large number of spots, with intensity lobe diameters in the order of  $1 \mu\text{m}$ , and with a long non-diffracting range.

Our solution is to produce an hexagonal array beam by implementing a 3-beam interference phase mask at the SLM, allowing us to generate between 40 and 60 intensity peaks with variable diameters from a single incident laser pulse. This procedure opens the possibility of patterning a large number holes in a target substrate with a single laser shot.

The phase mask implemented on the SLM is divided in three equal sections of  $120^\circ$  centered at  $(x, y) = (0, 0)$  as shown in Figure 3.11. In each section the phase mask is defined introducing a phase shift that controls the wave vector independently of the other sections. The critical constraint is the tilt angle of the phase mask which will define the

periodicity of the interference pattern along propagation. The phase mask implemented on the SLM determined the wave vector direction of each of the three sections. We define the wave vector so the three sections of the beam after the SLM converge towards the propagation axis with a certain angle generating the expected interference pattern. From the imposed geometrical constraints we derived the wave vectors of three beams,

$$\vec{k}_1 = k(0.5 \sin\theta, \sqrt{\frac{3}{4}} \sin\theta) \quad \vec{k}_2 = k(-\sin\theta, 0) \quad \vec{k}_3 = k(0.5 \sin\theta, -\sqrt{\frac{3}{4}} \sin\theta) \quad (3.6)$$

which are consistent with previous studies [185]. After numerical calculations, the analytical formula which relates the tilt angle of the beams after the SLM can be deduced from that set of Eq.3.6,

$$period = \frac{\lambda}{1.5 \cdot \sin(\alpha)} \quad (3.7)$$

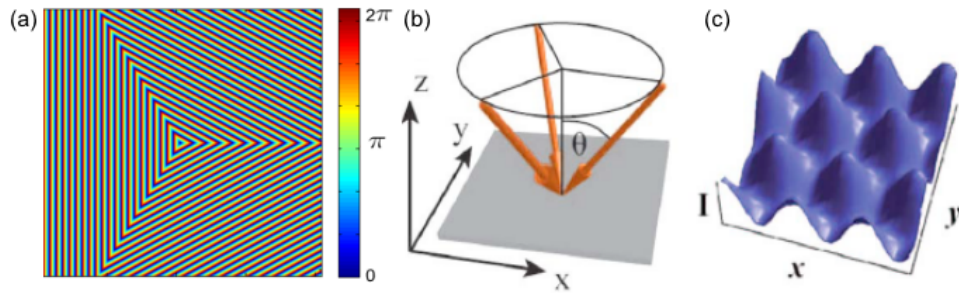


FIGURE 3.11 (a) Phase mask loaded at the SLM to generate the three-beam interference pattern. From [185] (b) three-beam interference geometry and (c) three-beam interference pattern intensity.

First, we evaluate the invariance of the periodicity between the intensity peaks of the pattern along propagation, i.e. its non-diffractive nature, for a fixed set of parameters. Pulse energy and duration, beam diameter and tilt angle were fixed and the propagation of the three beams interference after the phase mask was simulated.

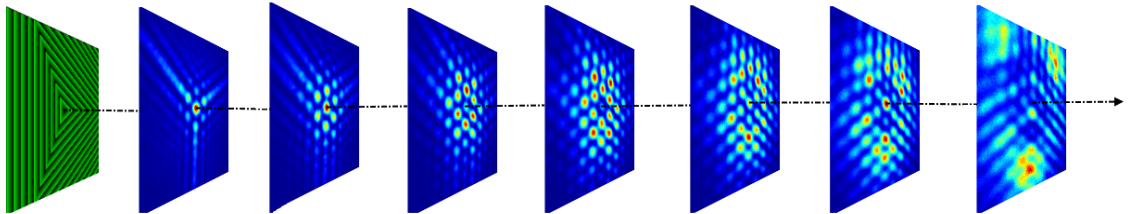


FIGURE 3.12 The periodicity of the intensity peaks in the interference pattern is constant along the propagation axis even if the respective intensities slowly evolves.

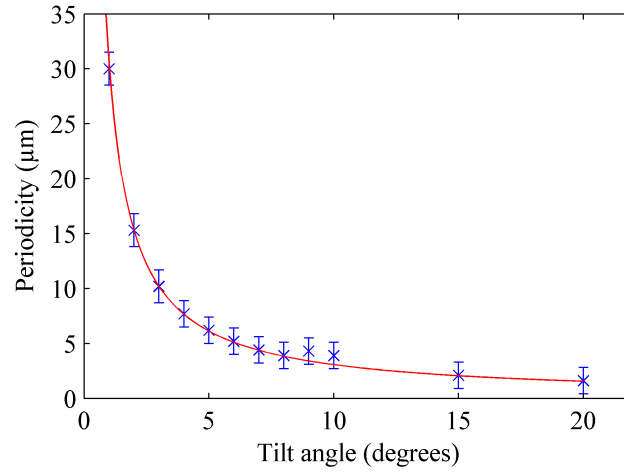


FIGURE 3.13 Numerical (blue) and analytical (red) interference pattern periodicity as a function of the tilt angle for fixed energy pulse, beam diameter and pulse duration.

The intensity distribution changed along the propagation axis but the period of the interference pattern along the optical axis was constant for any fixed tilt angle value as shown in Fig.3.12 .

Second, we determine the relation between the tilt angle at the phase mask and the periodicity of the interference pattern. We simulated beam propagation after the phase mask for tilt angles between 1° and 20° as shown in Fig. 3.13.

Analytical expression in Eq.3.7 and numerical simulation of the periodicity in terms of the tilt angle at the phase mask are shown in Fig.3.13, with a good matching between both results.

A 4f-system allows us to transfer the interference pattern generated after the SLM to the sample position with a certain demagnification as shown in Fig.3.14.

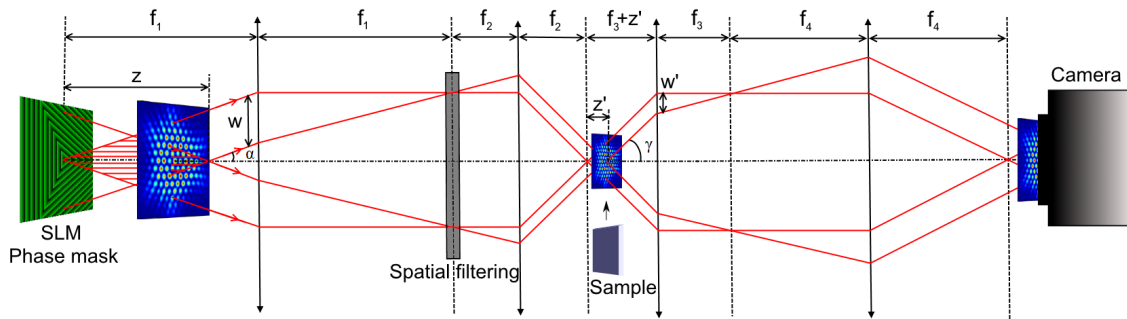


FIGURE 3.14 Experimental setup. The lens and microscope objective form a 4f telescope that demagnifies the beam and increases the waves crossing angle. Spatial filtering allows for eliminating unmodulated zero-th order from the Spatial Light Modulator (SLM).

To select the optimum set of parameters for patterning an hexagonal array of holes, we have to consider the next geometrical relations between the hexagonal pattern generated after the SLM and its projection at the sample position.



$$\begin{aligned}
 M &= \frac{f_1}{f_2} & \tan \alpha &= \frac{1}{M} \tan \gamma \\
 z &= \frac{w}{\tan \alpha} & z' &= \frac{1}{M^2} z & w' &= \frac{1}{M} w
 \end{aligned} \tag{3.8}$$

where  $z$  is the interference pattern region after the SLM,  $z'$  is the interference pattern region after the 4f system where the sample is to be placed,  $w$  is the beam radius incident onto the SLM, equivalent to the maximum transverse length of the interference pattern,  $w'$  is the beam radius after the 4f system, corresponding to the maximum transverse length of the interference pattern at the sample position. In our experimental setup  $f_1 = 1$  m and  $f_2 = 9.0$  mm.

Next, a second 4f-system was implemented after the sample position to record the beam image on a CCD camera. The camera and the Pockels cell at the laser system output were synchronized. By moving a microscope objective along the propagation axis, the beam intensity profile was scanned in air. The translation stage holding the microscope objective moved one step, then the camera shutter opened during  $2000 \mu\text{s}$ , a single laser pulse was sent through the Pockels cell and the intensity distribution at the focal plane of the microscope objective could be recorded in the CCD camera. By repeating this procedure moving in steps along the propagation axis, the complete intensity profile of the beam was scanned.

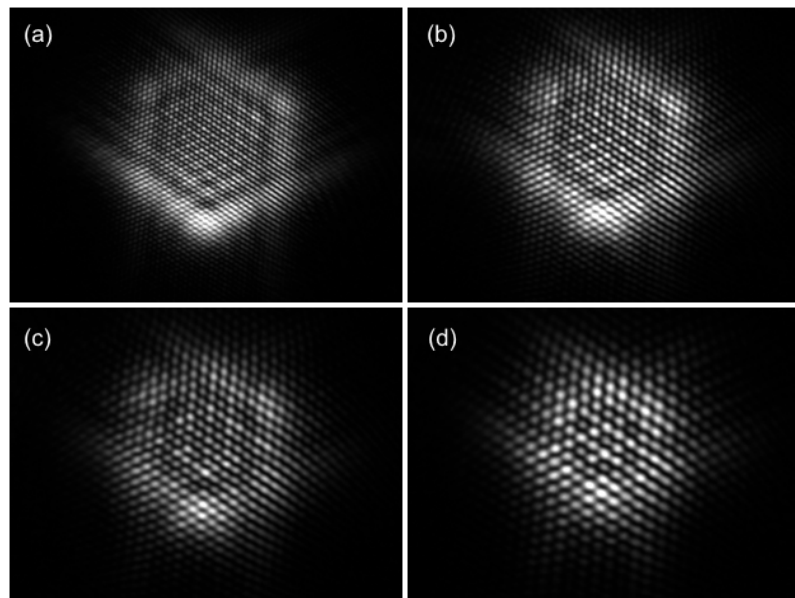


FIGURE 3.15 Images of the beam intensity scanned in air for periodicity (a) 0.16 mm, (b) 0.24 mm, (c) 0.32 mm and (d) 0.40 mm.



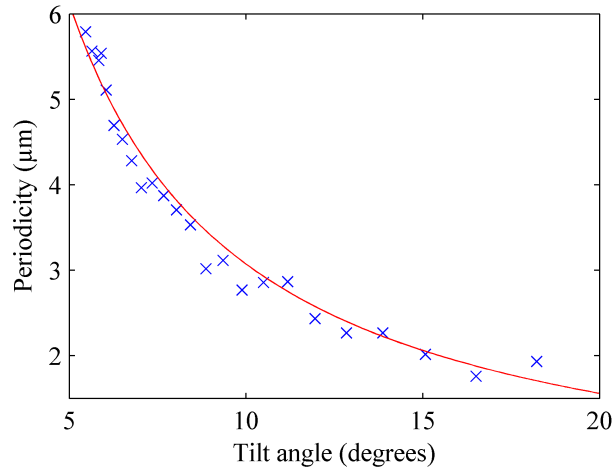


FIGURE 3.16 Experimentally measured periodicity of the interference pattern at the sample position as a function of the tilt angle at the machining region. Red line corresponds to the analytical expression.

As shown in Fig. 3.15, the interference pattern was imaged for different tilt angles, adapting in each case the pulse energy through the Pockels cell voltage and optical densities not to saturate the CCD camera. From the recorded beam images and the angle introduced at the SLM in each case, we retrieved experimentally the relation between the tilt angle in the machining zone and the period of the interference pattern as shown in Fig.3.16, and consequently it allowed us to select the desired period of the interference pattern at the sample position by implementing the corresponding tilt angle at the SLM. Experimental results were in good agreement with the analytical values determined by Eq.3.7.

Finally, we determined for our experiments an optimum tilt angle at the sample position of  $\gamma = 9^\circ$  which leads to a pattern periodicity of  $3.4 \mu\text{m} \pm 0.2 \mu\text{m}$  at the sample position.

### 3.5/ QUANTITATIVE BEAM CHARACTERIZATION

In our experiments, precise control the laser patterning of graphene is based on the accurate characterization of the fluence distribution of the beam along its propagation. The beam characterization system comprises a 4f-system and a CCD camera. We perform a characterization beam procedure consisting in recording the beam image on a CCD camera and retrieving the fluence map using the pulse energy and the camera pixel size. The 4f-system consist of a microscope objective with  $f_1 = 3.6 \text{ mm}$  and a monuted lens with  $f_2 = 200 \text{ mm}$ . The microscope objective was mounted on a 5-axis translational stage wich has micrometric precision. The real pixel size of the CCD camera is  $4.65 \mu\text{m}/\text{pixel}$ , however, to study the images recorded on the camera we have to take into account the 4f-system. As a results, we consider in our calculations a pixel size as follows

$$\text{Pixel size} = \frac{f_1}{f_2} \frac{4.65 \mu\text{m}}{\text{real pixel size}} = 0.0837 \mu\text{m}/\text{pixel} \quad (3.9)$$

By imaging each transversal fluence map of the beam in a CCD camera, we can reconstruct the complete fluence beam profile along its propagation.

There are three conditions to be fulfilled to characterize the images with this procedure :

1. To be in the linear regime of the CCD camera.
2. The whole beam has to be incident onto the CCD camera.
3. The optical components (i.e. optical densities) before the CCD have to stay fixed during the procedure.

For each recorded image, from the number of counts in each pixel, the total sum of pixels of the image, and the pixel size it is possible to retrieve the fluence  $F(x, y)$ ,

$$F(x, y) = \frac{\text{signal}(x, y)}{\text{Total number of counts on the CCD}} \cdot \frac{E_p}{\text{Area pixel}} \quad (3.10)$$

and the pulse energy is the variable parameter that allows us to control the fluence. The procedure had some differences depending on the beam shape we want to characterize.

### 3.5.1/ IMAGING OF THE BESSEL BEAMS

The characterization procedure of the Bessel beam is focused in determining the position corresponding to the peak intensity where the graphene sample will be placed. After recording the complete beam along the propagation axis, we considered the maximum number of counts in the CCD camera recorded at each z-axis scanned position. Fig. 3.17 illustrates an increasing on-axis number of counts when the interference region is reached, followed by a decays due to the spreading of the interference pattern energy over a larger area.

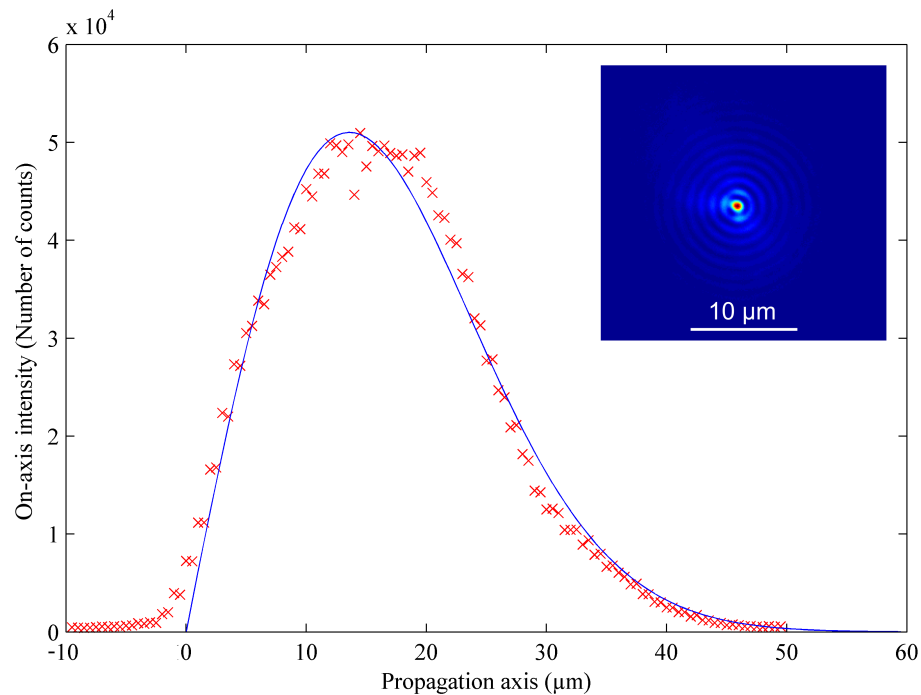


FIGURE 3.17 Comparison between the experimental (red) and theoretical (blue) on axis intensity of the Bessel beam along propagation for a tilt angle of  $\alpha = 26^\circ$ . Inset shows the scanned image of the Bessel beam at the intensity peak plane.

Fig. 3.18(a) shows the experimental longitudinal distribution of the Bessel beam of order zero. Fig. 3.18(b) and 3.18(c) present, respectively, measured and calculated cross section of the beam at a propagation distance corresponding to the peak intensity position.

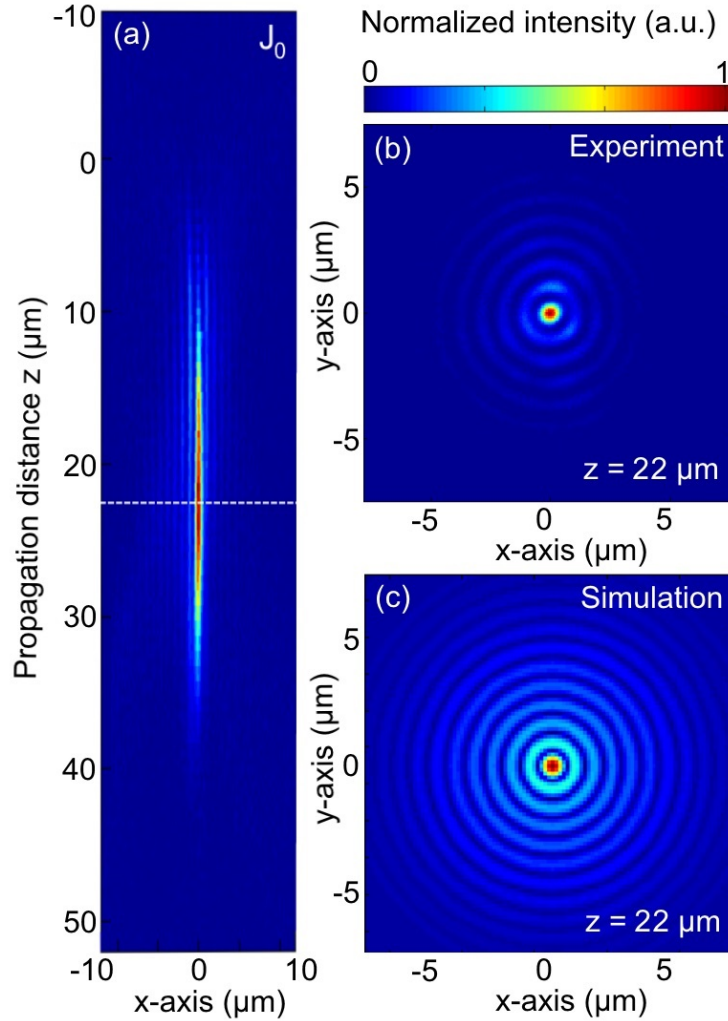


FIGURE 3.18 Experimental scanned Bessel beam in air (a) along propagation axis, (b) transversal profile at the sample, and (c) its corresponding simulation for a tilt angle of  $\alpha = 26^\circ$ .

To investigate the influence of the applied energy gradient in ablation, we used Bessel beams with two different tilt angles :  $26^\circ$  and  $9^\circ$ . The simulated and measured on-axis fluence in both cases are illustrated in Fig.3.19 and Fig.3.20, respectively.

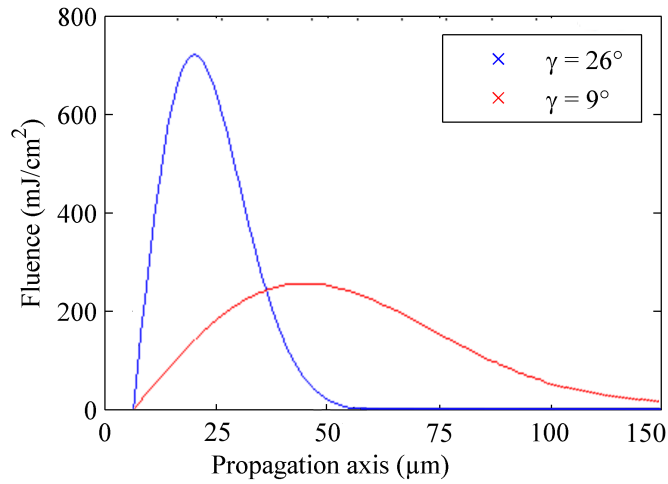


FIGURE 3.19 Theoretical Bessel beam on-axis fluence for pulse energy of 20 nJ and tilt angle of 26°(blue) and 9° (red).

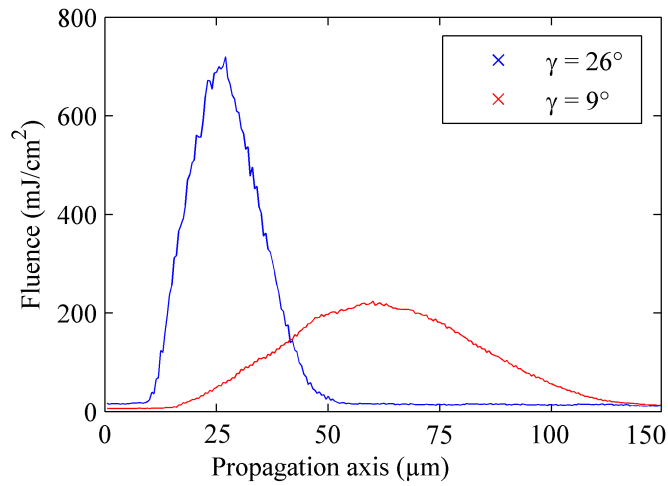


FIGURE 3.20 Experimental Bessel beam on-axis fluence for pulse energy of 20 nJ and tilt angle of 26°(blue) and 9°(red).

### 3.5.2/ HEXAGONAL ARRAY BEAM

In the case of an hexagonal array beam, once the beam is recorded in the CCD camera, the fluence map can be characterized using any of the images of the interference region. From beam parameters and CCD camera characteristics we retrieved the fluence value recorded at any pixel in the camera. For an incident pulse energy of  $E_p = 1\mu J$  we had

$$F_{max} = \frac{\text{Maximum number of counts in 1 pixel}}{\text{Total number of counts on the CCD}} \cdot \frac{E_p}{\text{Area pixel}} = 323\text{mJ/cm}^2 \quad (3.11)$$

Once the intensity at the pixel with the largest number of counts was determined it was possible to scale the complete image as shown in Fig.3.21

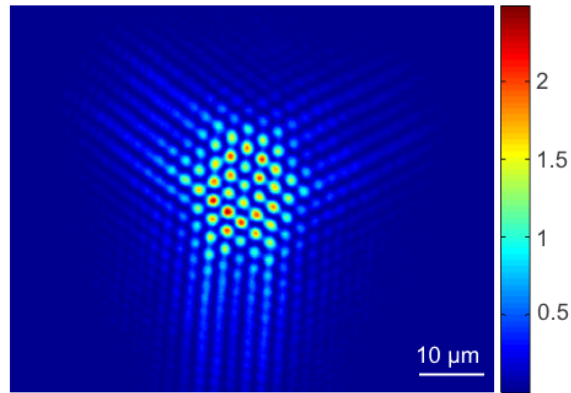


FIGURE 3.21 Intensity profile of the beam scanned in air corresponding to transversal plane number 51 for incident pulse energy  $E_p = 1\mu\text{J}$  for 130 fs pulse. Units are in  $10^{12} \text{ W/cm}^2$ .

### 3.6/ TYPES OF GRAPHENE SAMPLES

In our experiments we used CVD monolayer graphene on two different substrates, glass and quartz, both supplied by Graphene Supermarket. In both cases monolayer graphene film is grown by CVD processing onto copper foil, and then transferred onto glass or quartz.

Thickness and quality of graphene films were controlled by Raman spectroscopy by the company, ensuring graphene coverage of the substrate around 95 % leading to a continuous graphene films with occasional holes and cracks. Since CVD graphene is polycrystalline, it consists of grains with different crystallographic orientation. Supplied graphene films have a transmission above 97 %.

Glass substrate is Corning EAGLE XG AMLCD with a thickness of 0.7 mm and a density of  $2.38 \text{ g/cm}^3$ . Quartz substrate is G.E. 124 fused quartz with a thickness of 1 mm and a density of  $2.21 \text{ g/cm}^3$ .

Since different substrate could have an important role when patterning graphene with ultrafast pulses, the substrate influence is studied in detail in section 4.4.

### 3.7/ SAMPLE POSITIONING

In our experiments, the positioning of the sample with respect to the beam is a critical parameter since our goal is precise patterning of graphene at sub-micron scale. In our experiments we are working with two different types of beams, in each case there will be a set of parameters we want to optimize through the positioning system. In addition, the beam imaging system and the sample patterning system are on different translation stages, so it is required to set a common reference for both in order to compare the beam images with the patterned samples.

### 3.7.1/ HEXAGONAL ARRAY BEAM

For the hexagonal array we want to place the graphene layer at the position where the cross section of the interference area will be the largest, so we can get the largest amount of intensity peaks, which will lead to a large number of ablated holes produced by a single shot. To determine the optimal position next method was developed. The CVD monolayer graphene film on glass was placed at the sample holder with the graphene layer facing the incident beam. Since an accurate perpendicular positioning of the sample respect the beam propagation axis is required to minimize fluctuations from the expected incident intensity, a tilt correction Matlab code was implemented leading to an error in the order of  $1\text{ }\mu\text{m}$  over a distance of 20 mm. We used a camera on top of the sample holder to place the sample at the focus plane of the microscope objective of the beam forming system. By introducing the coordinates at 4 different sample surface points on the focal plane, the code corrected the tilt of the sample respect the beam propagation axis.

Although the microscope objective of the imaging system and the sample holder move along the same direction, they are in different translation stages. Due to this experimental constraint next method was developed to determine which scanned beam image corresponds to the sample position.

Before patterning directly on graphene, an ink mark on graphene was done with a pen. Then several tests were performed onto the ink at very low power, since removing the ink needed much less energy than removing the graphene layer. The ink line thickness was characterized at the optical microscope with a result of  $3\text{ }\mu\text{m} \pm 1\text{ }\mu\text{m}$  which was taken into account in the next measurements.

Initially, the ink layer was not at the interference region, and no ink removal was observed. The sample holder was moved along the translation stage in steps of  $2\text{ }\mu\text{m}$  towards the interference region until first ablated marks appeared on ink indicating the onset of the interference region as shown in Fig.3.22. A single pulse was sent to a clean ink region after each step along the axis. It was easy to visually recognize the correspondence between the marks on ink were easy and the scanned images of the beam in air. Through this scan we could determine the onset of the interference region and link it to the set of scanned images of the beam. The ablation depth, i.e. length of the interference region, was also determined. We concluded that the largest area of the interference pattern appeared  $85\text{ }\mu\text{m}$  after the onset plane.

In order determine the sample position we took into account the contributions from the interference pattern onset position, the ink thickness and the ablation depth displacement. We also determined the error of  $9\text{ }\mu\text{m}$  on the sample positioning.

### 3.7.2/ BESSEL BEAM

For Bessel beams, we want to place the sample at the position corresponding to maximal values of on-axis intensity. A slightly different procedure was developed. In this case, a matrix of shots was done on the ink. Each line of shots consisted in a depth scan, i.e. between two shots the sample was translated along the propagation axis. Pulse energy of each line was progressively reduced respect the previous one. Since the on-axis intensity of a Bessel beam first increases until it reaches the peak and then decreases, using this method we will find at lower pulse energy lines few ablated holes until only there will be one left indicating the exact position of the intensity peak along the propagation axis. In this case also, the relative sample-to-beam position is determined with an error bar of  $\pm 1\text{ }\mu\text{m}$ .

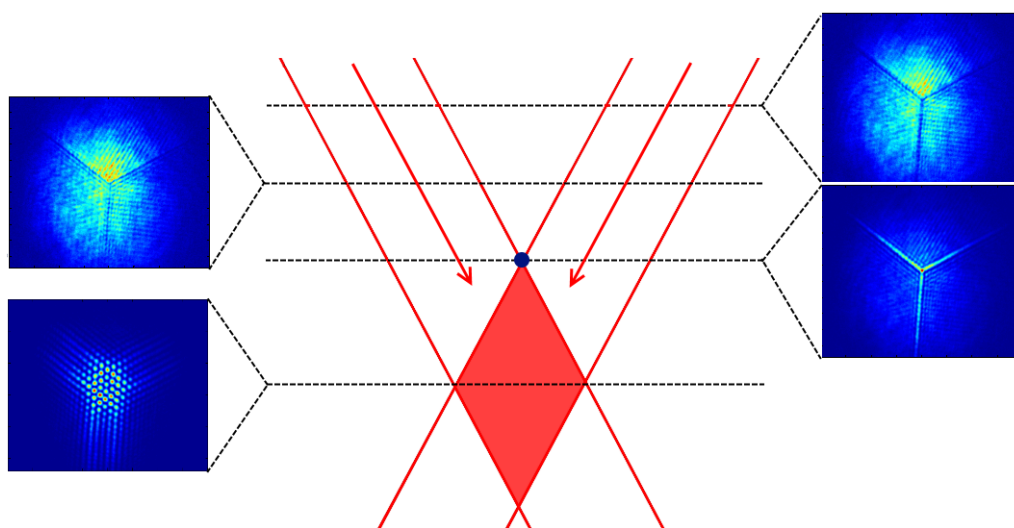


FIGURE 3.22 Transversal intensity beam profile used to determine the onset of the interference region. Blue spot indicates the onset of the interference region (red). Red arrows indicates propagation direction of the different beam sectors.

### 3.8/ SAMPLE CHARACTERIZATION

There are several methods to study graphene samples depending on the properties to characterize. Surface science techniques such as scanning probe microscopies, or other microscopy or diffraction techniques in geometries and/or with energies yielding to superficial penetration of electrons or photons suit for graphene characterization. However, non-surface science methods can be used. Some of these techniques are transmission electron microscopy (TEM) and Raman spectroscopy. Of special interest are the latter technique, which through a resonance scattering process is well suited for the study of a single layer of graphene, and the scanning electron microscopy (SEM), where the graphene surface can be imaged within a nanometer scale resolution.

#### 3.8.1/ OPTICAL MICROSCOPY

As a previous step to the ultrafast laser processing, we produced several samples using the adhesive tape method and characterize them at the optical microscope.

After the aforementioned production process, the sample was placed under the optical microscope and two different procedures were implemented, optical reflection contrast and optical transmission contrast. The linear optical response of exfoliated graphene first received attention for its importance in quantitative identification of graphene layers via optical reflection microscopy on oxidized silicon substrates [1]. Figure 3.23 shows reflection and transmission microscope characterization of an exfoliated graphene sample where regions with different grayscale value indicate different number of graphene layers. Despite the weak graphene absorption, 2.3 % for a single layer, it is still possible to use optical microscopy to visualize large scale damage, i.e. damage diameter larger than 1  $\mu\text{m}$ , for further positioning reference in SEM. This technique is obviously not suitable to



characterize sub-micron damages.

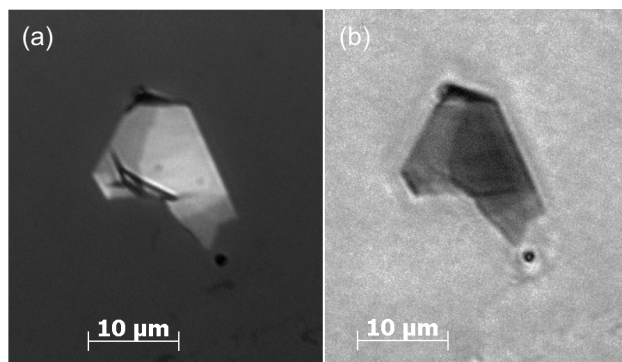


FIGURE 3.23 (a) Reflected and (b) transmission microscope images of adhesive tape exfoliated graphene sample.

### 3.8.2/ SCANNING ELECTRON MICROSCOPY (SEM)

Electrons generated by an electron gun are shaped into a beam through a column composed of electromagnetic lenses. The electron beam is focused onto the sample surface and guided by coils it scans the surface. The beam electron energies can be chosen in a range between few 100 eV to a few keV. Using specific detectors we can determine the existence of secondary electrons, emitted by ionization of the sample's atoms, and back-scattered electrons, which are elastically scattered. Secondary electrons have low energy, they can only escape if they are produced close enough to the impact point of the electron beam onto the surface, which allows high spatial resolution of 1 nm [186]. Since back-reflected electrons are reflected elastically, they have higher energy and they can scatter from rather deep within the sample surface.

SEM is widely used for ex situ characterization of graphene growth. Due to its atomic thickness graphene is usually detected with secondary electrons which probe a topmost fraction of the sample. It allows the study of defects such as wrinkles and provided valuable insight into the damage on graphene caused by ultrafast laser ablation. Secondary electrons also provide information related to the shape of the graphene islands and its size, which was determined to be in the order of tens of micrometers. It also allowed us to determine the grain morphology influence on the ablation probability.

Once the sample was processed by the ultrafast laser, it was mounted rigidly on a holder. Samples need to be electrically conductive to be characterized at the SEM. In our case no treatment of the sample was needed since graphene is electrically conductive, but normally non-conductive samples are sputtered by a conductive material such as gold.

The SEM used to characterize our samples operates with a Everhart-Thornley detector (ETD), which consists in a scintillator inside a Faraday cage inside the specimen chamber of the microscope. A low positive voltage is applied to the Faraday cage to attract low energy secondary electrons. The scintillator has a very high positive voltage to accelerate the incoming electrons to it where they are converted into photons.

During the characterization of our samples two different high voltages were implemented



in the ETD, with values of 1 kV and 5 kV. In the sample images in the case of 1 kV the ablated regions appeared much darker than the background and with nanoholes have sharp edges, meanwhile for a voltage of 5 kV the ablated regions appeared as bright spots as shown in Fig. 3.24. As a results, the first configuration was much better to study both the ablation probability and the damaged/ablated area characteristics and morphology, whereas the second voltage value was convenient only to study the ablation probability at different energies.

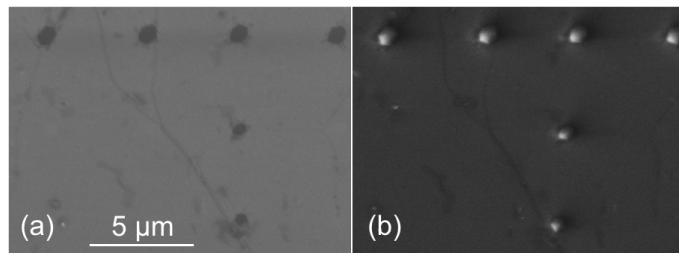


FIGURE 3.24 Comparison of nanoholes in CVD graphene film when ETD voltage is (a) 1 kV and (b) 5 kV.

# SINGLE SHOT ULTRAFAST LASER ABLATION OF CVD MONOLAYER GRAPHENE

When a material is illuminated by a laser beam with a certain fluence (or intensity) distribution, if the local fluence is high enough the material will be removed, typically converted to plasma. Fluence ablation threshold, which is the minimum fluence necessary to remove the material, is a key parameter to control laser patterning.

In this chapter we present the results of the set of experiments we performed in order to determine the possibilities and constraints of single shot ultrafast laser patterning at submicron scale of CVD monolayer graphene. Our first objective was to determine the ablation fluence threshold of this material. We developed two different methods based on comparison between the fluence profile of the beam and the SEM image of the damage which allowed us to characterize the ablation threshold independent of spot size.

Secondly, we performed a statistical study of the ablation process which let us observe a deviation in the threshold model for over-threshold beam diameters below 1  $\mu\text{m}$ . This behavior was explained in terms of the high carrier diffusion coefficient in graphene.

Next we investigated the effect of grain boundaries on graphene ablation at nanoscale. We determined that grain boundaries increase the ablation probability for over-threshold beam diameters below 1  $\mu\text{m}$ .

We explored the ablated area and the ablation probability for CVD monolayer graphene in two different substrates and no significant difference was regarded. We inspected single shot nanopatterning and we observed also certain limitations in the minimal spot size due to graphene folding. We proposed an hypothesis to go further in nanometric control of ablated spot. A magnetic field was applied during the ablation process, which could lead to electronic confinement compensating the high carrier diffusion coefficient.

Finally we studied nanopatterning using higher order Bessel beams which led to different patterned features using the the same beam with different pulse energy.

## 4.1/ DETERMINATION OF THE FLUENCE ABLATION THRESHOLD

Several methods have been developed to investigate the ablation threshold of a material. Regression of crater diameters with fluence averages the fluence threshold over several holes [187]. Recently, the ablation threshold has been retrieved from the comparison between the beam profile and the damage observed in situ by optical microscopy [188].

In back-geometry irradiation, it has been demonstrated reproducible submicron ablation controlling the crater diameter as a function of the focal plane relative to the surface [189]. This approach is, however, inapplicable for craters with sub- $\mu\text{m}$  dimensions, and the relative magnification between beam and damage is a potential source of flaw for circularly symmetric damages. This is why we developed a novel approach using non-diffractive beams with complex intensity distribution.

#### 4.1.1/ EXPERIMENTAL PROCEDURE

We used an amplified Ti:Sapphire laser system delivering 130 fs pulses at 800 nm. Scheme of the experimental setup is shown in Fig. 3.1. The laser operates at kHz repetition rates and pulse-picking is implemented to operate in single-shot regime.

Since it has been largely reported that a material does not have the same ablation threshold for different pulse durations [190], we first characterized the pulse duration. Then, in order to determine the fluence ablation threshold we developed a two steps method based on :

1. Single shot illumination of the sample with a well-characterized complex beam pattern
2. Imaging of the damages by Scanning Electron Microscopy (SEM)

The beam pattern was obtained by multiple interference generating an hexagonal array beam, which defined approximately 40 intensity spots with different sizes and peak intensities. These produced, in single shot, a set of craters with diameters ranging between 0.7 to 2.5  $\mu\text{m}$ . This approach allowed us to directly explore with better confidence the relative ablation threshold and probability of ablation depending on the size, without the ambiguity on pulse energy fluctuations or sample-to-focus critical positioning issue [189]. We used an interference pattern which defines lobes that are almost non-diffracting, which also removed the latter constraint on positioning [191]. In addition, during the fitting procedure, the ambiguity on the relative magnification between beam and sample images was dropped out since the distance between the craters was fixed by the distance between the intensity spots.

Since we were using a complex interference beam pattern, first we developed an accurate alignment method to have the precise projection of the pattern generated after the SLM at the sample position with the desired magnification as shown in Fig.3.14.

First step was to center the incident Gaussian pulse at the SLM screen, then the beam was precisely aligned parallel to the displacement direction of the translation stage of the sample. The pulse energy was characterized at the sample position using a power meter. Next we recorded the hexagonal array beam along propagation in the CCD camera. After characterizing the beam profile at the sample position, we proceeded to pattern the sample.

The sample was placed at the position corresponding to the largest area of the interference pattern. Complete patterning process was done at the same ablation depth. After a single shot was sent, the sample holder moved laterally to a clean area and the procedure started again. We performed 3 sets of ablations at pulse durations of 130 fs, 1 ps, and 3 ps, where we varied the pulse energy from 1  $\mu\text{J}$  to 2  $\mu\text{J}$  and repeated the experiment 5 times in identical conditions. After laser processing, the sample was characterized by SEM, as shown in Figure 4.1.

Error in fluence was determined investigating the scanned images in the 9  $\mu\text{m}$  positioning error range and we concluded that, for an incident pulse energy  $E_p = 1 \mu\text{J}$ , the peak

fluence at the sample position was

$$F_{max} = (323 \pm 16) \text{ mJ/cm}^2 \quad (4.1)$$

With this approach, we have determined the ablation threshold of CVD graphene under ultrafast laser pulse irradiation and investigated the evolution of the ablation probability versus the size of the damage [192].

#### 4.1.2/ EXPERIMENTAL RESULTS

The ablation fluence threshold of CVD graphene was determined by comparing the beam fluence distribution and the SEM image of the ablated sample. We note that the images of CVD graphene have a high dynamical range, so that it is possible to discriminate between ablated areas, laser damaged areas, and un-modified areas [193]. In Figure 4.1 (a), we show, as an example, the image of the ablated sample and beam fluence distribution for one of our data points. After scaling and alignment of SEM and beam images, we implemented two different numerical methods to determine the fluence threshold for ablation.

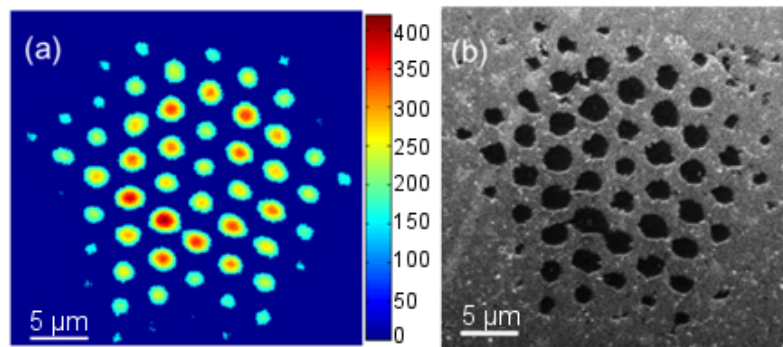


FIGURE 4.1 Comparison of fluence distribution over threshold (a) with the SEM image of the damage (b) for a given intensity distribution, pulse duration (130 fs), and input pulse energy (1.3  $\mu\text{J}$ ).

##### 4.1.2.1/ CORRELATION METHOD

In the first method, we numerically evaluated the correspondence between ablated sample areas and beyond-threshold beam areas. Identically, we evaluated the correspondence between non-ablated areas and below-threshold beam areas. An increasing fluence threshold was applied on the fluence map of the beam scanned in air and after each fluence threshold step it was compared to the SEM image of the ablated sample to retrieve the correlation between both images as shown in Fig. 4.2. The correlation was calculated as the normalized sum of the logical equalities (XNOR function) pixel per pixel over the whole image area. The matching percentage varying as a function of the fluence threshold value is shown for one pulse energy in Figure 4.3. Since the image totals a large area where no ablation occurs where the beam fluence is negligible, the correlation percentage is naturally high (over 98%). The maximum of the correlation curve is still very well defined and provides the value of the threshold. Figure 4.4 shows the residues of the

correspondence at the ablation threshold : the green part shows the matching areas ; red areas are the points where ablation was expected from the threshold and did not occur meanwhile blue areas are the points where no ablation was expected from the threshold but ablation occurred.

Since we focus on ablation, the areas where graphene was damaged but not removed was counted as unmodified in this procedure.

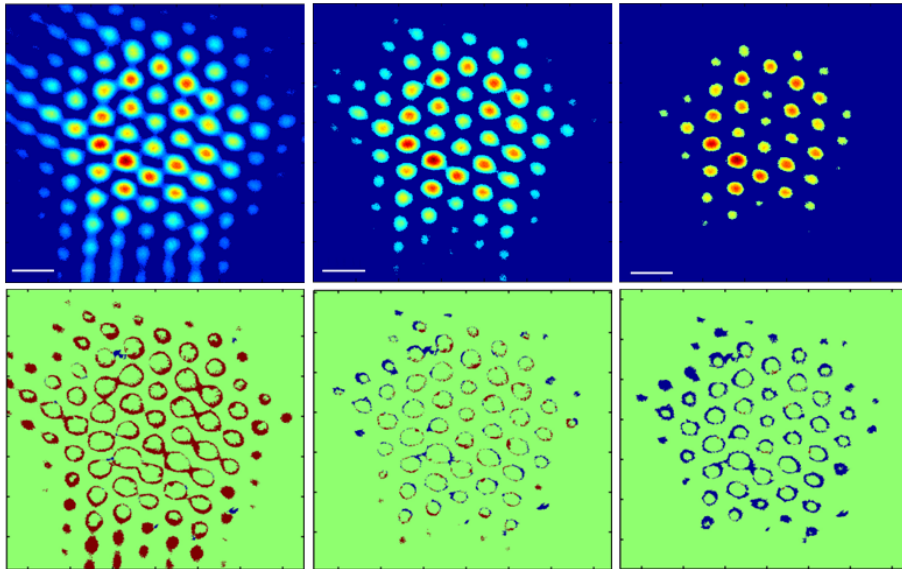


FIGURE 4.2 Beam image (top) applying an increasing fluence threshold from left to right, and the corresponding correlation map between the over-threshold map and the SEM ablated sample (bottom). In the correlation map, green color indicates matching between the fluence map above the threshold and the image of the ablated sample. Red and blue colors indicate mismatch corresponding to a lower and higher threshold values, respectively. The scale bar indicates  $5 \mu\text{m}$ .

In Figure 4.6, we report, in red, the values of the ablation threshold obtained with the procedure described above and that was averaged over 25 images for each pulse duration (i.e., 5 different input pulse energies between  $1.00 \mu\text{J}$  and  $2.00 \mu\text{J}$ , and 5 repetitions for each energy). This effectively provides an average of over  $\sim 1250$  ablated craters. The error bar takes into account the deviation between the images, the errors originating from positioning and energy characterization, and the resolution of the peak of the correlation curve.

This measurement was repeated for different pulse durations (130 fs, 1 ps, 3 ps), and we obtained the ablation fluence threshold of  $139 \pm 7 \text{ mJ/cm}^2$  for 130 fs pulse duration,  $166 \pm 9 \text{ mJ/cm}^2$  for 1 ps and  $190 \pm 9 \text{ mJ/cm}^2$  for 3 ps. These results are in good agreement with previous results [196, 193, 194] ranging between  $100 - 210 \text{ mJ/cm}^2$ , reported on single-shot ablation threshold of CVD graphene samples for similar pulse durations but on wider diameters. A similar correlation procedure has been used by another group to characterize multishot processing of stripes in graphene[195].

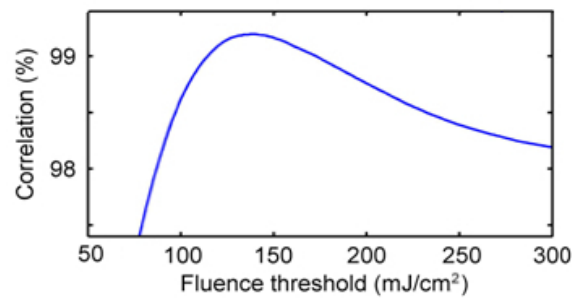


FIGURE 4.3 Correlation between the processed sample image and the scanned beam image applying different fluence thresholds, for a given pulse duration (130 fs) and input pulse energy ( $1.3 \mu\text{J}$ ).

Importantly, our technique allowed for investigating the influence between spots. When the input pulse energy was increased, the areas where the fluence threshold was reached get larger and larger, while the distance between neighboring areas obviously reduced. Within our experimental data, the boundaries between independent spots varied from  $0.8$  to  $2.5 \mu\text{m}$ . Within this range, the change in ablation threshold fluence was not significant and remained below the error bar.

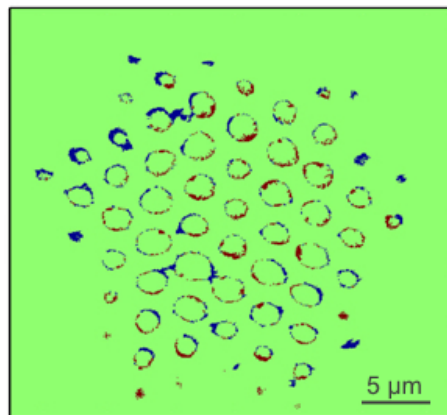


FIGURE 4.4 Image of the spatial distribution of the residues : green color for matching areas, red (resp. blue) for areas where the fluence is higher (resp. lower) than the threshold but ablation did not occur (resp. did occur). This image corresponds to the peak of the correlation in Fig.4.3 for a fluence threshold of  $(139 \pm 7) \text{ mJ/cm}^2$ .

#### 4.1.2.2/ CONTOUR METHOD

For the second method we numerically determined the positions of the contour boundaries between ablated and non-ablated areas on SEM images. The fluence threshold was measured as the average of the fluence value over the contours (again over  $\sim 1250$  ablated craters).

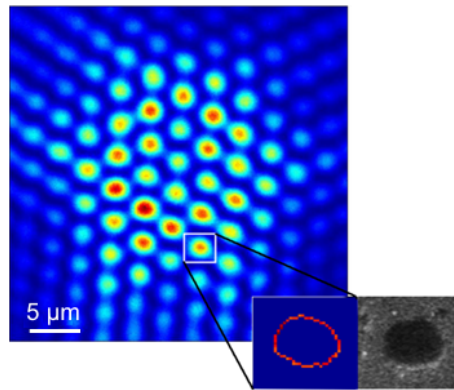


FIGURE 4.5 Direct measurement of the scanned beam intensity at the ablated contour.

The fluence threshold measurement was repeated for different pulse durations (130 fs, 1 ps, 3 ps), and we obtained the ablation fluence threshold of  $149 \pm 6 \text{ mJ/cm}^2$  for 130 fs pulse duration,  $174 \pm 8 \text{ mJ/cm}^2$  for 1 ps and  $191 \pm 9 \text{ mJ/cm}^2$  for 3 ps. The ablation fluence threshold determined using this method, shown in blue in Fig. 4.6, was in good agreement with the results of the previous correlation map method.

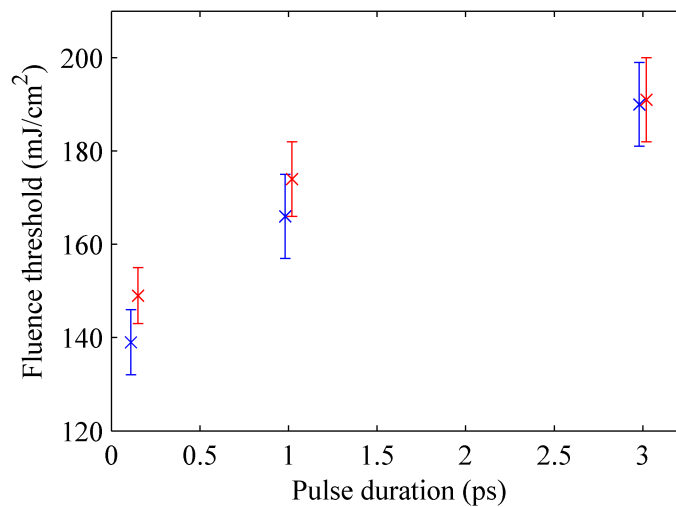


FIGURE 4.6 Comparison between the ablation threshold in monolayer graphene for different pulse duration determined by the best matching over different fluence thresholds technique (red) and by the mean fluence at the ablated contour (blue).

## 4.2/ DEVIATION FROM THRESHOLD MODEL AT SUB-MICRON SCALE

Once the ablation fluence threshold was determined we studied the statistics of ablation depending on the over-threshold beam diameter.

As a result we have determined that below crater dimensions of  $1 \mu\text{m}$ , CVD graphene exhibits a strong deviation from the intensity-threshold model as we will detail in this section.

Indeed, from a closer look at Fig. 4.4, we observed that there was a quantitative difference for the matching between the craters with the largest diameters, located in the central part



of the pattern, and the craters with the smallest diameters, located in the outer part of the pattern. Indeed, while the firsts showed a mismatch of typically less than 15% of the diameter (0.15 to 0.65  $\mu\text{m}$  mismatch for crater diameter ranging between 1.4 and 2.6  $\mu\text{m}$ ), the second have a discrepancy reaching typically 50% (0.25 to 0.65  $\mu\text{m}$  mismatch for crater diameter ranging between 0.7 and 0.9  $\mu\text{m}$ ). Several entirely red disks of  $\sim 400 - 700$  nm in diameter were visible, where ablation was expected from the ablation threshold but did not occur.

To quantitatively characterize this behavior, we tracked the same intensity lobes in the beam over 5 sample processing experiments with identical parameters as shown in Fig. 4.7. For each lobe, we determined the ablation probability. The reference parameter was taken as the *mean diameter* of the lobe over the fluence threshold that we will further refer as the "over-threshold beam diameter" (see Fig.4.8).

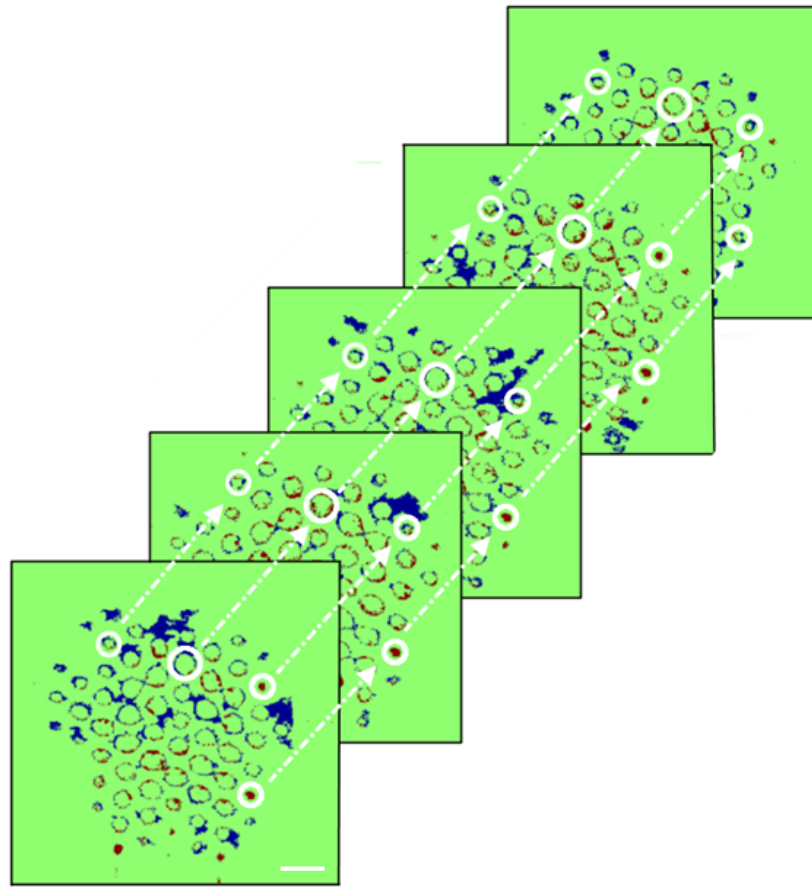


FIGURE 4.7 Tracking same illuminated zones in the correlation map along 5 single shots in identical conditions. The scale bar indicates 5  $\mu\text{m}$ .

This procedure provided, for each pulse energy, a set of  $\sim 40$  values of ablation probability with their respective diameters. In Figure 4.9, we plot as a histogram the evolution of the ablation probability as a function of diameter for input pulse energies from 1  $\mu\text{J}$  to 2  $\mu\text{J}$  and duration 130 fs, 1 ps, and 3 ps. The histogram therefore compiles results where the peak fluence values within the laser spots, range from 150  $\text{mJ}/\text{cm}^2$  to 320  $\text{mJ}/\text{cm}^2$ . We observed that below a diameter of  $\sim 1$   $\mu\text{m}$ , the ablation probability strongly decreased. This behavior was similar for all pulse durations.



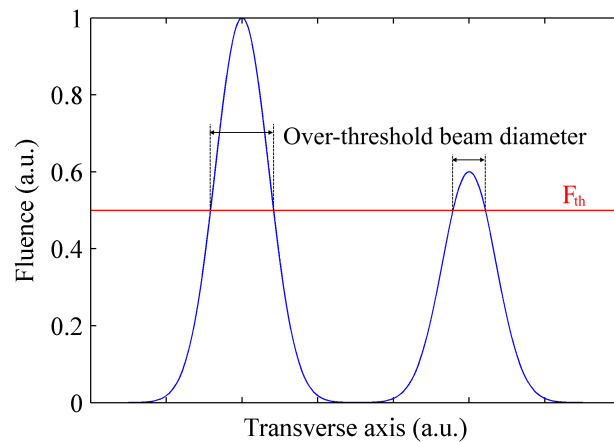


FIGURE 4.8 Over-threshold beam diameter comparison between two pulses with same beam shape but different pulse energy. Red line indicates the ablation fluence threshold.

We note that the structuration of the beam had negligible influence on the variation of the pulse duration over the different lobes [198]. A variation of the ablation probability of bulk fused silica has been reported in other conditions with varying numerical aperture [199]. The decrease of the probability with spot-size decrease was attributed to the reduction of the probability of the ablation volume to meet a structural defect [200]. In our case, the equivalent NA was constant at 0.16, but the difference in amplitude from spot to spot provided an equivalent difference in size of the over-threshold area. Spots with larger over-threshold diameter were obviously more prone to meet defects.

Here we highlight the role of free-electron diffusion. The typical diffusion coefficient for the 2D free electron gas at  $\sim 1$  eV is  $D \sim 5500 \text{ cm}^2/\text{s}$  [201, 202]. In order to explain the observed deviation in ablation probability below a certain over-threshold beam diameter, we performed a simulation of the temporal evolution of the carrier density distribution for different beam diameters.

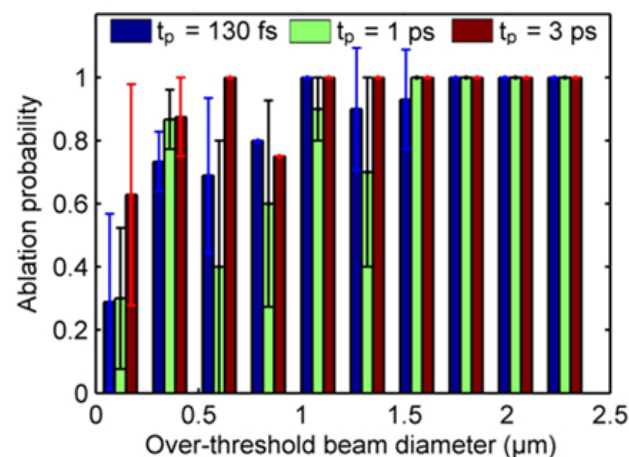


FIGURE 4.9 Probability of ablation in a disk as a function of the beam diameter above the fluence threshold for a pulse duration of 130 fs (blue), 1 ps (green), and 3 ps (red). Error bars show one standard deviation. For the largest diameters, the ablation probability is actually 100% of our tests, resulting in zero-width error bar.

Evolution of the carrier density was described by next equation

$$\begin{aligned}\rho(t) &= \rho_0 e^{-t \cdot D(2\pi\nu)^2} \\ \rho_0 &= \rho_{peak} e^{-\frac{R^2}{w^2}}\end{aligned}\tag{4.2}$$

where we assumed an initial  $\rho_0$  Gaussian shape electron density with waist  $w$ . We introduced a normalized peak density of 1. Within 100 fs, a Gaussian distribution of free-electrons with initial diameter 400 nm at 1/e expands to 1  $\mu\text{m}$  diameter while reducing the peak density by a factor of 6.5. In contrast, if the initial distribution was 2  $\mu\text{m}$  in diameter, it expanded only to 2.2  $\mu\text{m}$  in the same time and the peak electron density dropped only by a factor of 1.2, i.e., 5 times less than in the previous case. This simulation results are shown in Fig. 4.10.

This comparison showed that the high free-carrier diffusion could explain the difference in ablation probability at diameters below 1  $\mu\text{m}$ . Free-electron distributions with a small diameter are highly sensitive to local variations of the diffusion coefficient. In our interpretation, structural defects locally reduce the free-electron mobility, and effectively increase the ablation probability [203]. The influence of inhomogeneities on multi-shot laser processing has also been raised in Ref. [204]. In our view, the discrepancies (blue, red areas) observed in the correlation map of Figure 4.4 could be interpreted as originating from presence/absence of localized defects.

A similar diffusion mechanism involving phonons can also explain our results. However, it would occur on a larger timescale.

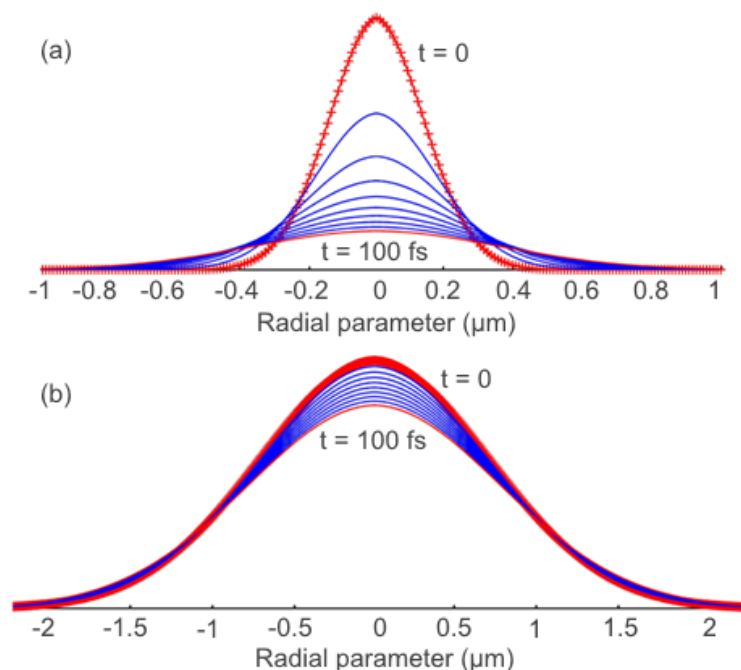


FIGURE 4.10 Evolution of free carrier density within 100 fs for an initial beam diameter of (a) 400 nm and (b) 2  $\mu\text{m}$ . Each blue line corresponds to a time step of 10 fs.

In conclusion, in this section we reported sub-micron patterning of graphene in single shot mode with crater diameters ranging 0.7 - 2.5  $\mu\text{m}$ . We described a decrease of

ablation probability below 1 micron over-threshold beam diameter on CVD monolayer graphene. The same ablation probability behaviour for the three different pulse durations investigated, ranging from 130 fs to 3 ps, suggests that the underlying mechanism is faster than 130 fs or larger than 3 ps. We inferred that high carrier diffusion coefficient in graphene would play a major role in nano-ablation of graphene since it is a major drawback against obtaining high confinement of laser energy deposition necessary for highly localized ablation.

### 4.3/ GRAIN BOUNDARIES INFLUENCE ON SINGLE SHOT NANOPATTERNING

In this section we present the results of our investigation on the impact of polycrystalline structures and grain boundaries on single shot laser patterning of CVD monolayer graphene.

Production of graphene by CVD leads to polycrystalline graphene samples as explained in section 1.4.3.4. The presence of grain boundaries induces changes in graphene properties. Theoretical calculations predict grain boundaries between monocrystallographic regions to act as potential reflective barriers [75].

To our knowledge, no previous studies were done on the impact of polycrystalline structures and grain boundaries on single shot laser patterning of CVD monolayer graphene. SEM image of grain boundaries in a non-patterned CVD graphene sample in Fig. 4.11 shows that any large scale patterning method on CVD graphene will have to deal with grain boundaries, since monocrystalline regions are in the order of tens microns.

Our motivation is to determine if grain boundaries could have an impact on nano-ablation in CVD monolayer graphene on glass substrate.

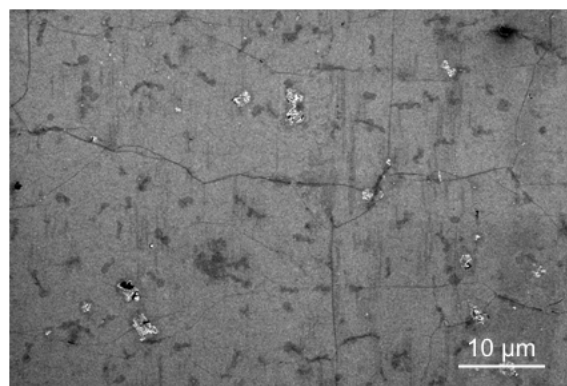


FIGURE 4.11 SEM image of non-patterned CVD monolayer graphene on glass substrate. Dark lines are grain boundaries due to the polycrystalline nature of CVD graphene.

We investigate nano-ablation with highly focused Bessel beams. Those are chosen because using non-diffracting beams allows us to minimize the relative positioning error between the sample and the laser focus.

We have investigated the influence of grain boundaries on the ablation probability.

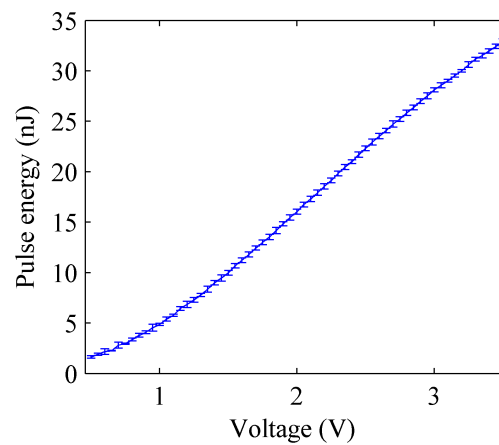


FIGURE 4.12 Pulse energy calibration as a function of the voltage at the Pockels cell. The average error for each pulse energy measurements was  $\pm 0.25$  nJ.

#### 4.3.1/ EXPERIMENTAL PROCEDURE

The experimental setup used in the grain boundaries investigation is close to the setup used before. In this case we used Bessel beam with a tilt angle of  $26^\circ$  as detailed in section 3.4.2. The setup includes spatial Fourier filtering to avoid undesired diffraction orders. By using the method previously reported we characterized the pulse energy in terms of the voltage applied in the Pockels cell by measuring the power at the sample position as shown in Fig. 4.12. Since precise pulse energy characterization was crucial in our experiment 10 measurements were done at each voltage value and an average error of  $\pm 0.25$  nJ was determined for the pulse energy values. Next, we scanned the beam intensity of the zero-th order Bessel beam along its propagation, the fluence map was characterized and the sample position corresponding to the peak fluence was determined. This procedure was detailed in sections 3.5 and 3.7.

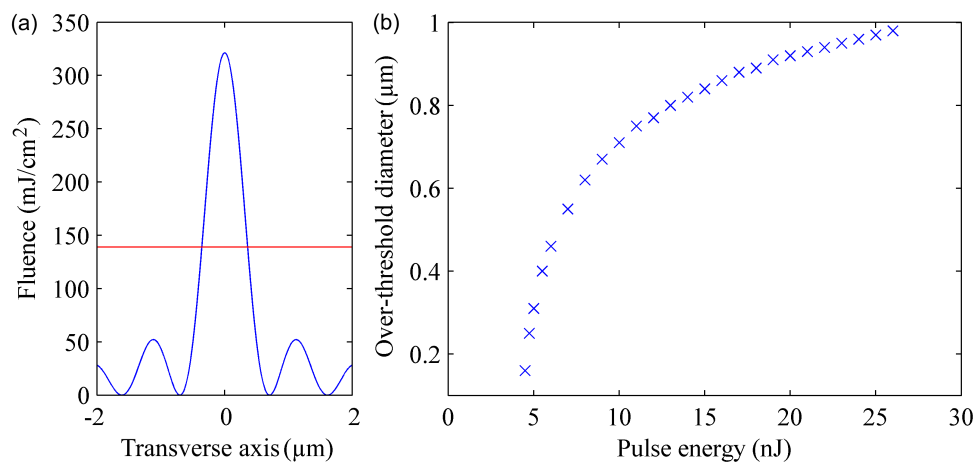


FIGURE 4.13 (a) Analytical transverse fluence profile at the sample position for an incident pulse energy  $E_p = 10$  nJ. Red line indicates graphene ablation fluence threshold of  $139 \text{ mJ/cm}^2$  and the corresponding over-threshold beam diameter is  $0.75 \mu\text{m}$ . (b) Over-threshold beam diameter for pulse duration of 130 fs at different pulse energies.

The total positioning error was  $1.2\ \mu\text{m}$ . Matrices of laser ablated holes were done with pulse energies in the range from 5 nJ to 20 nJ. The characterization images of the Bessel beam showed that all pulses were above the ablation fluence threshold, in which case we should expect to produce ablation in all the illuminated zones. Precise characterization of the transverse intensity of the Bessel beam allowed us to control the over-threshold diameter of the Bessel beam by controlling the pulse energy as shown in Fig. 4.13. For each pulse energy a matrix of 400 single shot illumination sites was investigated. After laser processing, the samples were characterized by SEM.

#### 4.3.2/ EXPERIMENTAL RESULTS

Fig.4.14 illustrates two matrices of illuminated spots. In (a) a pulse energy of 20.0 nJ was used and all illuminated spots were ablated independent of grain boundary presence, whereas (b) shows a strong correlation between the ablated spots and the presence of grain boundaries in the vicinity of the illuminated site. We defined the vicinity as a circular region of  $0.5\ \mu\text{m}$  radius around the centre of the irradiated region. Graphene regions with no grain boundaries presence are monocrystalline domains, called graphene islands.

We performed a statistical study of the SEM images of the patterned sample, which results are illustrated in Fig. 4.15. As in the previous experience, we determined a decrease in ablation probability when over-threshold beam diameter is below  $1\ \mu\text{m}$ . However, we report two different behaviors depending on the presence or absence of grain boundaries in the vicinity of the illuminated zone.

When the laser illumination takes place on a graphene island, the ablation probability has a step-like behaviour from 100% ablation probability to no ablation for over-threshold beam diameters below  $\sim 1\ \mu\text{m}$ . In the presence of grain boundaries, the ablation probability below  $\sim 1\ \mu\text{m}$  over-threshold beam diameters decreases gradually until it is zero for over-threshold beam diameters below  $\sim 0.6\ \mu\text{m}$ .

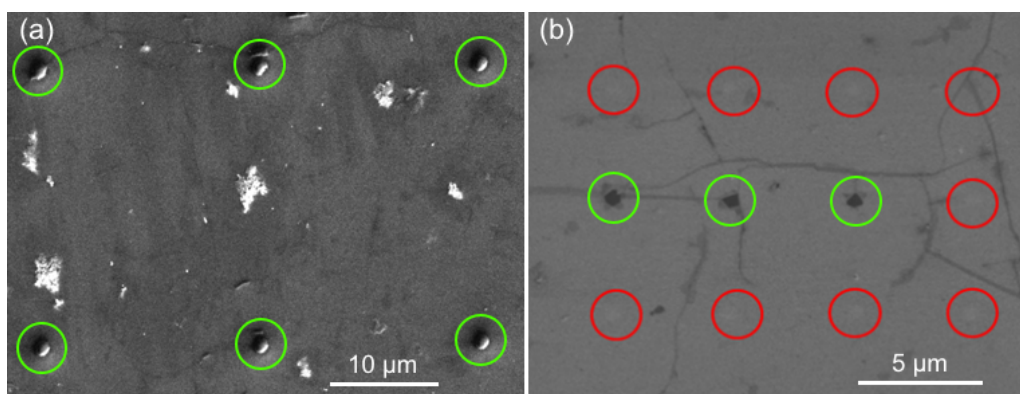


FIGURE 4.14 SEM image of matrix of equidistant laser illuminated spots with zero-th order Bessel beam with pulse energies of (a) 20.0 nJ and (b) 10.0 nJ. Red circles indicates illuminated but non-ablated sites and green circles indicates illuminated and ablated sites. Correlation between ablated holes and grain boundaries is obvious for the lower pulse energy. Difference in grayscale between both images corresponds to different voltage used at the SEM.

Ablation as a consequence of the presence of grain boundaries and not reverse, i.e. grain boundaries generated due to the ablation, was proved by sample inspection at the SEM. Similar density of grain boundaries was observed in patterned and non-patterned regions of the sample.

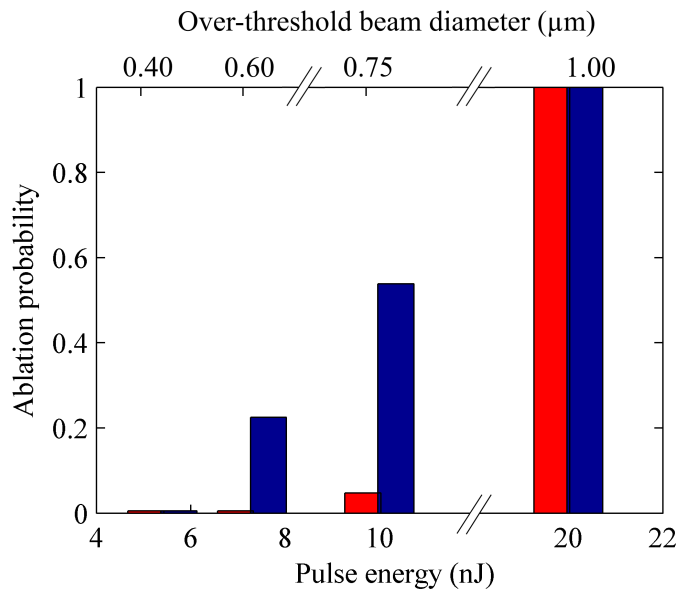


FIGURE 4.15 Ablation probability comparison between illuminated site in a graphene island (red) and in the vicinity of a grain boundary (blue).

In conclusion, we found a preference for grain boundaries as selective ablation sites for small beam diameters as shown in Fig. 4.16.

Our interpretation is the following :

A high reduction of the electron transmission has been determined in grain boundaries due to the misorientation angle between monocrystalline grain domains and the atomic structure at the grain boundaries [81]. The propagation of the free-electrons in the vicinity of a grain boundary acting as a reflecting potential barrier would increase the carrier density, and as a result, the experimentally determined gradual decrease in ablation probability at grain boundaries could be explained by the electronic confinement of the carriers at the grain boundary.

This result is consistent with the behaviour determined in previous section for over-threshold beam diameters below 1  $\mu\text{m}$ . Due to high diffusion coefficient, ablation probability in graphene islands has a step-like decrease to zero for over-threshold beam diameters below 1  $\mu\text{m}$ . However, in the case of laser illumination in the vicinity of grain boundaries, the electronic confinement due to grain boundaries acting as reflecting potential barriers compensates the rapid diffusion of free-carriers and the ablation probability tends to zero more gradually.



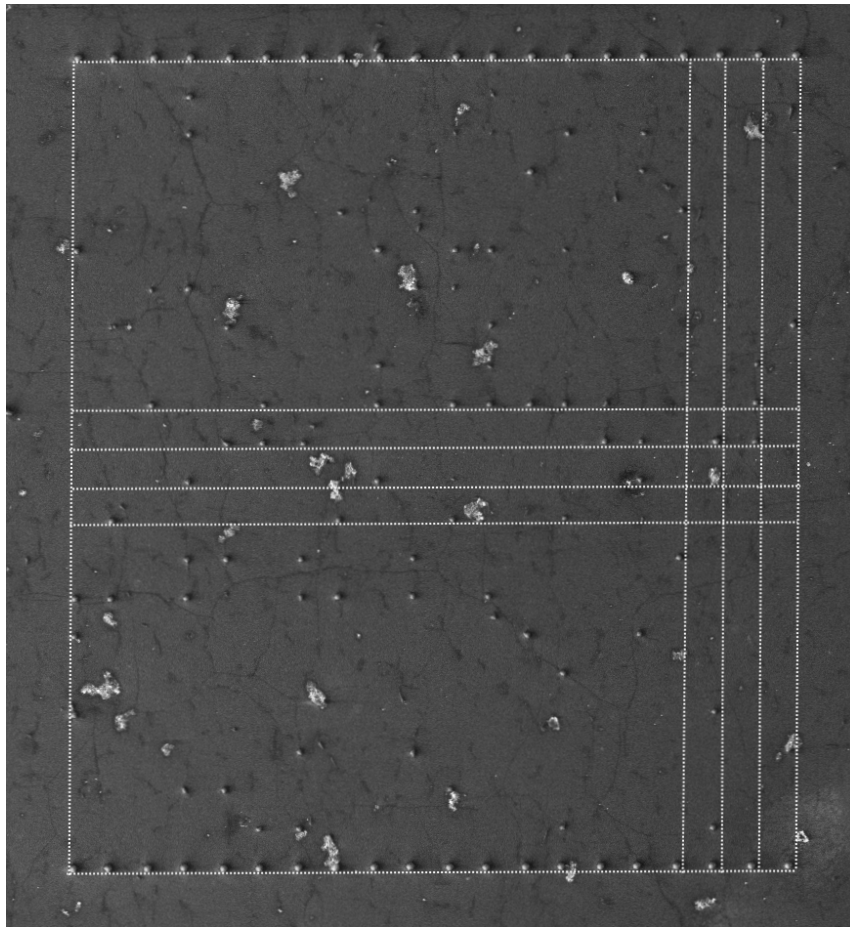


FIGURE 4.16 SEM image of matrix of equidistant 400 laser illuminated spots with pulse energy 10.0 nJ. Crossing white lines are the illuminated ablation sites. Top and bottom lines of ablated holes are reference lines patterned at 20.0 nJ where the ablation probability is 100%. The white colour of the ablated holes is due to the voltage applied at the SEM.

#### 4.4/ INFLUENCE OF SUBSTRATE ON SINGLE SHOT ABLATION OF CVD GRAPHENE

Future potential graphene applications will require patterned graphene on a substrate. In this section we investigate the effect of different substrate on ablation by comparing patterning of CVD monolayer graphene on glass substrate and on quartz substrate. Both samples were patterned using zero-th order Bessel beam with  $\rho_0 = 1.4$  mm corresponding to a tilt angle of  $9^\circ$ . We patterned 15 lines with different pulse energy each line, consisting of 20 illuminated sites, resulting in a total of 300 ablation sites for each different substrate. The results are plotted in Fig. 4.17 and we show the ablation probability as a function of input pulse energy. Laser fluence was close to the ablation threshold of graphene, which is one order of magnitude lower than the threshold for the substrates, avoiding underlying substrate damage. No significant difference was observed in the ablation probability for equal pulse energy, i.e. same over-threshold beam diameter, as shown in Fig. 4.17.

#### 4.4. INFLUENCE OF SUBSTRATE ON SINGLE SHOT ABLATION OF CVD GRAPHENE<sup>85</sup>

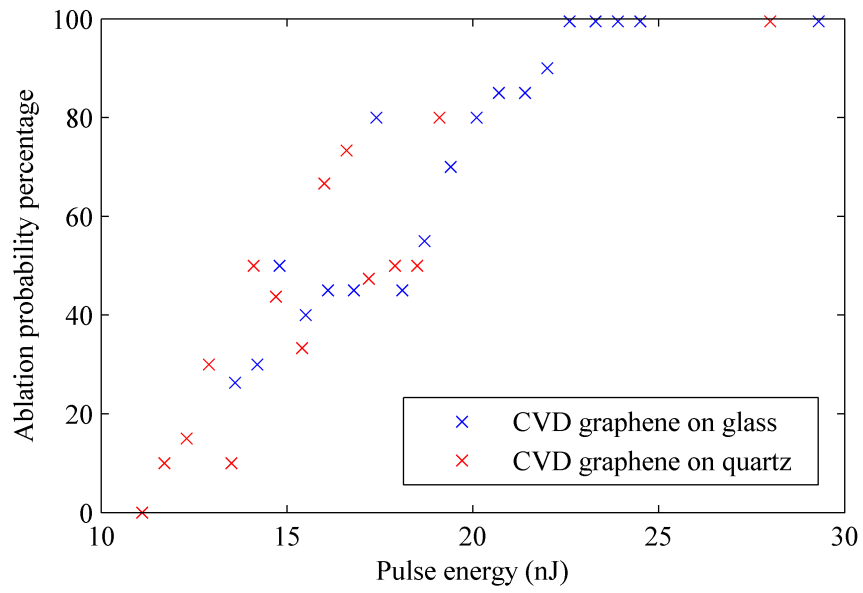


FIGURE 4.17 Ablation probability comparison between CVD monolayer graphene on glass substrate (blue) and on quartz substrate (red) for a pulse duration of 130 fs and different pulse energies.

Fig. 4.18 compares the evolution of the ablated spot area with energy for the two substrates. No significant difference appears

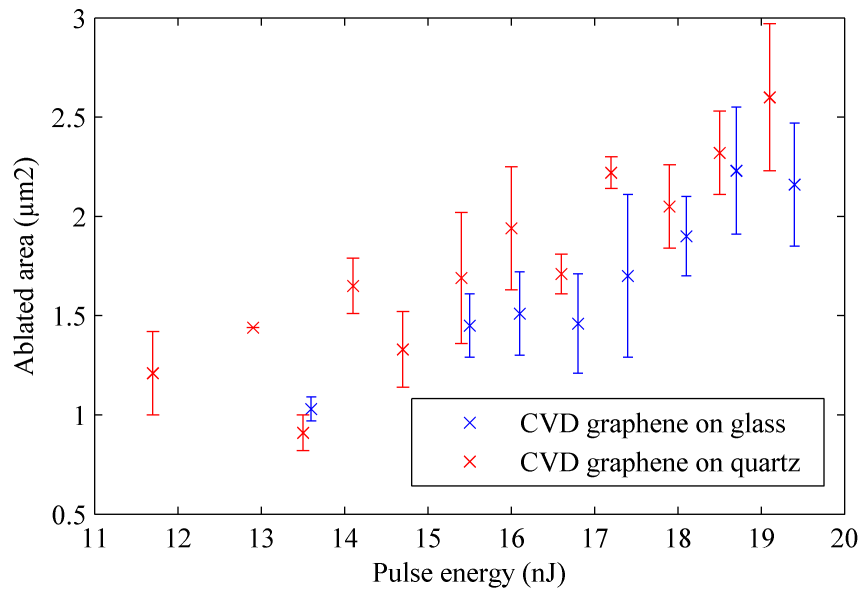


FIGURE 4.18 Ablated area comparison between CVD monolayer graphene on glass substrate (blue) and on quartz substrate (red) for a pulse duration of 130 fs and different pulse energies.

From our experiments we concluded that, in the investigated range of energies, the dielectric substrates have no impact on patterning of graphene, despite the fact their bandgaps are different ( $\sim 4$  eV for glass and  $\sim 6$  eV for quartz substrate).



#### 4.5/ ANALYSIS OF ABLATED SPOT EVOLUTION WITH OVER-THRESHOLD BEAM DIAMETER

In this section we investigate the morphology of the damages observed at SEM under different Bessel beam tilt angle. Bessel beam presents different over-threshold diameter and peak fluence depending on the tilt angle leading to a different fluence distribution onto the sample. We want to determine the effect of the different energy confinement on nano-ablation.

We used the same experimental setup as in previous sections.

A matrix of ablated spots was patterned with different pulse energies. Over-threshold beam diameter was controlled by the pulse energy.

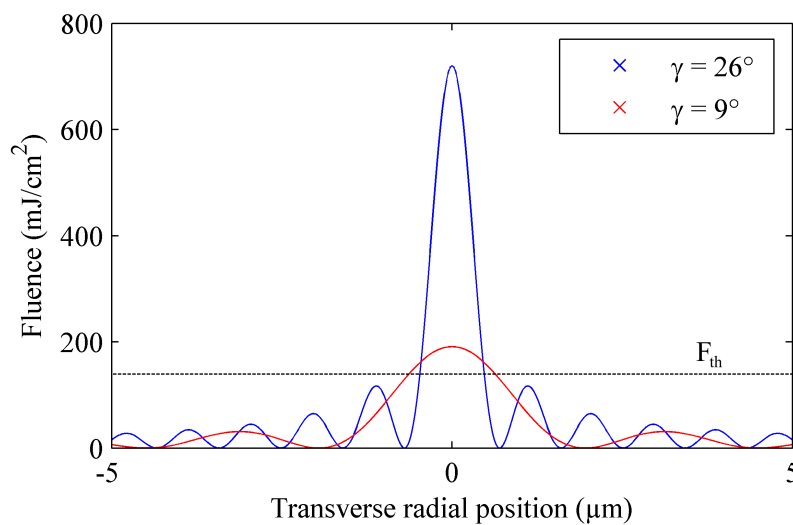


FIGURE 4.19 Analytical fluence distribution of the Bessel beam at the sample position for pulse energy of 20 nJ and tilt angle of 26 ° (blue) and 9° (red). Black dashed lines corresponds to graphene ablation fluence threshold.

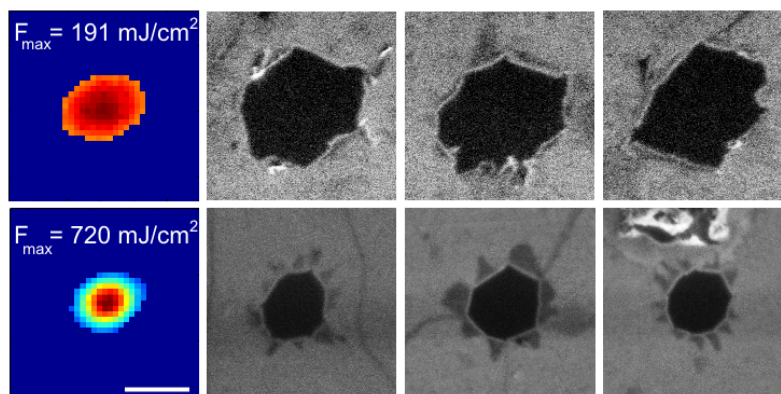


FIGURE 4.20 Experimentally characterized over-threshold fluence beam and SEM images of ablated holes for a pulse energy of 20.0 nJ for tilt angle of (top) 9° and (bottom) 26°. White scale bar corresponds to 1  $\mu\text{m}$ . All images are at the same scale.

The sample was characterized at the SEM. It is apparent on Fig. 4.20 that folding appears on the sides of the ablated hole. This was already observed by Yoo et al [205]. Graphene folding appeared preferentially for the highest focussing conditions. The ablated area and the area of the graphene folded petals were measured for each pulse energy corresponding to a certain over-threshold beam diameter as shown in Fig. 4.21. Statistical study over 20 identical single shots were done per each pulse energy. We found a different behavior for over-threshold beam diameters above and below  $1\text{ }\mu\text{m}$ . Above  $1\text{ }\mu\text{m}$  the ablated area increased rapidly with rising beam diameter (or pulse energy), and below  $1\text{ }\mu\text{m}$ , the ablated area remained almost constants in the range investigated corresponding to over-threshold beam diameter from approximately  $200\text{ nm}$  to  $1\text{ }\mu\text{m}$ .

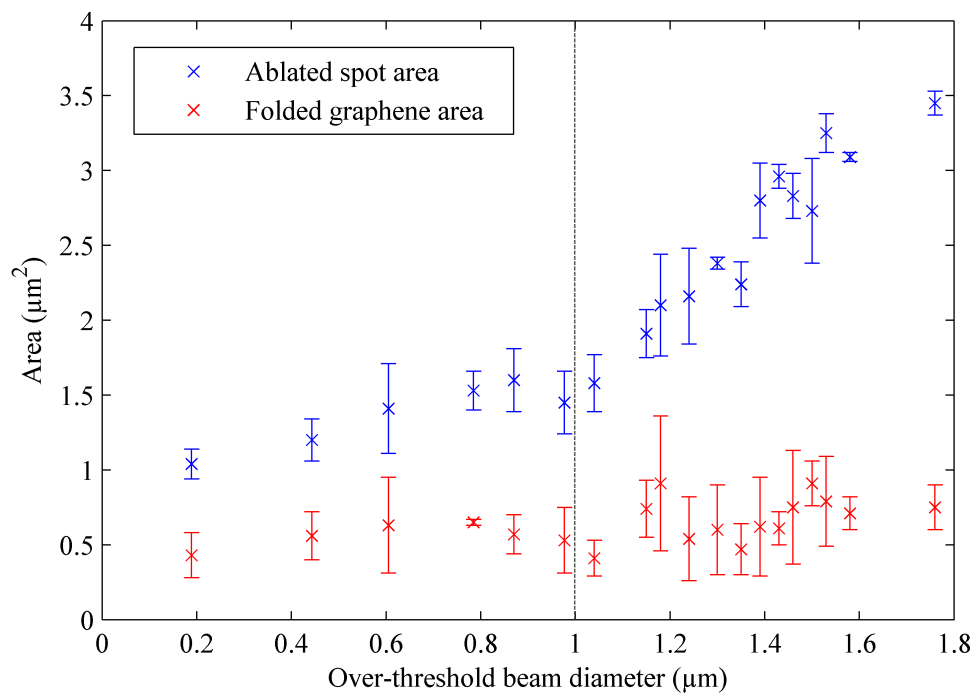


FIGURE 4.21 Measured areas of ablated spots (blue) and folded graphene petals (red) for a tilt angle of  $9^\circ$ . Each value corresponds to the average of 3 measured spots for each over-threshold diameter.

It is interesting to remark that in the complete range of over-threshold beam diameters investigated the area of the folded graphene remained almost constant. Previous investigations by other groups stated that although ablated area increased as pulse energy rises, the number of folded petals remains constant [205].

We inferred this behavior was due to relative size of the folded graphene respect the ablated spot. In fact, in what is commonly defined as ablated spot there are two different contributions, a truly ablated region where there is a material removal process and a graphene void region corresponding to graphene petals which just lifted up and folded.

We investigated the ablation and formation of graphene folded petals using a Bessel beam with a tilt angle of  $9^\circ$ , corresponding to a low energy gradient. As illustrated in Fig. 4.21, when the truly ablated region was larger than the area of folded graphene, the total area of the ablated spot (including both contributions) had a fast linear decrease with de-

creasing over-threshold diameter. However, when the truly ablated region was in the order of the folded graphene area, the total area of the spot remained approximately constant. We performed the same experience using Bessel beam with a tilt angle of  $26^\circ$ , i.e. with a higher energy gradient. Although only three pulse energies were investigated in this configuration, Fig. 4.22 shows clearly a different behaviour depending on the energy gradient even if the over-threshold beam diameter is the same. For a tilt angle of  $9^\circ$  the spot area is larger than the folded graphene area, meaning that there are two differentiated regions, one that was ablated and a part of the graphene sheet folded into petals. In the case of a tilt angle of  $26^\circ$ , the area of spot is equal to the area of the ablated petals, i.e. there was no *real* ablation, the mechanism leading to folded graphene formation completely overcomes the ablation process.

Further investigation is required since the mechanism of folded graphene formation is most probably a complex combination of laser-graphene, graphene-substrate interactions and mechanical stiffness. It has been demonstrated no formation of folded graphene structures in laser patterning of suspended graphene, which shows that folded graphene structures formation is critically related to the interaction between the graphene layer and the underlying substrate [205].

In addition, folded graphene limiting the minimum ablated spot could be a main constraint for single shot nanopatterning of graphene.

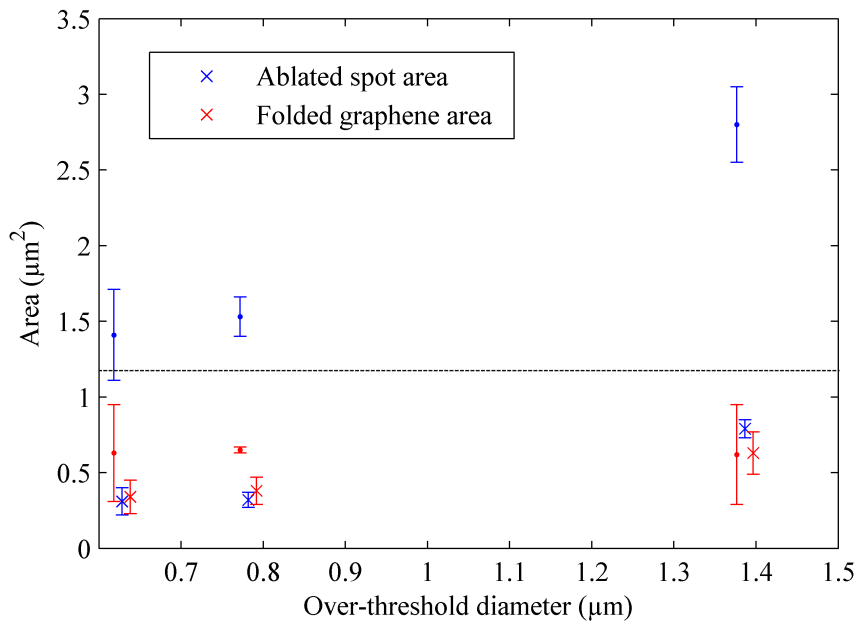


FIGURE 4.22 Measured areas of ablated spots (blue) and folded graphene petals (red) for a tilt angle of  $9^\circ$  (dots) and  $26^\circ$  (crosses). Dashed line corresponds to a  $1 \mu\text{m}$  diameter.

#### 4.6/ EXTERNAL MAGNETIC FIELD EFFECT ON MONOLAYER GRAPHENE LASER PATTERNING

From the previously reported results we inferred the deviation in ablation behaviour below a certain over-threshold diameter is due to the high diffusion coefficient of electrons in graphene. In order to compensate this rapid diffusion we set the next hypothesis.

If the ablation of graphene at nanoscale is carried out in the presence of a magnetic

field, there could be an electronic confinement effect compensating the rapid diffusion and there would be a higher ablation probability for over-threshold diameters below  $1\ \mu\text{m}$ . We also investigate the possibility of patterning smaller diameter holes in the presence of a magnetic field due the above mentioned effect. The radius of curvature of the trajectory of a charged particle in a magnetic field, also called gyroradius, is defined by

$$r_g = \frac{mv}{|q|B} \quad (4.3)$$

where  $m$  is the particle mass,  $v$  is the component velocity perpendicular to the magnetic field direction,  $q$  is the electric charge of the particle and  $B$  is the magnetic field. Within our experimental parameters, for an electron with an energy of typically 1 eV in a magnetic field of 1 T, the non-relativistic gyroradius is  $\sim 3\ \mu\text{m}$ , which is in the order of the diameter of the ablated spots we are investigating.

#### 4.6.1/ MAGNET DESCRIPTION

In order to detect the response on the ablation process due to potential electronic confinement in presence of magnetic field, the strongest the field the easily detectable the effects would be.

There were two different magnet configurations available for our experiments : ring magnets and rod magnets.

The magnetic fields of a ring and rod magnets follow next equations,

$$B_{ring} = \frac{B_r}{2} \left[ \frac{D+z}{\sqrt{R_a^2 + (D+z)^2}} - \frac{z}{\sqrt{R_a^2 + z^2}} - \left( \frac{D+z}{\sqrt{R_i^2 + (D+z)^2}} - \frac{z}{\sqrt{R_i^2 + z^2}} \right) \right] \quad (4.4)$$

$$B_{rod} = \frac{B_r}{2} \left( \frac{D+z}{\sqrt{R^2 + (D+z)^2}} - \frac{z}{\sqrt{R^2 + z^2}} \right) \quad (4.5)$$

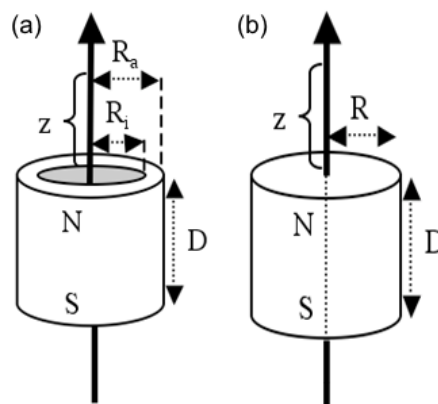


FIGURE 4.23 (a) Ring magnet and (b) rod magnet configuration.

Theoretical calculations for our available magnets in Figure 4.24 showed clearly the most convenient configuration was the rod magnet, which had a magnetic field of  $\sim 0.4\ \text{T}$  at a distance of 0.8 mm from the magnet surface, meanwhile in the case of ring magnet, at same distance, the field was only 0.08 T. Neodymium Iron Boron rod magnet from Supermagnet company was used. We consider 0.8 mm since it was the closest magnet

position to the graphene layer achievable in our experimental setup. CVD monolayer graphene on glass sample thickness was  $0.7\ \mu\text{m}$  and we needed an extra  $0.1\ \mu\text{m}$  to be sure the rod magnet did not collide with the sample.

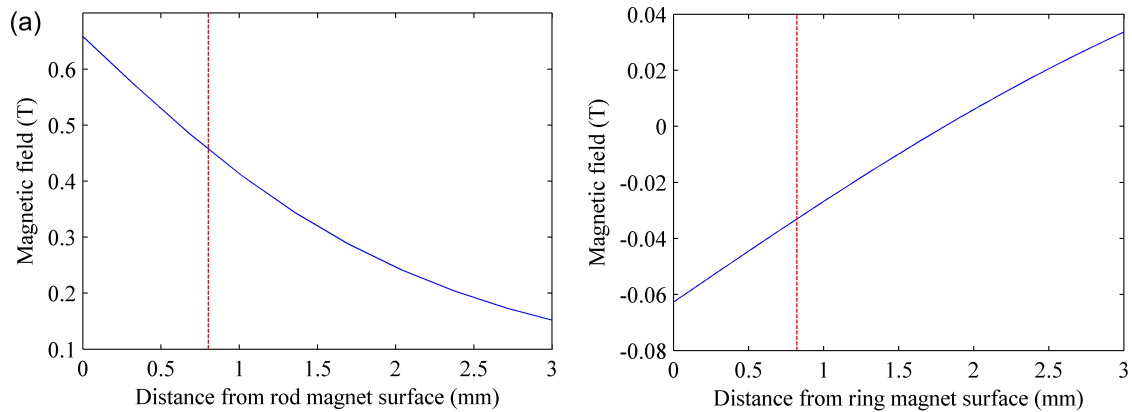


FIGURE 4.24 (a) Rod and (b) ring magnetic field as a function of the distance from the magnet surface. Red dashed line indicates the graphene layer distance to the magnet surface.

#### 4.6.2/ EXPERIMENTAL PROCEDURE

We used similar experimental setup as in previous sections.

Beam fluence distribution along propagation was scanned in air in steps of  $0.5\ \mu\text{m}$  and the transversal plane with the maximum on-axis intensity was selected to place the sample. Once the position of the sample holder corresponding to the peak intensity of the Bessel beam along propagation was known, we proceed to determine the magnet position.

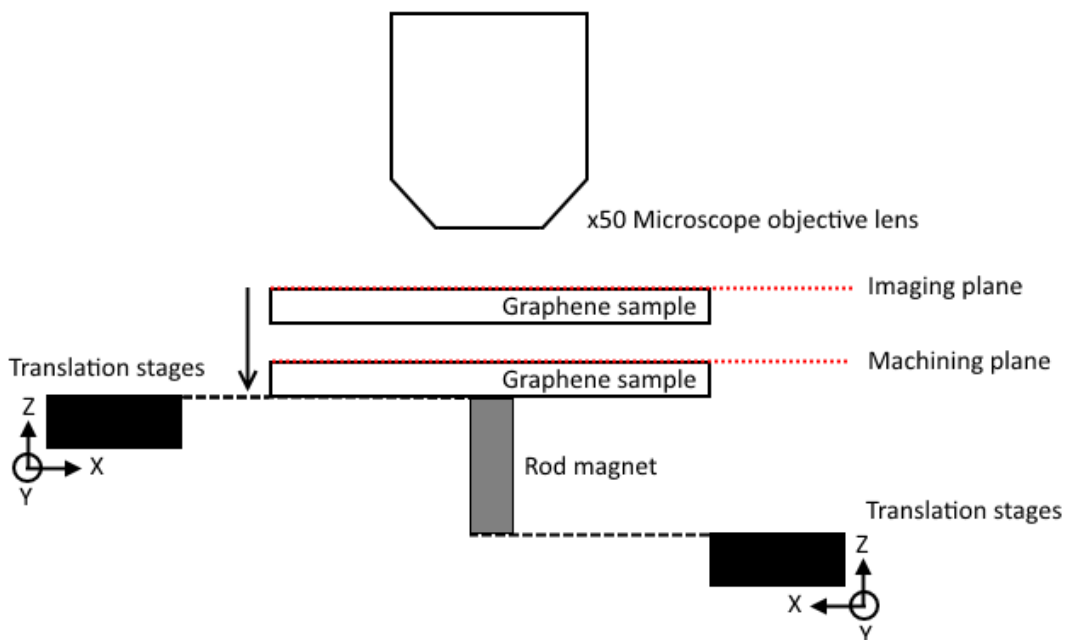


FIGURE 4.25 Scheme of the sample and magnet positioning system.

We used the top camera to observe the surface of the magnet and considering the difference between imaging plane and machining plane as illustrated in Fig. 4.25, we place the magnet surface at  $800\ \mu\text{m} \pm 2\ \mu\text{m}$  from the graphene layer.

After determining the magnet position, the monolayer graphene sample was placed in the sample holder attached to its own translation stage. Then, the sample surface was moved to the machining plane position and the graphene layer was patterned without presence of any magnet. Finally the patterning procedure was repeated under same laser beam parameter in the presence of an external magnetic field.

#### 4.6.3/ RESULTS AND CONCLUSIONS

We investigated the variation in ablated spot area and ablation probability in both experimental configurations, with and without magnetic field.

In order to investigate the ablated area, a set of holes were patterned with fixed pulse duration  $t_p = 130\ \text{fs}$  in a pulse energy range from 32 nJ up to 650 nJ, well above the ablation threshold.

A statistical study of the SEM images of the ablated sample determined no appreciable difference in the ablated area in the presence of a magnetic field as shown in Figs. 4.26 and 4.27, where each area value corresponded to the average of 5 different ablated holes for the same pulse energy. The first figure shows the results for pulse energies above 100 nJ and the second for pulse energies below 100 nJ. Larger errorbars in the latter were due to higher relative error when the ablated area became smaller.

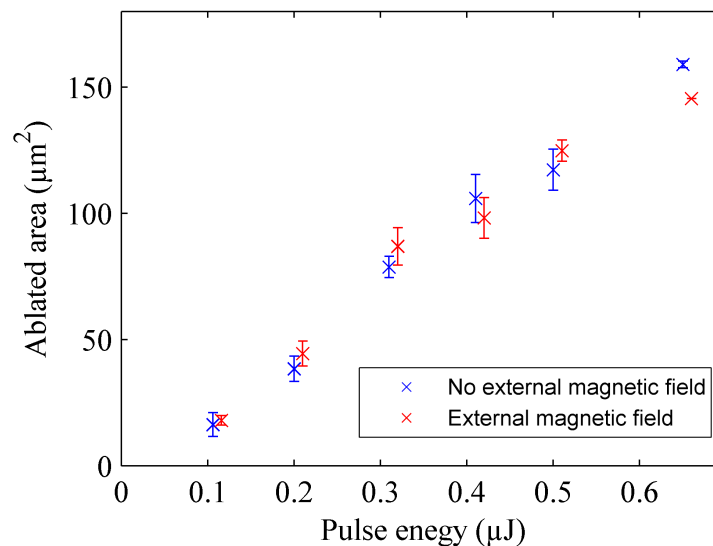


FIGURE 4.26 Comparison between the ablated area with (red) and without (blue) magnetic field presence for different pulse energies in the range from 100 nJ up to 650 nJ.

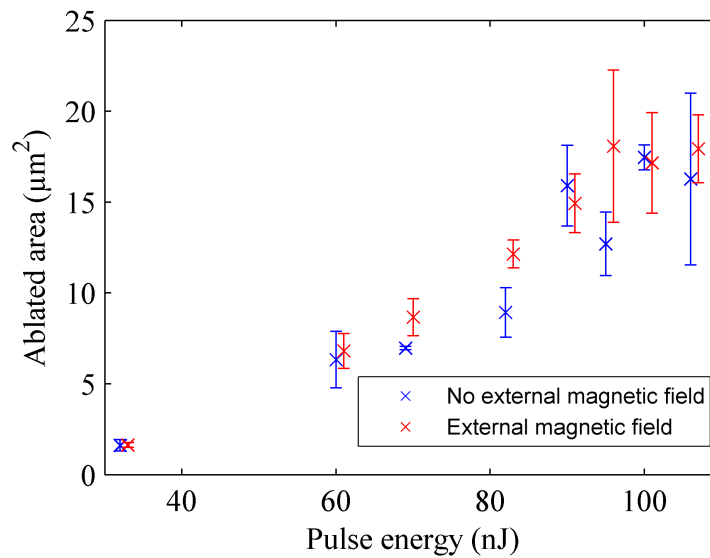


FIGURE 4.27 Comparison between the ablated area with (red) and without (blue) magnetic field presence for different pulse energies in the range from 32 nJ up to 100 nJ.

Next we wanted to investigate the possible effect of a magnetic field on the ablation probability of graphene. A first set of holes with energies between 13 nJ and 35 nJ was patterned with pulse duration of 130 fs and tilt angle of  $9^\circ$ . Each line with constant pulse energy consisted in 10 ablation sites.

It was repeated with same parameters with and without presence of magnetic field. Results are shown in Fig. 4.28. Peak fluence of all pulses were above the ablation threshold.

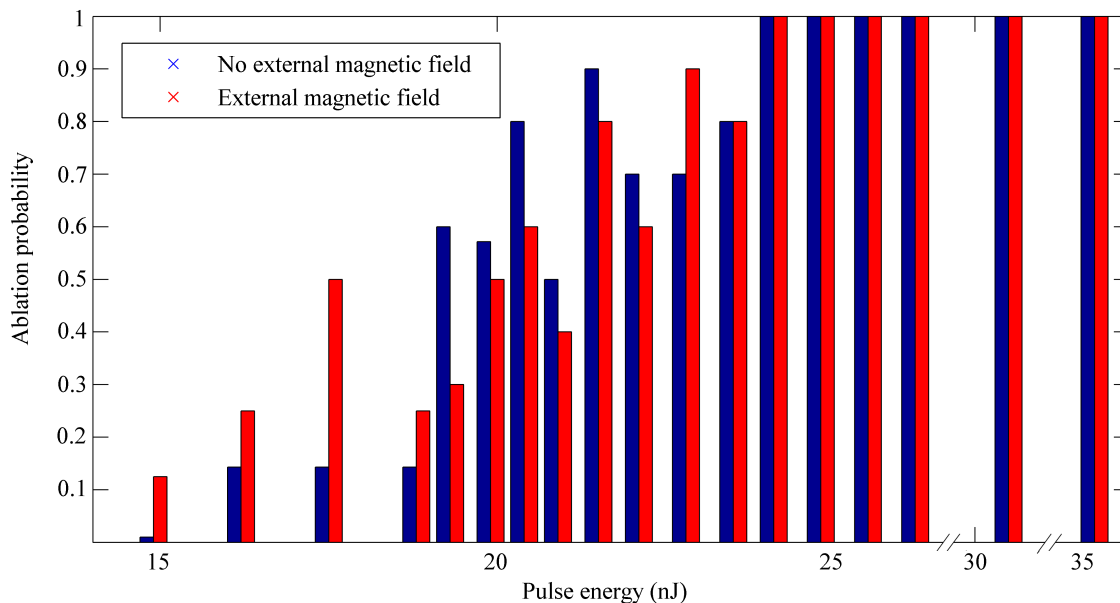


FIGURE 4.28 Comparison between the ablation probability with (red) and without (blue) magnetic field presence for different pulse energies.

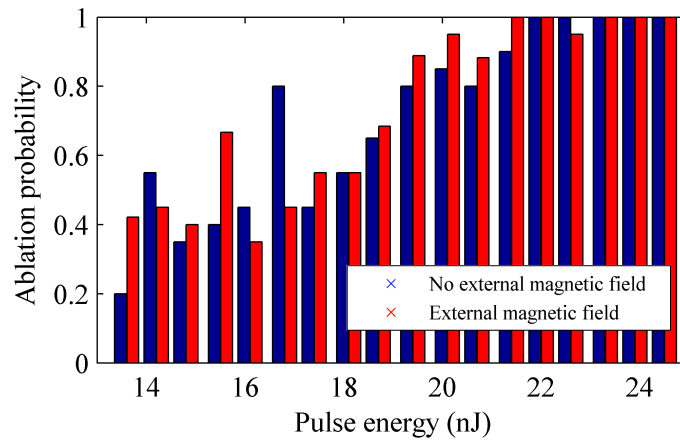


FIGURE 4.29 Comparison between the ablated area with (red) and without (blue) magnetic field presence for different pulse energies.

Once we identified the region where the ablation probability decreased, we studied 18 different pulse energies in smaller energy steps in the range from 13 nJ to 26 nJ. No appreciable difference was observed in ablation behaviour between both cases as shown in Fig.4.29.

In order to investigate possible effects on ablation due to the presence of a magnetic field for over-threshold beam diameters below  $1\ \mu\text{m}$ , we repeated the experience in section 4.5 with and without presence of an external magnetic field. CVD monolayer graphene on glass substrate was irradiated with zero-th order Bessel beam of 130 fs pulse duration and  $\rho_0 = 0.5\ \text{mm}$  corresponding to a tilt angle of  $26^\circ$ . We processed five matrices consisting in 400 single shot illuminated sites each matrix. The energies of the different matrices were 2.9 nJ, 4.1 nJ, 5.4 nJ, 7.3 nJ and 10.0 nJ. From the beam scan in air we determined that peak fluence of  $139\ \text{mJ}/\text{cm}^2$ , i.e. the fluence ablation threshold, corresponded to a pulse energy of 4.1 nJ, hence no ablation was expected for pulse energies of 2.9 nJ and 4.1 nJ, and for higher pulse energies we figure there would be graphene ablation.

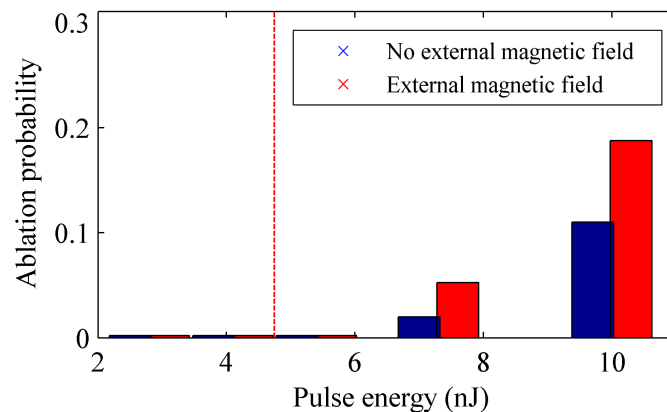


FIGURE 4.30 Comparison between the ablated area with (red) and without (blue) presence of magnetic field for different pulse energies with peak fluence close to the ablation threshold. Red line indicates separates energies below (left) and above (right) ablation threshold.



Statistical study of the patterned sample after characterization at the SEM, showed that there was no ablation for pulse energies 2.9 nJ, 4.1 nJ and 5.4 nJ, even if the peak fluence of the latter is above the ablation threshold. This result was consistent with our results in section 4.2, where we explained the deviation in the threshold model through the high free-carrier diffusion in graphene. Fig.4.30 shows the ablation probability for higher pulse energies with and without external magnetic field.

In conclusion, after investigating single shot patterning of CVD monolayer graphene on glass substrate in a wide range of energies from far above ablation fluence threshold to just below it with and without presence of an external magnetic field of  $B \sim 0.45$  T. No significant difference was observed in ablation probability nor ablated area between both cases. Further investigation at higher magnetic field should be carried out to determine possible effects of an external magnetic field on ablation at sub-micron scale which could have been overshadowed in our experiments by other possible constraints in ablation such as processes leading to formation of folded graphene.

#### 4.7/ GRAPHENE NANOSTRUCTURING WITH HIGHER ORDER BESSEL BEAM

Following our line of research we propose the next hypothesis. Different fluence distribution can produce different electronic density distribution in the illuminated region. In zero-th order Bessel beam due to the spot-like illuminated zone, after laser excitation the electronic density will expand and decrease, since it is a ring distribution, the inner part of the ring will expand towards the center which could lead to a high electronic density at the center of the illuminated ring and a subsequent localized graphene ablation in that region.

We followed similar experimental procedure as detailed in previous sections. After characterization of the 1<sup>st</sup> order Bessel beam, the graphene sample was placed at the position corresponding to the peak intensity along propagation with an error of  $0.6 \mu\text{m}$ .

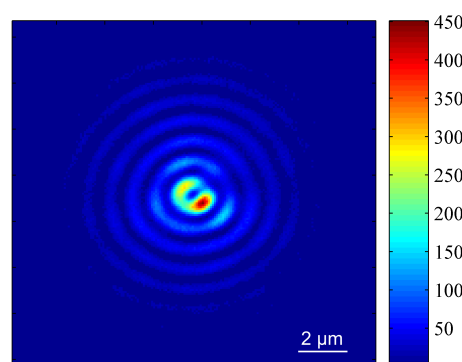


FIGURE 4.31 Transverse fluence map of the first order Bessel beam at its peak intensity plane along propagation for a pulse energy of 29.3 nJ. Fluence colorbar is in  $\text{mJ}/\text{cm}^2$ .

Matrices of illuminated spots were done in the sample applying pulse energies ranging from 3.4 nJ to 24.9 nJ. A total of 400 identically illuminated spots were investigated for each different pulse energy. After laser processing the sample was characterized by SEM.

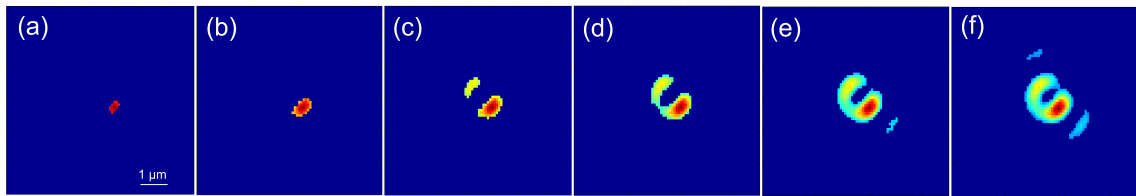


FIGURE 4.32 Fluence map at the sample position after applying ablation fluence threshold of  $139 \text{ mJ/cm}^2$  for pulse energies of (a) 7.3 nJ, (b) 9.5 nJ, (c) 11.8 nJ, (d) 14.8 nJ, (e) 20.3 nJ and (f) 24.9 nJ. The fluence colorscale is different in each figure with increasing peak fluence from (a)  $164 \text{ mJ/cm}^2$  to (f)  $554 \text{ mJ/cm}^2$ .

For pulse energies of  $3.35 \pm 0.14 \text{ nJ}$ ,  $5.02 \pm 0.16 \text{ nJ}$  and  $7.39 \pm 0.12 \text{ nJ}$  there was no ablation. Since the intensity distribution of the first order Bessel beam was not exactly centered as shown in Fig .4.31, for the higher pulse energies investigated we could differentiate between 6 five different types of behaviour for single shot laser processing : no ablation process, ablation of a small spot corresponding to the region of the ring where the intensity was maximum, two small spot at each side of the ring, a complete ablated spot corresponding to the area of the first ring and its inner region, a partially ablated spot where the inner region was not ablated and remained connected to the graphene sheet, and the complete ablation of the first ring and the inner graphene region plus partial ablation of the second ring. Figure 4.33 shows the different ablated morphologies. This results were consistent with over-threshold beam distributions for the different pulse energies as shown in Fig.4.32.

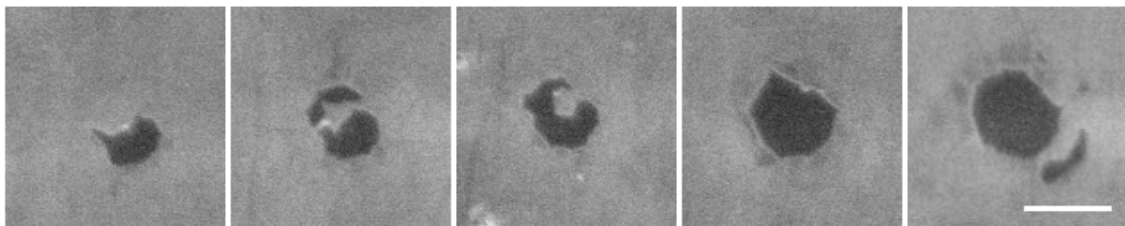


FIGURE 4.33 SEM images of different ablated morphologies using first order Bessel beam with non-radial symmetric intensity distribution. The scale bar indicates  $1 \mu\text{m}$ . All images have the same scale.

Interaction between regions of the ring with different intensity distribution could lead to precise determination of the carrier diffusion length before thermalization. In addition, non-radial symmetric intensity distributions can be of interest for potential graphene applications, e.g.ablation of two semicircles could lead to fabrication of graphene nanochannels.

## 4.8/ CONCLUSIONS

In this chapter we presented the results of the set of experiments we performed to determine the possibilities and constraints of single shot ablation of CVD monolayer graphene with spatially shaped ultrafast laser pulses.

First, we developed a novel technique using non-diffractive beam with an hexagonal array intensity distribution that allowed us to use two different methods to determine the ablation threshold monolayer graphene. The threshold values we obtained with both methods were consistent and also in good agreement with previous results reported by other groups. With this procedure we also observed a deviation in from the threshold model at sub-micron scale. For over-threshold beam diameters below  $1\mu\text{m}$  even if the peak fluence was well above the ablation threshold, no material was removed. From our simulations of the carrier density evolution within the pulse duration we infer this behaviour could be explained by the high carrier diffusion coefficient.

We investigated the possible effects of the polycrystalline structure of CVD monolayer graphene could have on laser ablation at sub-micron scale. Using zero-th order Bessel beam to pattern a graphene sheet we observed that above  $1\mu\text{m}$  over-threshold beam diameters there was a 100 % ablation probability regardless the presence of grain boundaries, meanwhile below that over-threshold diameter, the ablation probability was much higher when there was a grain boundary in the vicinity of the illuminated region. Our results are in good agreement with theoretical predictions of other groups showing a high reduction of electron transmission in grain boundaries. This electronic confinement at the grain boundaries would allow a higher ablation probability despite graphene diffusion coefficient.

We observed no impact on ablation at sub-micron scale when using different dielectric substrate. We also tested potential confinement of electrons when an external magnetic field was applied but no statistically meaningful difference was observed.

In the last part of this chapter we investigated ablation of graphene using higher order Bessel beams and we observed a deviation in ablation probability when decreasing the pulse energy. We determined that deposition of different energy gradient leads to diverse graphene folded petals configurations which could limit minimal size of the ablated features.

## CONCLUSIONS AND PERSPECTIVES

In this thesis we have carried a set of experiments to characterize laser patterning of CVD monolayer graphene at sub-micron scale. Our motivation was the need of a patterning procedure suitable with industrial scale production of graphene-based devices. This procedure should be fast, easily reconfigurable and low cost. In addition it should allow large scale patterning.

We have investigated in which extent single shot patterning using spatially shaped beams could satisfy those requirements.

We developed a novel technique to measure the fluence threshold for ablation independently of the beam size. This allowed us to determine the ablation threshold of CVD monolayer graphene on glass substrate at different pulse durations between 130 fs to 3 ps. Our results were in good agreement with previous reported ablation threshold values. The method we developed appears to be suitable for ablation threshold characterization of any kind of thin films independent of spot size.

Through a statistical study we determined a deviation from the classical ablation model for over-threshold beam diameters below 1  $\mu\text{m}$ . Since the peak fluence was above the ablation threshold, material removal was always expected, however, below this diameter the ablation probability decreased rapidly. Our simulations on the evolution of the carrier density showed this phenomena could be linked to the high carrier diffusion in graphene. Although high carrier diffusion in graphene is a big opportunity in optoelectronic applications, we showed it is an important drawback when laser patterning graphene at sub-micron scale because it hinders the necessary energy confinement for laser ablation.

Graphene layers produced by chemical vapor deposition suits well for graphene-based devices production at industrial scale because sheets up to 1  $\text{m}^2$  is already achievable. This was our motivation to investigate possible effect of the polycrystalline nature of CVD graphene in laser patterning at sub-micron scale. Experimental results showed two different behaviors depending on the presence of a grain boundary in the vicinity of the illuminated region. In the case of a laser pulse incident on a graphene island, the ablation probability shows a step-like behaviour from no ablation below 1  $\mu\text{m}$  over-threshold diameter to 100 % ablation above that diameter. On the other hand, when there is a grain boundary at less than 0.5  $\mu\text{m}$  from the center of the illuminated spot, below over-threshold diameters the ablation probability decreases gradually. Our results could be explained again by electronic confinement of the carriers at the grain boundary which allows for a higher ablation probability in the case of small beam diameters. This results are in good agreement with theoretical studies of other groups showing a high reduction of electron transmission in grain boundaries. This is an inconvenient to control

sub-micron laser patterning of graphene.

To determine possible limitations in minimizing the laser ablated spot size in graphene we investigated the evolution of the ablated features when reducing the over-threshold beam diameter far below  $1\ \mu\text{m}$ . We found that not only the fluence threshold was a key parameter but also the fluence gradient. Different fluence gradient produces distinct graphene folded petals configuration. Folded petals are part of the graphene layer that is not removed by the laser pulse, instead it folds around the ablated spot. For small gradient, ablated spots were larger than the area of the folded graphene and even for over-threshold beam diameters of  $\sim 200\ \text{nm}$  it was not possible to achieve ablated diameters below  $1\ \mu\text{m}$ . On the other hand, for a high fluence gradient, spot diameters down to  $600\ \text{nm}$  were achieved but the ablated spot area were equal to the folded graphene area, meaning that no material was removed. We infer that in case of a high gradient, possible mechanisms leading to formation of folded graphene petals, such as the high mechanical strength of graphene could be an important factor at sub-micron scale during the ablation process overcoming the mechanisms responsible of laser material removal. This results could have a strong impact in single shot patterning of graphene since ablated spots in the order of hundreds of nanometers are achievable but graphene folded petals are unavoidable. However, this could lead to certain applications requiring a fast method to produce graphene folded nanochannels since electrical transport measurements indicating conduction tunneling effects in graphene nanochannels has been previously reported[206].

We also experimentally tested if the potential confinement of free-electrons by a high magnetic field could prevent diffusion but no statistically meaningful difference was observed.

In the last part of this thesis we have investigated graphene ablation under higher order Bessel beams. Even if the beam shape was the same, features with different morphology were patterned depending on the pulse energy. We observed this method is compatible with industrial production of patterned graphene layers when the peak fluence is well above the ablation threshold since the same features were always obtained, meanwhile for peak fluence values close to the threshold the ablation it is a non-deterministic process, for each pulse energy different shapes were ablated with a certain probability. However, for lower pulse energies we patterned interesting features such as graphene nanochannels of a width of  $200\ \text{nm}$  over a length of more than  $1\ \mu\text{m}$  with a single laser shot. Although this last procedure was not suitable for large scale production for patterned features below  $1\ \mu\text{m}$ , it can be a convenient method to produce various features such as nanoribbons in order to study its fundamental properties. It could also be a first approach to characterize the excited carriers diffusion distance in a graphene sheet.

From the actual state-of-the-art and our results we infer the future research guidelines before this method becomes totally functional for industrial scale production should be the following.

First step towards precise controlled sub-micron patterning of graphene should be to clarify the principle leading to the deviation from the classical ablation model when the over-threshold beam diameter is below  $1\ \mu\text{m}$ . We propose a spectral interferometry experiment to determine if the mechanism leading to this deviation is high carrier diffusion or if it is a thermal process, such as phonon relaxation. A setup where a reference pulse, a pump pulse and finally a probe pulse are incident onto the graphene sample could

allow to determine the evolution of the carrier density by controlling the delay between the pump and the probe. In addition this experimental scheme enables studying the redistribution of the absorbed energy since it was clear from our results that different fluence gradient lead to diverse phenomena.

Further investigation is required to determine if there is a minimum ablated feature size in single shot regime, since it could be a main constraint for this method to produce nano-patterned graphene devices. The future research in this direction should determine the mechanism of interaction between graphene and the dielectric substrate leading to folded graphene petals formation and its role as a constraint in ablated feature size.

In addition, nonlinear excitation mechanisms should be estimated in order to determine the impact of the secondary lobes when patterning graphene with Bessel beams.

From an application point of view, once the previous questions will be solved and the patterning of sub-micron features will be controlled, next approaches should be to develop a novel illumination scheme that would generate a similar damage between grain boundaries and graphene islands, in addition to allowing the patterning of areas of graphene in the order of  $1 \text{ m}^2$  in a very short period of time.

Once these requirements will be accomplished, laser patterning of CVD graphene sheets at sub-micron scale could be at the doorstep of its application at industrial scale leading finally to the presence of graphene-based devices in our daily life.



# BIBLIOGRAPHIE

- [1] Novoselov, K. S., Geim ; A.K., Morozov, S.V., Jiang, D., Zhang, Y., Dubonos, S.V., Grigorieva, I.V., and Firsov, A.A. *Electric field effect in atomically thin carbon films*. Science 306, 666 (2004)
- [2] A. K. Geim, and K. S. Novoselov *The rise of graphene* Nature Materials 6, 183 (2007)
- [3] K. Ghaffarzadeh *Graphene, 2D Materials and Carbon Nanotubes : Markets, Technologies and Opportunities 2016-2026*
- [4] W. Steen, and J. Mazumder *Laser Material Processing* ISBN 978-3-540-19670-9, Springer-Verlag Berlin Heidelberg GmbH (2010)
- [5] J. C. Ion *Laser processing of engineering materials* ISBN 978-0-750-66079-2, Elsevier (2005)
- [6] D. Strickland, and G. Mourou *Compression of amplified chirped optical pulses* Optics communications 56, 219 (1985)
- [7] A. B. J. Sullivan, and P. T. Houldcroft *Gas-jet laser cutting* British Welding Journal 14, 443 (1967)
- [8] P. R. Wallace *The band theory of graphite* Physical Reviews 71, 622 (1947)
- [9] A. H. Castro Neto, F. Guinea, N. M. R. Peres, K. S. Novoselov, and A. K. Geim *The electronic properties of graphene*. Reviews of Modern Physics 81, 109 (2009)
- [10] M. I. Katsnelson *Graphene : Carbon in two dimensions* Cambridge University Press (2012)
- [11] S. Reich, C. Thomsen, and J. Maultzsch *Carbon nanotubes : Basic concepts and physical properties* Wiley-VCH Verlag GmbH (2004)
- [12] R. Saito, G. Dresselhaus, and M. S. Dresselhaus *Physical properties of carbon nanotubes* Imperial College, ISBN : 978-1-86094-379-9 (2005)
- [13] M.C. Lemme, T.J. Echtermeyer, M. Baus, and H. Kurz *A graphene field-effect device* IEEE Electron Device Letters 28, 4 (2007)
- [14] S. V. Vonsovsky, and M. I. Katsnelson *Quantum solid-state physics* Springer series in Solid-State Science 73 (1989)
- [15] J. D. Bjorken, and S. D. Drell *Relativistic quantum mechanics* McGraw-Hill (1964)
- [16] V. B. Berestetskii, E. M. Lifshitz, and L. P. Pitaevskii *Relativistic quantum theory* Pergamon Press (1971)
- [17] L. D. Landau, and E. M. Lifshitz *Quantum Mechanics. A Course of Theoretical Physics* Pergamon Press, Volume 3 (1965)
- [18] J. D. Jackson *Classical electrodynamics* John Wiley & Sons (1962)
- [19] K. F. Mak, J. Shan, and T. F. Heinz *Seeing many-body effects in single- and few-layer graphene : Observation of two-dimensional saddle-point excitons* Physical Review Letters 106, 046401 (2011)



- [20] K. F. Mak, M. Y. Sfeir, Y. Wu, C. H. Lui, J. A. Misewich, and T. F. Heinz *Measurement of the optical conductivity of graphene* Physical review Letters 101, 196405 (2008)
- [21] F. Bonaccorso, Z. Sun, T. Hasan, and A. C. Ferrari *Graphene photonics and optoelectronics* Nature photonics 4, 611 (2010)
- [22] Q. Bao, and K. P. Loh *Graphene photonics, plasmonics, and broadband optoelectronic devices* ACS Nano 6, 3677 (2012)
- [23] M. Breusing, S. Kuehn, T. Winzer, E. Malic, F. Milde, N. Severin, J. P. Rabe, C. Ropers, A. Knorr, and T. Elsaesser *Ultrafast nonequilibrium carrier dynamics in a single graphene layer* Physics Review Letters B 83, 153410 (2011)
- [24] E. Malic, T. Winzer, E. Bobkin, and A. Knorr *Microscopic theory of absorption and ultrafast many-particle kinetics in graphene* Physical Review B 84, 205406 (2011)
- [25] S. Luo, Y. Wang, X. Tong, and Z. Wan *Graphene-based optical modulator* Nanoscale Research Letters 10, 199 (2015)
- [26] E. McCann and V. I. Falko *Landau-level degeneracy and quantum Hall effect in a graphite bilayer* Physical Review Letters 96, 086805 (2006)
- [27] E. McCann, D. S.L. Abergel, V. I. Falko *Electrons in bilayer graphene* Solid State Communications 143, 110 (2007)
- [28] K. Nagashio, T. Nishimura, K. Kita and A. Toriumi *Mobility variations in mono- and multi-layer graphene films* Applied Physics Express 2, 025003 (2009)
- [29] M. Koshino *Stacking-dependent optical absorption in multilayer graphene* New Journal of Physics 15, 015010 (2013)
- [30] C. Lee, X. Wei, J.W. Kysar, and J. Hone *Measurement of the elastic properties and intrinsic strength of monolayer graphene* Science 321, 385 (2008)
- [31] A. A. Balandin, S. Ghosh†, W. Bao, I. Calizo, D. Teweldebrhan, F. Miao and C. N. Lau *Superior Thermal Conductivity of Single-Layer Graphene* Nano Letters 8, 902 (2008)
- [32] A. A. Balandin *Thermal properties of graphene and nanostructured carbon materials* Nature Materials 10, 569 (2011)
- [33] S. Chen, A. L. Moore, W. Cai, J. W. Suk, J. An, C. Mishra, C. Amos, C. W. Magnuson, J. Kang, L. Shi, and R. S. Ruoff *Raman measurements of thermal transport in suspended monolayer graphene of variable sizes in vacuum and gaseous environments* ACS Nano 5, 321 (2011)
- [34] B. Qiu, Y. Wang, Q. Zhao, and X. Ruan *The effects of diameter and chirality on the thermal transport in free-standing and supported carbon-nanotubes* Applied Physics Letters 100, 233105 (2012)
- [35] P. A. Denis and F. Iribarne *Comparative Study of Defect Reactivity in Graphene* Journal of Physical Chemistry 117, 19048 (2013)
- [36] C. Melios, A. Centeno, A. Zurutuza, V. Panchal, C. E. Giusca, S. Spencer, S. R. P. Silva, and O. Kazakova *Effects of humidity on the electronic properties of graphene prepared by chemical vapour deposition* Carbon 103, 273 (2016)
- [37] B. Jayasena, C. D. Reddy, and S. Subbiah *Separation, folding and shearing of graphene layers during wedge-based mechanical exfoliation* Nanotechnology 24, 20 (2013)
- [38] B. Jayasena, and S. Subbiah *A novel mechanical cleavage method for synthesizing few-layer graphenes* nanoscale Research Letters 6, 95 (2011)

- [39] M. Quintana, M. Grzelczak, K. Spyrou, B. Kooi, S. Bals, G. Van Tendeloo, P. Rudolf, and M. Prato *Production of large graphene sheets by exfoliation of graphite under high power ultrasound in the presence of tiopronin* Chemical Communications 48, 12159 (2012)
- [40] H. Xu, and K. S. Suslick *Sonochemical Preparation of Functionalized Graphenes* Journal of the American Chemical Society 133, 9148 (2011)
- [41] J. N. Coleman *Liquid Exfoliation of Defect-Free Graphene* Accounts of Chemical Research 46, 14 (2013)
- [42] S. Park, and R. S. Ruoff *Chemical methods for the production of graphenes* Nature nanotechnology 4, 217 (2009)
- [43] Y. Hernandez , V. Nicolosi, M. Lotya, F.M. Blighe, Z. Sun, S. De, T.T. McGovern, B. Holland, M. Byrne, Y.K. Gun'ko, J.J. Boland, P. Nuraj, G. Duesberg, S. Krishnamurthy, R. Goodhue, J. Hutchison, V. Scardaci, A.C. Ferrari, and J.N. Coleman *High-yield production of graphene by liquid-phase exfoliation of graphite* Nature Nanotechnol 3, 563 (2008)
- [44] J.H. Lee, D.W. Shin, V.G. Makotchenko, A.S. Nazarov, V.E. Fedorov, Y.H. Kim, J.Y. Choi, J.M. Kim and J.B. Yoo *One-step exfoliation synthesis of easily soluble graphite and transparent conducting graphene sheets*. Advanced Materials 21, 4383 (2009)
- [45] W.T. Gu, W. Zhang, X.M. Li, H.W. Zhu, J.Q. Wei, Z. Li, Q. Shu, C. Wang, K.L. Wang, W. Shen, F.Y. Kang and D.H. Wu *Graphene sheets from worm-like exfoliated graphite* Journals of Materials Chemistry 19, 3367 (2009)
- [46] <http://www.graphene.ac.rs/lpe.html>
- [47] S. Kataria, S. Wagner, J. Ruhkopf, A. Gahoi, H. Pandey, R. Bornemann, S. Vaziri, A. D. Smith, M. Ostling, and M. C. Lemme. *Chemical vapor deposited graphene : From synthesis to applications*. Physica Status Solidi A 11, 211 (2004)
- [48] B. Pollard. *Growing graphene via chemical vapor deposition*. PhD-Master ? thesis, Pomona College (2009)
- [49] A. Kumar and C. H. Lee *Advances in Graphene Science* Nanotechnology and Nanomaterials, IMTECH, ISBN 978-953-51-1182-5 (2013)
- [50] W. Zhu, T. Low, V. Perebeinos, A. A. Bol, Y. Zhu, H. Yan, J. Tersoff, and P. Avouris *Structure and electronic transport in graphene wrinkles* Nano Letters 12, 3431 (2012)
- [51] V. E. Calado, G. F. Schneider, A. M. M. G. Theulings, C. Dekker, and L. M. K. Vander-sypen *Formation and control of wrinkles in graphene by the wedging transfer method* Applied Physics Letters 101, 103116 (2012)
- [52] Xuesong Li, Weiwei Cai, Jinho An, Seyoung Kim, Junghyo Nah, Dongxing Yang, Richard Piner, Aruna Velamakanni, Inhwa Jung, Emanuel Tutuc, Sanjay K. Banerjee, Luigi Colombo, and Rodney S. Ruoff. *Large-Area Synthesis of High-Quality and Uniform Graphene Films on Copper Foils* . Science 5, 1312 (2009).
- [53] O. V. Yazyev, and S. G. Louie *Electronic transport in polycrystalline graphene* Nature Materials 9, 806 (2010).
- [54] G.-H. Lee, R. C. Cooper, S. J. Ann, S. Lee, A. van der Zande, N. Petrone, A. G. Hammerberg, G. Lee, B. Crawford, W. Oliver, J. W. Kysar, and J. Hone *High-strength Chemical-Vapor-Deposited graphene and grain boundaries* Science 340, 1073 (2013)

- [55] P. Vancsó, G. I. Mark, P. Lambin, A. Mayer, Y.-S. Kim, C. Hwang, and L. P. Biró *Electronic transport through ordered and disordered graphene grain boundaries* Carbon 64, 101 (2013).
- [56] P. Nemes-Incze, P. Vancsó, Z. Osváth, G. I. Máek, X. Jin, Y.-S. Kim, C. Hwang, P. Lambin, C. Chapelier, and L. P. Biró *Electronic states of disordered grain boundaries in graphene prepared by chemical vapor deposition* Carbon 64, 178 (2013).
- [57] N. Liu, Z. Pan, L. Fu, C. Zhang, B. Dai, and Z. Liu *The origin of wrinkles on transferred graphene* Nano Research 4, 996 (2011)
- [58] N. Woehrl, O. Ochedowski, S. Gottlieb, K. Shibasaki and S. Schulz *Plasma-enhanced chemical vapor deposition of graphene on copper substrates* AIP Advances 4, 047128 (2014)
- [59] A. Malesevic, R. Vitchev, K. Schouteden, A. Volodin, L. Zhang, G. van Tendeloo, A. Vanhulsel, and C. Van Haesendonck *Synthesis of few-layer graphene via microwave plasma-enhanced chemical vapour deposition* Nanotechnology 19, 305604 (2008)
- [60] K. H. Lee, B. Lee, S.-J. Hwang, J.-U. Lee, H. Cheong, O.-S. Kwon, K. Shin, N. H. Hur *Large scale production of highly conductive reduced graphene oxide sheets by a solvent-free low temperature reduction* Carbon 69, 327 (2014)
- [61] W. A. de Heer, C. Berger, M. Ruan, M. Sprinkle, X. La, Y. Hua, B. Zhang, J. Hankinson and E. Conrad *Large area and structured epitaxial graphene produced by confinement controlled sublimation of silicon carbide* Proceedings of the National Academy of sciences of the United States 108, 16900 (2011)
- [62] R. M. Tromp and J. B. Hannon *Thermodynamics and Kinetics of Graphene Growth on SiC(0001)* Physical Review Letters 102, 106104 (2009)
- [63] K. V. Emtsev, A. Bostwick, K. Horn, J. Jobst, G. L. Kellogg, L. Ley, J. L. McChesney, T. Ohta, S. A. Reshanov, J. Röhr, E. Rotenberg, A. K. Schmid, D. Waldmann, H. B. Weber and T. Seyller *Towards wafer-size graphene layers by atmospheric pressure graphitization of silicon carbide* Nature Materials 8, 203 (2009)
- [64] E. Moreau, S. Godey, F. J. Ferrer, D. Vignaud, X. Wallart, J. Avila, M. C. Asensio, F. Bournel, and J. J. Gallet *Graphene growth by molecular beam epitaxy on the carbon-face of SiC* Applied Physics Letters 97, 241907 (2010)
- [65] J. Park, W. C. Mitchel, L. Grazulis, H. E. Smith, K. G. Eyink, J. J. Boeckl, D. H. Tomich, S. D. Pacley and J. E. Hoelscher *Epitaxial Graphene Growth by Carbon Molecular Beam Epitaxy (CMBE)* Advanced materials 22, 4140 (2010)
- [66] J. M. Garcia, U. Wurstbauer, A. Levy, L. N. Pfeiffer, A. Pinczuk, A. S. Plaut, L. Wang, C. R. Dean, R. Buizza, A. M. Van Der Zande, J. Hone, K. Watanabe and T. Taniguchi *Graphene growth on h-BN by molecular beam epitaxy* Solid State Communications 152, 975 (2012)
- [67] S. Bae, S. J. Kim, D. Shin, J.-H. Ahn and B. H. Hong *Towards industrial applications of graphene electrodes* Physica Scripta T146, 014024 (2012)
- [68] J. Lee, V. Varshney, J. Park, B. L. Farmer, and A. K. Roy *In silico carbon molecular beam epitaxial growth of graphene on the h-BN substrate : carbon source effect on van der Waals epitaxy*. Nanoscale 8, 9704 (2016)
- [69] F. Banhart, J. Kotakoski, and A. V. Krashenninnikov *Structural defects in graphene*. ACS Nano 5, 26 (2010)

- [70] J. Lahiri, Y. Lin, P. Bozkurt, I. I. Oleynik and M. Batzill *An extended defect in graphene as a metallic wire*. Nature Nanotechnology 5, 326 (2010)
- [71] P. Y. Huang, C. S. Ruiz-Vargas, A. M. van der Zande, W. S. Whitney, M. P. Levendorf, J. W. Kevek, S. Garg, J. S. Alden, C. J. Hustedt, Y. Zhu, J. Park, P. L. McEuen and D. A. Muller *Grains and grain boundaries in single-layer graphene atomic patchwork quilts* Nature 469, 389 (2011)
- [72] Z. Sun, Q. Ye, C. Chi, and J. Wu *Low band gap polycyclic hydrocarbons : from closed-shell near infrared dyes and semiconductors to open-shell radicals* Chemical Society Reviews 41, 7857 (2012)
- [73] A. Krasheninnikov, F. Banhart *Engineering of nanostructured carbon materials with electron or ion beams* Nature Materials 6, 723 (2007)
- [74] A. Krasheninnikov, V. Nordlund *Ion and electron irradiation-induced effects in nano-structured materials* Journal of Applied Physics 107, 071301 (2010)
- [75] P. Nemes-Incze, P. Vancsó, Z. Osváth, G. I. Máek, X. Jin, Y.-S. Kim, C. Hwang, P. Lambin, C. Chapelier, and L. P. Biró *Electronic states of disordered grain boundaries in graphene prepared by chemical vapor deposition*. Carbon 64, 178 (2013).
- [76] H.-B.-R. Lee, J. T. Tanskanen, N. Liu, and C. Pang *Selective metal deposition at graphene line defects by atomic layer deposition*. Nature Communications
- [77] A. Mesaros, S. Papanikolaou, C. F. J. Flipse, D. Sadri, and J. Zaanen *Electronic states of graphene grain boundaries* Physical Review B 85, 205119 (2010)
- [78] N. M. R. Peres, F. Guinea, and A. H. Castro Neto *Electronic properties of disordered two-dimensional carbon* Physical Review B 73, 125411 (2006)
- [79] Y. Hwangbo, C.-K. Lee, S.-M. Kim, J.-H. Kim, K.-S. Kim, B. Jang, H.-J. Lee, S.-K. Lee, S.-S. Kim, J.-H. Ahn, S.-M. Lee *Fracture characteristics of monolayer CVD-graphene* Scientific Reports 4, 4439 (2014)
- [80] G.-H. Lee, R. C. Cooper, S. J. An, S. Lee, A. van der Zande, N. Petrone, A. G. Hammerberg, C. Lee, B. Crawford, W. Oliver, J. W. Kysar, and J. Hone *High-strength Chemical-Vapor-Deposited graphene and grain boundaries* Science 30, 1073 (2013)
- [81] P. Vancsó, G. I. Mark, P. Lambin, A. Mayer, Y.-S. Kim, C. Hwang, and L. P. Biró *Electronic transport through ordered and disordered graphene grain boundaries*. Carbon 64, 101 (2013).
- [82] M. Ahmad, S. A. Han, D. H. Tien, J. Jung, and Y. Seoa *Local conductance measurement of graphene layer using conductive atomic force microscopy* Journal of Applied Physics 110, 054307 (2011)
- [83] A. W. Tsen, L. Brown, M. P. Levendorf, F. Ghahari, P. Y. Huang, R. W. Havener, C. S. Ruiz-Vargas, D. A. Muller, P. Kim, J. Park *Across grain boundaries in polycrystalline graphene* Science 336, 1143 (2012)
- [84] L. Holland, G. Siddall *The properties of some reactively sputtered metal oxide films* Vacuum 3, 375 (1953)
- [85] I. Hamberg and C. G. Granqvist *Evaporated Sn-doped In<sub>2</sub>O<sub>3</sub> films : Basic optical properties and applications to energy-efficient windows* Journal of Applied Physics 60, R123 (1986)
- [86] T. Minami *Transparent conducting oxide semiconductors for transparent electrodes* Semiconductor Science Technology 20, S35 (2005)

- [87] D. R. Sahu, S. Y. Lin, and J. L. Huang *ZnO/Ag/ZnO multilayer films for the application of a very low resistance transparent electrode* Applied Surface Science 252, 7509 (2006)
- [88] M. A. Green, K. Emery, K. Bücher, D. L. King, and S. Igari *Solar cell efficiency tables* Progress in Photonics : Research and Applications 7,321 (1999)
- [89] V. Yong, and J. M. Tour *Theoretical efficiency of nanostructured graphene-based photovoltaics* Small, 6, 313 (2009)
- [90] N. Yang, J. Zhai, D. Wand, Y. Chen, and L. Jiang *Two-dimensional graphene bridges enhanced photoinduced charge transport in dye-sensitized solar cells.* ACS Nano 4, 887 (2010)
- [91] C. G. Granqvist *Transparent conductors as solar energy materials : a panoramic review* Solar Energy Materials and Solar Cells 91,1529 (2007)
- [92] F. Xia, T. Muller, Y.-M. Lin, A. Valdes-Garcia, and P. Avouris *Ultrafast graphene transistor* Nature Nanotechnology 4, 839 (2009)
- [93] S. Thongrattanasiri, F. H. L. Koppens, and F. J. Garcia de Abajo *Complete Optical Absorption in Periodically Patterned Graphene* Physical Review Letters 108, 047401 (2012)
- [94] U. Keller *recent developments in compact ultrafast lasers* Nature 424, 831 (2003)
- [95] T. Hasan, Z. Sun, F. Wang, F. Bonaccorso, P.-H. Tan, A. G. Rozhin, A.C. Ferrari *Nanotube-polymer composites for ultrafast photonics* Advanced Materials 21, 3874 (2009)
- [96] H. Zhang, D. Y. Tang, L. M. Zhao, Q. L. Bao, and K. P. Loh *Large energy mode locking of an erbium-doped fiber laser with atomic layer graphene* Optics Express 17, 17630 (2009)
- [97] H. Zhang, D. Tang, R. J. Knize, L. Zhao, Q. Bao and K. P. Loh *Graphene mode locked, wavelength-tunable, dissipative soliton fiber laser* Applied Physics Letters 96, 111112 (2010)
- [98] Y. W. Song, S. Y. Jang, W. S. Han, and M. K. Bae *Graphene mode-lockers for fiber lasers functioned with evanescent field interaction* Applied Physics lettersd 96, 051122 (2010)
- [99] W. D. Tan, C. Y. Su, R. J. Knize, G. Q. Xie, L. J. Li and D. Y. Tang *Mode locking of ceramic Nd :Yttrium aluminum garnet with graphene as saturable absorber* Applied Physics Letters 96, 031106 (2010)
- [100] Q. Bao, H. Zhang, Y. Wang, Z. Ni, Y. Yan, Z. X. Shen, K. P. Loh, D. Y. Tang *Atomic-layer graphene as saturable absorber for ultrafast pulsed lasers* Advanced Functional Materials 19, 3077 (2010)
- [101] J.A. Pickering *Touch-sensitive screens : the technologies and their applications* International Journal of Man-Machine Studies 25, 249 (1986)
- [102] J. Wang, Y. Chen, and W. J. Blau *Carbon nanotubes and nanotube composites for nonlinear optical devices* Journal of Materials Chemistry 19, 7425 (2009)
- [103] F. Rana *Graphene terahertz plasmon oscillations* IEEE Transactions on Nanotechnology 7, 91 (2008)
- [104] D. Sun, C. Divin, J. Rioux, J. E. Sipe, C. Berger, W. A. de Heer, P. N. First, T. B. Norris *Coherent control of ballistic photocurrents in multilayer epitaxial graphene using quantum interference* Nano Letters 10, 1293 (2010)

- [105] T. Otsuji, H. Karasawa, T. Komori, T. Watanabe, H. Fukidome, M. Suemitsu, A. Satou, V. Ryzhii *Observation of amplified stimulated terahertz emission from optically pumped epitaxial graphene heterostructures* arXiv :1001.5075 [cond-mat.mtrl-sci] (2010)
- [106] L. Du, G. Chen, L. Wang, X. Chen, and W. Lu *Plasmon resonances of terahertz absorption in nano-patterned graphene* 40th International Conference on Infrared, Millimeter, and Terahertz waves (IRMMW-THz) (2015)
- [107] J. J. Dean, and H. M. van Driel *Second harmonic generation from graphene and graphitic films* Applied Physics Letters 95, 261910 (2009)
- [108] E. Hendry, P. J. Hale, J. J. Moger, A. K. Savchenko, and S. A. Mikhailov *Strong nonlinear optical response of graphene flakes measured by four-wave mixing* Applied Physics Letters 95, 261910 (2009)
- [109] M. D. Stoller, S. Park, Y. Zhu, J. An and R. S. Ruoff *Graphene-Based Ultracapacitors* Nano Letters 8, 3498 (2008)
- [110] C. Liu, Z. Yu, D. Neff, A. Zhamu, and B. Z. Jang *Graphene-Based Supercapacitor with an Ultrahigh Energy Density* Nano Letters 10, 4863 (2010)
- [111] L. Zhang, F. Zhang, X. Yang, G. Long, Y. Wu, T. Zhang, K. Leng, Y. Huang, Y. Ma, A. Yu, and Y. Chen *Porous 3D graphene-based bulk materials with exceptional high surface area and excellent conductivity for supercapacitors* Scientific reports 3, 1408 (2013)
- [112] Y. Shao, M. F. El-Kady, L. J. Wang, Q. Zhang, Y. Li, H. Wang, M. F. Mousaviae and R. B. Kaner *Graphene-based materials for flexible supercapacitors* Chemical Society Reviews 44, 3639 (2015)
- [113] S. Han, and B. C. Chun *Preparation of polyurethane nanocomposites via covalent incorporation of functionalized graphene and its shape memory effect* Composites Part a : Applied Science and Manufacturing 58, 65(2014)
- [114] V. Georgakilas, M. Otyepka, A. B. Bourlinos, V. Chandra, N. Kim, K. C. Kemp, P. Hobza, R. Zboril, and K. S. Kim *Functionalization of Graphene : Covalent and Non-Covalent Approaches, Derivatives and Applications* Chemical Reviews 112, 6156 (2012)
- [115] X. Yan, F. Wang, B. Zheng, F. Huang *Stimuli-responsive supramolecular polymeric materials* Chemical Society Review 41, 666 (2012)
- [116] Y. Wang, Z. Li, J. Wang, J. Li, Y. Lin *Graphene and graphene oxide : biofunctionalization and applications in biotechnology* Trends Biotechnology 29, 205 (2011)
- [117] P. Avouris , C. Dimitrakopoulos *Graphene : synthesis and applications* Materials Today 15, 86 (2012)
- [118] Z. Liu, J. T. Robinson, X. Sun and H. Dai *PEGylated Nanographene Oxide for Delivery of Water-Insoluble Cancer Drugs* Journal of the American Chemical Society 130, 10876 (2008)
- [119] X. Sun, Z. Liu, K. Welsher, J. T. Robinson, A. Goodwin, S. Zaric, H. Dai *Nano-Graphene Oxide for Cellular Imaging and Drug Delivery* Nano Research 1, 203 (2008)
- [120] J. T. Robinson, S. M. Tabakman, Y. Liang, H. Wang, H. Sanchez-Casalogue, D. Vinh, and H. Dai *Ultrasmall Reduced Graphene Oxide with High Near-Infrared Absorbance for Photothermal Therapy* Journal of the American Chemical Society 133, 6825 (2011)

- [121] M. Li, X. Yang, J. Ren, K. Qu and X. Qu *Using Graphene Oxide High Near-Infrared Absorbance for Photothermal Treatment of Alzheimer's Disease* *Advanced Materials* 24, 1722 (2012)
- [122] X. Kang, J. Wang, H. Wu, I.A. Aksay, J. Liu, Y. Lin *Glucose oxidase-graphene-chitosan modified electrode for direct electrochemistry and glucose sensing* *Biosensors and Bioelectronics* 25, 901 (2009)
- [123] C. Shan, H. Yang, J. Song, D. Han, A. Ivaska and L. Niu *Direct Electrochemistry of Glucose Oxidase and Biosensing for Glucose Based on Graphene* *Analytical Chemistry* 81, 2378 (2009)
- [124] D. Du, Z. Zou, Y. Shin, J. Wang, H. Wu, M. H. Engelhard, J. Liu, I. A. Aksay and Y. Lin *Sensitive Immunosensor for Cancer Biomarker Based on Dual Signal Amplification Strategy of Graphene Sheets and Multienzyme Functionalized Carbon Nanospheres* *Analytical Chemistry* 82, 2989 (2010)
- [125] Y. Xie, A. Chen, D. Du, Y. Lin *Graphene-based immunosensor for electrochemical quantification of phosphorylated p53 (S15)* *Analytica Chimica Acta* 699, 44 (2011)
- [126] K. P. Loh, Q. Bao, G. Eda, M. Chhowalla *Graphene oxide as a chemically tunable platform for optical applications* *Nature Chemistry* 2, 1015 (2010)
- [127] Z. Liu, Q. Liu, Y. Huang, Y. Ma, S. Yin, X. Zhang, W. Sun, and Y. Chen *Organic Photovoltaic Devices Based on a Novel Acceptor Material : Graphene* *Advanced Materials* 20, 3924 (2008)
- [128] Z. Tang, H. Wu, J. R. Cort, G. W. Buchko, Y. Zhang, Y. Shao, I. A. Aksay, J. Liu, Y. Lin *Constraint of DNA on functionalized graphene improves its biostability and specificity* *Small* 6, 1205 (2010)
- [129] M. Zhang, L. Bai, W. Shang, W. Xie, H. Ma, Y. Fu, D. Fang, H. Sun, L. Fan, M. Han, C. Liub and S. Yang *Facile synthesis of water-soluble, highly fluorescent graphene quantum dots as a robust biological label for stem cells* *Journal of Materials Chemistry* 22, 7461 (2012)
- [130] J. Peng, W. Gao, B. K. Gupta, Z. Liu, R. Romero-Aburto, L. Ge, L. Song, L. B. Alemany, X. Zhan, G. Gao, S. A. Vithayathil, B. A. Kaipparattu, A. A. Marti, T. Hayashi, J.-J. Zhu, and P. M. Ajayan *Graphene Quantum Dots Derived from Carbon Fibers* *nano Letters* 12, 844 (2012)
- [131] C. Hu, Y. Liu, Y. Yang, J. Cui, Z. Huang, Y. Wang, L. Yang, H. Wang, Y. Xiao, and J. Rong *One-step preparation of nitrogen-doped graphene quantum dots from oxidized debris of graphene oxide* *Journal of Materials Chemistry B* 1, 39 (2013)
- [132] S. Zhu, J. Zhang, C. Qiao, S. Tang, Y. Li, W. Yuan, B. Li, L. Tian, F. Liu, R. Hu, H. Gao, H. Wei, H. Zhang, H. Sunb and B. Yang *Strongly green-photoluminescent graphene quantum dots for bioimaging applications* *Chemical Communications* 47, 6858 (2011)
- [133] W. Chen, P. Yi, Y. Zhang, L. Zhang, Z. Deng, and Z. Zhang *Composites of Aminodextran-coated Fe<sub>3</sub>O<sub>4</sub> nanoparticles and graphene oxide for cellular magnetic resonance imaging* *ACS Applied Materials and Interfaces* 3, 4085 (2011)
- [134] H. Hong, K. Yang, Y. Zhang, J. W. Engle, L. Feng, Y. Yang, T. R. Nayak, S. Goel, J. Bean, C. P. Theuer, T. E. Barnhart, Z. Liu, and W. Cai *In-vivo targeting and imaging of tumor vasculature with radiolabeled, antibody-conjugated nanographene*

- [135] A. Y. Romanchuk, A. S. Slesarev, S. N. Kalmykov, D. V. Kosynkin, J. M. Tour *Graphene oxide for effective radionuclide removal* Physical Chemistry Chemical Physics 15,2321 (2013)
- [136] D. Cohen-Tanugi, and J. C. Grossman *Water desalinization across nanoporous graphene* Nano Letters 12, 3602 (2012)
- [137] D. Cohen-Tanugi, and J. C. Grossman *Water permeability of nanoporous graphene at realistic pressures for reverse osmosis desalination* The journal of Chemical Physics 141, 074704 (2014)
- [138] D. Cohen-Tanugi, and J. C. Grossman *Mechanical Strength of Nanoporous Graphene as a Desalination Membrane* Nano Letters 14, 6171 (2014)
- [139] R. J. Blaikie, D. O.S. Melville and M. M. Alkaisi *Super-resolution near-field lithography using planar silver lenses* Microelectronic Engineering 83, 723 (2006)
- [140] C. Vieu, F. Carcenac, A. Pepin, Y. Chen, M. Mejias, A. Lebib, L. Manin-Ferlazzo, L. Couraud, and H. Launois *Electron beam lithography : resolution limits and applications* Applied Surface Science 164 111 (2000)
- [141] X. Liang, Z.i Fu, and S. Y. Chou *Graphene transistors fabricated via transfer-printing in device active-areas on large wafer* Nano Letters 7, 3840 (2007)
- [142] H. R. Khaleel, H. M. Al-Rizzo, and A. I. Abbosh *Design, Fabrication, and Testing of Flexible Antennas, Advancement in Microstrip Antennas with Recent Applications* InTech, DOI : 10.5772/50841 (2013)
- [143] S. Prezioso, F. Perrozzi, M. Donarelli, F. Bisti, S. Santucci, L. Palladino, M. Nardone, E. Treossi, V. Palermo, and L. Ottaviano *Large area extreme-UV lithography of graphene oxide via spatially resolved photoreduction* Langmuir 28, 5489 (2012)
- [144] C. Wang, K. J. Morton, Z. Fu,W.-D. Li, and S. Y. Chou *Printing of sub-20 nm wide graphene ribbon arrays using nanoimprinted graphite stamps and electrostatic force assisted bonding* Nanotechnology 22, 445301 (2011)
- [145] S. Kemme *Microoptics and nanooptics fabrication* CRS Press (2009)
- [146] A. A. Tseng, K. Chen, C. D. Chen, and K. J. Ma *Electron beam lithography in nanoscale fabrication : recent development* IEEE Transactions on electronics packaging manufacturing 26, 141 (2003)
- [147] B. Sommer, J. Sonntag, A. Ganczarczyk, D. Braam, G. Prinz, A. Lorke, and M. Geller *Electron-beam induced nano-etching of suspended graphene* Scientific Reports 5, 7781 (2015)
- [148] I. Childres, L. A. Jauregui, M. Foxe, J. Tian, R. Jalilian, I. Jovanovic, and Y. P. Chen *Effect of electron-beam irradiation on graphene field effect devices* Applied Physics Letters 97, 173109 (2010)
- [149] Z. J. Qi, J. A. Rodríguez-Manzo, S. J. Hong, Y. W. Park, E. A. Stach, Marija Drndić, and A. T. Charlie Johnson *Direct electron beam patterning of sub-5nm monolayer graphene interconnects* SPIE Proceedings 8680, Alternative Lithographic Technologies V (2013)
- [150] C. Thiele, A. Felten, T. J. Echtermeyer, A. C. Ferrari, C. Casiraghi, H. v. Löhneysen, and R. Krupke *Electron-beam-induced direct etching of graphene* Carbon 64, 84 (2013)
- [151] D. C. Bell *Nanoscale engineering and e-beam lithography using (S)TEM* Microscopy and Microanalysis 13, 532 (2007)



- [152] X. Wang and Y. Shi *Fabrication techniques of graphene nanostructures* Nanofabrication and its application in renewable energy 1, 1 (2014)
- [153] Jon Orloff, L. W. Swanson and M. Utlaut *Fundamental limits to imaging resolution for focused ion beams* Journal of Vacuum Science and Technology B 14, 3759 (1996)
- [154] V. Castaldo, C. W. Hagen, B. Rieger and P. Kruit *Sputtering limits versus signal-to-noise limits in the observation of Sn balls in a Ga<sup>2</sup> microscope* Journal of Vacuum Science and Technology B 26, 2107 (2008)
- [155] J. Kotakoski, C. Brand, Y. Lilach, O. Cheshnovsky, C. Mangler, M. Arndt, and J. C. Meyer *Toward two-dimensional all-carbon heterostructures via ion beam patterning of single-layer graphene* Nano Letters 15, 5944 (2015)
- [156] B. S. Archanjo, A. P. M. Barboza, B. R. A. Neves, L. M. Malard, E. H. M. Ferreira, J. C. Brant, E. S. Alves, F. Plentz, V. Carozo, B. Fragneaud, I. O. Maciel, C. M. Almeida, A. Jorio, and C. A. Achete *The use of a Ga<sup>+</sup> focused ion beam to modify graphene for device applications* Nanotechnology 23, 25 (2012)
- [157] A. Hemamouche, A. Morin, E. Bourhis, B. Toury, E. Tarnaud, J. Mathé, P. Guégan, A. Madouri, X. Lafosse, C. Ulysse, S. Guilet, G. Patriarche, L. Auvray, F. Montel, Q. Wilmart, B. Plaçais, J. Yates, and J. Gierak *FIB patterning of dielectric, metallized and graphene membranes : A comparative study* Microelectronics Engineering 121, 87 (2014)
- [158] L. Scipioni, L.A. Stern, J. Notte, S. Sijranddij, and B.J. Griffin *Helium ion microscope* Advanced Materials Processing 166, 27 (2008)
- [159] R.S. Averbeck, and M. Ghaky *A model for Surface Damage in Ion-Irradiated Solids* Journal of Applied Physics 76, 3908 (1994)
- [160] J. Zeigler, J. Biersack, U. Littmark *The stopping range of ions in matter* Treatise on heavy-ion science 6, 93 (1985)
- [161] D.C. Bell, M.C. Lemme, L. A. Stern, J.R. Williams, and C. M. Marcus *Precision cutting and patterning of graphene with helium ions* Nanotechnology 20, 455301 (2009)
- [162] M. C. Lemme, D. C. Bell, J. R. Williams, L. A. Stern, B. W. H. Baugher, P. Jarillo-Herrero, and C. M. Marcus *Etching of graphene devices with a Helium ion beam* ACS Nano 3, 2674 (2009)
- [163] V. Iberi, I. Vlassioux, X.-G. Zhang, B. Matola, A. Linn, D. C. Joy, and A.J. Rondinone *Maskless lithography and in situ visualization of conductivity of graphene using Helium ion microscopy* Scientific Reports 5, 11952 (2015)
- [164] B. N. Chichkov, C. Momma, S. Nolte, F. von Alvensleben, A. Tünnermann *Femtosecond, picosecond and nanosecond laser ablation of solids* Applied Physics A 63, 109 (1996)
- [165] S. K. Sundaram, and E. Mazur *Inducing and probing non-thermal transitions in semiconductors using femtosecond laser pulses* Nature Materials 1, 217 (2002)
- [166] R. R. Gattass, and E. Mazur *Femtosecond laser micromachining in transparent materials* Nature photonics 2, 219 (2008)
- [167] I. Martín-Fabiani, S. Riedel, D. R. Rueda, J. Siegel, J. Boneberg, T. A. Ezquerro, and A. Nogales *Micro- and submicrostructuring thin polymer films with two and three-beam single pulse laser interference lithography* American Chemical Society 30, 8973 (2014)

- [168] K. Sugioka, and Y. Cheng *Ultrafast lasers reliable tools for advanced materials processing* Light : Science Applications 3, 149 (2014)
- [169] M. Gladwell *The tipping point : How little things can make a big difference* Back Bay Books (2000)
- [170] M. Malinauskas, A. Zukauskas, S. Hasegawa, Y. Hayasaki, V. Mizeikis, R. Buividas, and S. Juodkazis *Ultrafast laser processing of materials : from science to industry* Light : Science and Applications 5, 1633 (2016)
- [171] J.-H. Seo, J. H. Park, S.-I. Kim, B. J. Park, Z. Ma, J. Choi, and B.-K. Ju *Nanopatterning by laser interference lithography : Applications to optical devices* Journal of Nanoscience and Nanotechnology 14, 1521 (2014)
- [172] A. F. Lasagni, and B. S. Menéndez-Ormaza *Two-and three-dimensional micro-and sub-micrometer periodic structures using two-beam laser interference lithography* Advanced Engineering Materials 12, 54 (2010)
- [173] J. L. Stay, G. M. Burrow, and T. K. Gaylord *Three-beam interference lithography methodology* Review of Scientific Instruments 82, 023115 (2011)
- [174] X. Xiao, T. E. Beechem, M. T. Brumbach, T. N. Lambert, D. J. Davis, J. R. Michael, C. M. Washburn, J. Wang, S. M. Brozik, D. R. Wheeler, D. B. Burckel, and R. Polsky *Lithographically defined three-dimensional graphene structures* ACS Nano 6, 3573 (2012)
- [175] S. M. Eaton, H. Zhang, P. R. Herman, F. Yoshino, L. Shah, J. Bovatsek, and A. Y. Ara *Heat accumulation effects in femtosecond laser-written waveguides with variable repetition rate* Optics Express 13, 4708 (2012)
- [176] G. Kalita, L. Qi, Y. Namba, K. Wakita, and M. Umeno *Femtosecond laser induced micropatterning of graphene film* Materials Letters 65, 1569 (2011)
- [177] R. Sahin, E. Simsek, and S. Akturk *Nanoscale patterning of graphene through femtosecond laser ablation* Applied Physics Letters 104, 053118 (2014)
- [178] B. Wetzal, C. Xie, P.-A. Lacourt, J. M. Dudley, and F. Courvoisier *Femtosecond laser fabrication of micro and nano-disks in single layer graphene using vortex Bessel beams* Applied Physics Letters 103, 241111 (2013)
- [179] R. J. Stoehr, R. Kolesov, K. Xia, and J. Wrachtrup *All-optical high-resolution nanopatterning and 3D suspending of graphene* ACS Nano 5, 5141 (2011)
- [180] A. Roberts, D. Cormode, C. Reynolds, T. Newhouse-Ilige, B. J. LeRoy, and A. Sandhu *Response of graphene to femtosecond high-intensity laser irradiation* Applied Physics Letters 99, 051912 (2011)
- [181] A. Mathis *Génération de faisceau accélérants : études numériques, expérimentales, et application à l'ablation laser*. PhD Thesis
- [182] P. K. Velpula *High aspect ratio sub-micron structuring of transparent materials using non-diffractive ultrafast laser beams : dynamics and interaction regimes*. PhD Thesis
- [183] P. Wu, C. Sui, and W. Huang *Theoretical analysis of a quasi-Bessel beam for laser ablation*. Photon Res. 2, 2327(2014)
- [184] V. Jarutis, R. Paskauskas, and A. Stabinis *Focusing of Laguerre-Gaussian beams by axicon* Optics Communications 184, 105 (2000)
- [185] J. de Boor, N. Geyer, U. Gösele, and V. Schmidt *Three-beam interference lithography : upgrading a Lloyd's interferometer for single-exposure hexagonal patterning*. Optics letters, 34, 1738 (2009)

- [186] H. Tetlow, J. Posthuma de Boer, I.J. Ford, D.D. Vvedensky, J. Coraux, L. Kantorovich *Growth of epitaxial graphene : Theory and experiment*. Physics Reports 542, 195 (2014)
- [187] N. Sanner, O. Utéza, G. Coustillier, A. Leray, T. Itina, and M. Sentis *Measurement of femtosecond laser-induced damage and ablation thresholds in dielectrics* Applied Physics A, 94, 889 (2009)
- [188] B. Mangote, L. Gallais, M. Zerrad, F. Lemarchand, L. H. Gao, M. Commandré, and M. Lequime *A high accuracy femto-/picosecond laser damage test facility dedicated to the study of optical thin films* Review letters, 83, 013109 (2012)
- [189] L. Mercadier, D. M. Rayner, and P. B. Corkum *Control of femtosecond laser ablation of thin films from a dielectric surface by nonlinear interaction with the substrate* Physical Review Applied, 2, 034001 (2014)
- [190] D. Giguère, G. Olivié, F. Vidal, S. Toetsch, G. Girard, T. Ozaki, and J.-C. Kieffer *Laser ablation threshold dependence on pulse duration for fused silica and corneal tissues : experiments and modeling* Journal of the Optical society of America A 24, 1562 (2007)
- [191] F. Courvoisier, P.-A. Lacourt, M. Jacquot, M. K. Bhuyan, L. Furfaro, and J. M. Dudley *Surface nanoprocessing with nondiffracting femtosecond Bessel beams* Optics Letters, 34, 3163 (2009)
- [192] A. Gil-Villalba, C. Xie, R. Salut, L. Furfaro, R. Giust, M. Jacquot, P. A. Lacourt, J. M. Dudley, and F. Courvoisier *Deviation from threshold model in ultrafast laser ablation of graphene at sub-micron scale* Applied Physics Letters, 107 ; 061103 (2015)
- [193] B. Wetzel, C. Xie, P.-A. Lacourt, J. M. Dudley, and F. Courvoisier *Femtosecond laser fabrication of micro and nano-disks in single layer graphene using vortex Bessel beams* Applied Physics Letters, 103, 241111 (2013)
- [194] J.-H. Yoo, J. B. Park, S. Ahn, and C. P. Grigoropoulos *Laser-induced direct graphene patterning and simultaneous transferring method for graphene sensor platform* Applied Physics Letters, 100, 233124 (2012)
- [195] R. Sahin, S. Akturk, and E. Simsek *Nanoscale patterning of graphene through femtosecond laser ablation* Applied Physics Letters, 104, 053118 (2014)
- [196] A. Roberts, D. Cormode, C. Reynolds, T. Newhouse-Ilige, B. J. LeRoy, and A. Sandhu *Response of graphene to femtosecond high-intensity laser irradiation* Applied Physics letters, 99, 051912 (2011)
- [197] M. Breusing, C. Ropers, and T. Elsaesser *Ultrafast Carrier Dynamics in Graphite* Physical Review Letters, 102, 086809 (2009)
- [198] L. Froehly, M. Jacquot, P. A. Lacourt, J. M. Dudley, and F. Courvoisier *Spatiotemporal structure of femtosecond Bessel beams from spatial light modulators* Journal of Optical Society of America A 31, 790 (2014)
- [199] J. B. Ashcom, R. R. Gattass, C. B. Schaffer, and E. Mazur *Numerical aperture dependence of damage and supercontinuum generation from femtosecond laser pulses in bulk fused silica* Journal of Optical Society of America B 23, 2317 (2006)
- [200] S. Martin, A. Hertwig, M. Lenzner, J. Krüger, and W. Kautek *Spot-size dependence of the ablation threshold in dielectrics for femtosecond laser pulses* Applied Physics A, 77, 883 (2003)

- [201] B. A. Ruzicka, S. Wang, J. Liu, K.-P. Loh, J. Z. Wu, and H. Zhao *Spatially resolved pump-probe study of single-layer graphene produced by chemical vapor deposition* Optical materials Express, 2, 164523 (2012)
- [202] B. A. Ruzicka, S. Wang, L. K. Werake, B. Weintrub, K. P. Loh, and H. Zhao *Hot carrier diffusion in graphene* Physical Review B, 82, 195414 (2010)
- [203] J. Noack and A. Vogel *Laser-induced plasma formation in water at nanosecond to femtosecond time scales : Calculation of thresholds, absorption coefficients, and energy density* IEEE Journal of quantum electronics, 35, 9197 (1999)
- [204] R. Sahin, S. Akturk, and E. Simsek *Quantifying the quality of femtosecond laser ablation of graphene* Applied Physics A 116, 555 (2014)
- [205] J.-H. Yoo, J. B. In, J. B. Park, H. Jeon and C. P. Grigoropoulos *Graphene folds by femtosecond laser ablation* Applied Physics Letters 100, 233124 (2012)
- [206] I. Silvestre, A. W. Barnard, S. P. Roberts, P. L. McEuen, and R. G. Lacerda *Folded graphene nanochannels via pulsed patterning of graphene* Applied Physics Letters 106, 153105 (2015)



# TABLE DES FIGURES

1.1	from [9]. Honeycomb lattice made out of two interpenetrating triangular lattices (left) and its corresponding Brillouin zone (right). The Dirac cones are located at K and K' points. . . . .	12
1.2	from [9]. Electronic dispersion in the honeycomb lattice. Left : energy spectrum (in units of $\gamma_0$ ) for values of $\gamma_0 \sim 2.8$ eV and $\gamma'_0 \sim -0.2 \gamma_0$ . Right : zoom in of the energy bands close to one of the Dirac points. . . . .	13
1.3	from [9]. Density of states per unit cell as a function of energy (in units of $\gamma_0$ ) computed from the energy dispersion. . . . .	15
1.4	Interband optical transitions between filled states (red) and empty states (yellow) in (a) p-doped, (b) undoped graphene and (c) n-doped. Graphene doping level varies the permitted transitions . . . . .	16
1.5	from [19]. Experimental optical conductivity (solid line) and the universal optical conductivity defined in the previous section(dashed line) of monolayer graphene in the spectral range of 0.2 - 5.5 eV. The experimental peak energy is 4.62 eV. Note the deviation of the optical conductivity from the universal value at low energies is attributed to spontaneous doping [20]. . .	17
1.6	from [23]. (a) Graphene layer on mica structure. Incident probe light hits the surface at an angle $\alpha = 35^\circ$ . (b) Linear band structure of graphene, arrow indicating pumped and probed optical transitions at the same wavelength. (c) Spectrally integrated transmission change (points) as a function of pump-probe delay. Solid line : biexponential fit. Gray line : cross correlation of pump and probe pulses. Inset : linear dependence of the maximum transmission change on pump fluence. . . . .	17
1.7	from [24]. (a) Coulomb- and (b) phonon-induced scattering channels along the linear band structure of graphene. Intra- and interband as well as intra- and intervalley processes are taken into account. . . . .	18
1.8	from [24]. Temporal evolution of the angle-averaged carrier distribution $[\rho_k$ weighted by the density of states $D(\omega)$ ] as a function of energy. The relaxation dynamics is determined by Coulomb- and phonon-induced intra- and interband scattering channels. It is characterized by (a) an ultrafast thermalization followed by (b) cooling of the optically excited carriers. . . . .	19
1.9	from [25]. Processes of saturable absorption in graphene. (a) Optical interband excited by incident light. (b) The photogenerated carriers redistribute a Fermi-Dirac distribution. (c) Further absorption is blocked under sufficient intensity of incident light. . . . .	20
1.10	from [30]. Schematic of nanoindentation test on suspended graphene membrane. . . . .	21

1.11 (a) Reflection and (b) transmission image of graphene flakes produced by scotch tape method under x40 magnification optical microscope. Different grayscale color correspond to a different number of graphene layers. . . . .	22
1.12 from [37]. Schematic diagram for wedge-based mechanical exfoliation of a few layers of graphene. . . . .	23
1.13 from [46]. Schematic liquid phase exfoliation technique to produce graphene. . . . .	23
1.14 from [49]. Schematic diagram of the transfer process to an arbitrary substrate. . . . .	24
1.15 from [50]. Three different wrinkle morphologies : (a) simple ripple geometry, (b) standing collapse wrinkle, and (c) folded geometry wrinkle. . . . .	25
1.16 from [67]. Comparison between four representative methods to obtain graphene films. . . . .	27
1.17 from [69]. Stone-Wales defect, formed by rotating a carbon-carbon bond by 90°. (a) Experimental TEM image of the defect ; (b) its atomic structure as obtained from density functional theory (DFT) calculations. (c) Zigzag (red) and armchair (blue) edge configurations of graphene [72]. . . . .	29
1.18 from [82]. SEM image of graphene layer by CVD graphene shows the formation of wrinkles and individual grain domains with grain boundaries as darker lines. . . . .	30
1.19 from ref. [21]. Schematic of a graphene-based photodetector. . . . .	32
1.20 from ref.[21]. (a) Schematic of a capacitive touchscreen. (b) Resistive graphene-based touch screen. . . . .	33
1.21 from ref.[136]. Schematic of a graphene desalination membrane. . . . .	35
2.1 from [142]. Scheme of the chemical etching (photolithography) process. . . . .	37
2.2 from [144]. SEM images of (a) UV nanoimprinted graphene nanoribbons array transferred onto SiO <sub>2</sub> wafer and (b) a layer of graphene sheet attached to graphene nanoribbons array. . . . .	38
2.3 from [155]. (a) SEM image of TEM grid showing an array of holes with diameters of 2.5 $\mu\text{m}$ . Graphene layer covers the whole area and is suspended over the holes. Visible dark stripes correspond to patterned graphene at a dose of 4.96 pC/nm <sup>2</sup> . (b) TEM image of pattern written at a dose of 15.2 pC/nm <sup>2</sup> showing completely removed graphene in white. . . . .	40
2.4 from [157] SEM images of (a) an 8 nm drilled pore in a mechanically exfoliated graphene flake and (b) a 9 nm drilled pore on CVD growth graphene sheet. . . . .	41
2.5 from [162]. Helium ion microscope image (with false color) of a suspended graphene device after etching with minimum feature sizes of about 10 nm (color online). . . . .	41
2.6 from [161]. Schematic of the interactions of primary energetic He ions with a graphene layer on SiO <sub>2</sub> substrate, showing the production of secondary electrons (SE <sub>I</sub> at the primary beam and SE <sub>II</sub> at the secondary scattered ion exiting the surface), back scattered ions and secondary ions. . . . .	42

2.7	from [164]. Comparison between (a) femtosecond and (b) nanosecond pulse ablated hole in steel. . . . .	43
2.8	from [165]. Timescales of various electron and lattice processes in laser-excited solids. Each green bar represents an approximate range of characteristic times over a range of carrier densities from $10^{17}$ to $10^{22}$ $\text{cm}^{-3}$ . Yellow colored region corresponds to optical excitation duration in the range $\sim 1 - 100$ fs . . . . .	43
2.9	from [165]. Electron and lattice excitation and relaxation processes in a laser-excited direct gap semiconductor. CB is the conduction band and VB the valence band. (a) Multiphoton absorption. (b) Free-carrier absorption. (c) Impact ionization. (d) Carrier distribution before scattering. (e) Carrier-carrier scattering. (f) Carrier-phonon scattering. (g) Radiative recombination. (h) Auger recombination. (i) Diffusion of excited carriers. (j) Thermal diffusion. (k) Ablation. (l) Resolidification or condensation . . . . .	44
2.10	Schematic ablation threshold in a typical gaussian intensity laser distribution.	45
2.11	from [172]. Calculated intensity distribution for (a) two-beam, (b) three-beam, and (c) four-beam interference patterning. The geometrical configurations of the beams necessary to achieve the displayed geometries are also shown. . . . .	45
2.12	from [177]. (a) SEM and (b) optical microscope images of a femtosecond laser ablated stripes on a single layer of graphene. Lighter regions are ablated parts. . . . .	46
2.13	from [193]. SEM images of (a) microdisk and (b) nanodisk obtained from ablation by 20 superimposed vortex Bessel beam exposures. . . . .	47
2.14	from [179]. AFM images of graphene nanoribbons of (a) 80 nm and (b) 35 nm width. The inset shows schematically the $\text{TEM}_{10}$ laser beam profile used for patterning. . . . .	47
3.1	Scheme of experimental setup used to image the beam in air removing the graphene sample and to pattern the graphene sheet. . . . .	50
3.2	Block diagram for the laser system. . . . .	51
3.3	Scheme of the Phazzler FROG working principle. . . . .	52
3.4	(a) Experimental FROG trace and (b) reconstruction of the pulse for pulse duration of 100 fs. . . . .	52
3.5	Experimental power values (blue) and fitting corresponding to a beam waist value of 4.50 mm. . . . .	53
3.6	The principle of knife edge method. . . . .	54
3.7	Typical pulse energy characterization at the sample site as a function of the applied command voltage at the Pockels cells. . . . .	54
3.8	Schematic SLM configuration. . . . .	56
3.9	from [181]. Schematic phase modulation principle using a SLM showing the difference in phase produced by two adjacent pixels. . . . .	56



3.10 (a) from [183] schematic of a quasi-Bessel beam generation with an axicon. (b) Phase mask implemented in the SLM in order to generate a zeroth-order Bessel beam from an incident gaussian beam. The color scale has 256 levels corresponding to phase shift values between 0 and $2\pi$ . No tilt term is applied in this phase mask. . . . .	58
3.11 (a) Phase mask loaded at the SLM to generate the three-beam interference pattern. From [185] (b) three-beam interference geometry and (c) three-beam interference pattern intensity. . . . .	59
3.12 The periodicity of the intensity peaks in the interference pattern is constant along the propagation axis even if the respective intensities slowly evolves. . . . .	59
3.13 Numerical (blue) and analytical (red) interference pattern periodicity as a function of the tilt angle for fixed energy pulse, beam diameter and pulse duration. . . . .	60
3.14 Experimental setup. The lens and microscope objective form a 4f telescope that demagnifies the beam and increases the waves crossing angle. Spatial filtering allows for eliminating unmodulated zero-th order from the Spatial Light Modulator (SLM). . . . .	60
3.15 Images of the beam intensity scanned in air for periodicity (a) 0.16 mm, (b) 0.24 mm, (b) 0.32 mm and (d) 0.40 mm. . . . .	61
3.16 Experimentally measured periodicity of the interference pattern at the sample position as a function of the tilt angle at the machining region. Red line corresponds to the analytical expression. . . . .	62
3.17 Comparison between the experimental (red) and theoretical (blue) on axis intensity of the Bessel beam along propagation for a tilt angle of $\alpha = 26^\circ$ . Inset shows the scanned image of the Bessel beam at the intensity peak plane. . . . .	63
3.18 Experimental scanned Bessel beam in air (a) along propagation axis, (b) transversal profile at the sample, and (c) its corresponding simulation for a tilt angle of $\alpha = 26^\circ$ . . . . .	64
3.19 Theoretical Bessel beam on-axis fluence for pulse energy of 20 nJ and tilt angle of $26^\circ$ (blue) and $9^\circ$ (red). . . . .	65
3.20 Experimental Bessel beam on-axis fluence for pulse energy of 20 nJ and tilt angle of $26^\circ$ (blue) and $9^\circ$ (red). . . . .	65
3.21 Intensity profile of the beam scanned in air corresponding to transversal plane number 51 for incident pulse energy $E_p = 1\mu\text{J}$ for 130 fs pulse. Units are in $10^{12} \text{ W/cm}^2$ . . . . .	66
3.22 Transversal intensity beam profile used to determine the onset of the interference region. Blue spot indicates the onset of the interference region (red). Red arrows indicates propagation direction of the different beam sectors. . . . .	68
3.23 (a) Reflected and (b) transmission microscope images of adhesive tape exfoliated graphene sample. . . . .	69

3.24	Comparison of nanoholes in CVD graphene film when ETD voltage is (a) 1 kV and (b) 5 kV. . . . .	70
4.1	Comparison of fluence distribution over threshold (a) with the SEM image of the damage (b) for a given intensity distribution, pulse duration (130 fs), and input pulse energy (1.3 $\mu$ J). . . . .	73
4.2	Beam image (top) applying an increasing fluence threshold from left to right, and the corresponding correlation map between the over-threshold map and the SEM ablated sample (bottom). In the correlation map, green color indicates matching between the fluence map above the threshold and the image of the ablated sample. Red and blue colors indicate mismatch corresponding to a lower and higher threshold values, respectively. The scale bar indicates 5 $\mu$ m. . . . .	74
4.3	Correlation between the processed sample image and the scanned beam image applying different fluence thresholds, for a given pulse duration (130 fs) and input pulse energy (1.3 $\mu$ J). . . . .	75
4.4	Image of the spatial distribution of the residues : green color for matching areas, red (resp. blue) for areas where the fluence is higher (resp. lower) than the threshold but ablation did not occur (resp. did occur). This image corresponds to the peak of the correlation in Fig.4.3 for a fluence threshold of $(139 \pm 7)$ mJ/cm <sup>2</sup> . . . . .	75
4.5	Direct measurement of the scanned beam intensity at the ablated contour. .	76
4.6	Comparison between the ablation threshold in monolayer graphene for different pulse duration determined by the best matching over different fluence thresholds technique (red) and by the mean fluence at the ablated contour (blue). . . . .	76
4.7	Tracking same illuminated zones in the correlation map along 5 single shots in identical conditions. The scale bar indicates 5 $\mu$ m. . . . .	77
4.8	Over-threshold beam diameter comparison between two pulses with same beam shape but different pulse energy. Red line indicates the ablation fluence threshold. . . . .	78
4.9	Probability of ablation in a disk as a function of the beam diameter above the fluence threshold for a pulse duration of 130 fs (blue), 1 ps (green), and 3 ps (red). Error bars show one standard deviation. For the largest diameters, the ablation probability is actually 100% of our tests, resulting in zero-width error bar. . . . .	78
4.10	Evolution of free carrier density within 100 fs for an initial beam diameter of (a) 400 nm and (b) 2 $\mu$ m. Each blue line corresponds to a time step of 10 fs. .	79
4.11	SEM image of non-patterned CVD monolayer graphene on glass substrate. Dark lines are grain boundaries due to the polycrystalline nature of CVD graphene. . . . .	80
4.12	Pulse energy calibration as a function of the voltage at the Pockels cell. The average error for each pulse energy measurements was $\pm 0.25$ nJ. . .	81

4.13 (a) Analytical transverse fluence profile at the sample position for an incident pulse energy $E_p = 10$ nJ. Red line indicates graphene ablation fluence threshold of $139 \text{ mJ/cm}^2$ and the corresponding over-threshold beam diameter is $0.75 \mu\text{m}$ . (b) Over-threshold beam diameter for pulse duration of 130 fs at different pulse energies. . . . .	81
4.14 SEM image of matrix of equidistant laser illuminated spots with zero-th order Bessel beam with pulse energies of (a) 20.0 nJ and (b) 10.0 nJ. Red circles indicates illuminated but non-ablated sites and green circles indicates illuminated and ablated sites. Correlation between ablated holes and grain boundaries is obvious for the lower pulse energy. Difference in grayscale between both images corresponds to different voltage used at the SEM. . . . .	82
4.15 Ablation probability comparison between illuminated site in a graphene island (red) and in the vicinity of a grain boundary (blue). . . . .	83
4.16 SEM image of matrix of equidistant 400 laser illuminated spots with pulse energy 10.0 nJ. Crossing white lines are the illuminated ablation sites. Top and bottom lines of ablated holes are reference lines patterned at 20.0 nJ where the ablation probability is 100%. The white colour of the ablated holes is due to the voltage applied at the SEM. . . . .	84
4.17 Ablation probability comparison between CVD monolayer graphene on glass substrate (blue) and on quartz substrate (red) for a pulse duration of 130 fs and different pulse energies. . . . .	85
4.18 Ablated area comparison between CVD monolayer graphene on glass substrate (blue) and on quartz substrate (red) for a pulse duration of 130 fs and different pulse energies. . . . .	85
4.19 Analytical fluence distribution of the Bessel beam at the sample position for pulse energy of 20 nJ and tilt angle of $26^\circ$ (blue) and $9^\circ$ (red). Black dashed lines corresponds to graphene ablation fluence threshold. . . . .	86
4.20 Experimentally characterized over-threshold fluence beam and SEM images of ablated holes for a pulse energy of 20.0 nJ for tilt angle of (top) $9^\circ$ and (bottom) $26^\circ$ . White scale bar corresponds to $1 \mu\text{m}$ . All images are at the same scale. . . . .	86
4.21 Measured areas of ablated spots (blue) and folded graphene petals (red) for a tilt angle of $9^\circ$ . Each value corresponds to the average of 3 measured spots for each over-threshold diameter. . . . .	87
4.22 Measured areas of ablated spots (blue) and folded graphene petals (red) for a tilt angle of $9^\circ$ (dots) and $26^\circ$ (crosses). Dashed line corresponds to a $1 \mu\text{m}$ diameter. . . . .	88
4.23 (a) Ring magnet and (b) rod magnet configuration. . . . .	89
4.24 (a) Rod and (b) ring magnetic field as a function of the distance from the magnet surface. Red dashed line indicates the graphene layer distance to the magnet surface. . . . .	90
4.25 Scheme of the sample and magnet positioning system. . . . .	90

4.26 Comparison between the ablated area with (red) and without (blue) magnetic field presence for different pulse energies in the range from 100 nJ up to 650 nJ. . . . .	91
4.27 Comparison between the ablated area with (red) and without (blue) magnetic field presence for different pulse energies in the range from 32 nJ up to 100 nJ. . . . .	92
4.28 Comparison between the ablation probability with (red) and without (blue) magnetic field presence for different pulse energies. . . . .	92
4.29 Comparison between the ablated area with (red) and without (blue) magnetic field presence for different pulse energies. . . . .	93
4.30 Comparison between the ablated area with (red) and without (blue) presence of magnetic field for different pulse energies with peak fluence close to the ablation threshold. Red line indicates separates energies below (left) and above (right) ablation threshold. . . . .	93
4.31 Transverse fluence map of the first order Bessel beam at its peak intensity plane along propagation for a pulse energy of 29.3 nJ. Fluence colorbar is in $\text{mJ}/\text{cm}^2$ . . . . .	94
4.32 Fluence map at the sample position after applying ablation fluence threshold of $139 \text{ mJ}/\text{cm}^2$ for pulse energies of (a) 7.3 nJ, (b) 9.5 nJ, (c) 11.8 nJ, (d) 14.8 nJ, (e) 20.3 nJ and (f) 24.9 nJ. The fluence colorscale is different in each figure with increasing peak fluence from (a) $164 \text{ mJ}/\text{cm}^2$ to (f) $554 \text{ mJ}/\text{cm}^2$ . . . . .	95
4.33 SEM images of different ablated morphologies using first order Bessel beam with non-radial symmetric intensity distribution. The scale bar indicates $1 \mu\text{m}$ . All images have the same scale. . . . .	95



# LISTE DES TABLES

3.1	Ratio between measured powers with different OD compared with the measurement without filters. . . . .	55
3.2	Technical characteristics of the SLM serie X8267. . . . .	57







## Résumé :

Depuis sa découverte expérimentale en 2004, le graphène a émergé comme un matériau potentiel pour les technologies de nouvelle génération. Le graphène était le premier matériau 2D produit et l'intérêt qu'il suscite provient de ses remarquables propriétés: il possède d'importants coefficients de mobilité électronique et de conductivité thermique, il est également le matériau le plus solide et léger connu. Pour permettre le développement d'applications à l'échelle industrielle, des technologies de structuration à l'échelle sub-micronique sont nécessaires.

Cette thèse se concentre sur l'exploration de l'ablation par laser femtoseconde en tant que technique de structuration rapide et peu coûteuse de structuré graphène obtenu par technique CVD (Chemical Vapor Deposition). L'utilisation d'impulsions laser ultrabrèves est a priori intéressante en raison de la capacité des impulsions laser ultrabrèves à déposer au sein des matériaux une quantité élevée d'énergie dans un volume extrêmement confiné.

Nous avons réalisé un ensemble d'expériences à partir de faisceaux non-diffractants pour caractériser les paramètres requis pour contrôler l'ablation à l'échelle sub-micronique. Nous avons déterminé les caractéristiques de l'ablation en régime mono-coup pour le graphène CVD, tels que le seuil d'ablation et la probabilité d'ablation. Pour cela, nous avons développé une nouvelle technique de mesure indépendante du seuil indépendante de la taille de la zone ablatée. Nous avons ainsi pu mettre en évidence un écart par rapport au modèle classique d'ablation, l'effet des différents substrats diélectriques, ainsi que le rôle des joints de grain. Nos résultats montrent que l'ablation mono-coup par impulsion femtoseconde est une technique efficace pour des structures au-delà d'une taille caractéristique de  $1\ \mu\text{m}$ , mais en dessous de cette dimension, de nouvelles stratégies d'illuminations se révèlent encore nécessaires.

**Mots-clés :** Graphène, Ablation, Laser femtoseconde

## Abstract:

Since its isolation in 2004, graphene has emerged as a potential material for next generation technologies. Graphene was the first truly 2D material produced. The interest in this material is due to its outstanding properties: graphene is the lightest and strongest material known. It has a large electronic mobility and thermal conductivity. To enable the development of technological applications at industrial scale, fast patterning techniques, operable at sub-micron scale are needed.

This thesis focuses on the requirement of a fast, easily reconfigurable, low cost method to pattern graphene. The aim of our research is to determine the possibilities and constraints of ultrafast laser ablation of CVD graphene at sub-micron scale. Using ultrafast laser to pattern graphene layers is interesting due to the ability of femtosecond laser pulses to accurately depositing a high energy density in confined regions.

We performed a set of experiments using non-diffractive shaped-beams to characterize the parameters required to control laser material processing at such small scale. We determined laser patterning characteristics on CVD monolayer graphene such as the ablation threshold and the ablation probability. To this aim, we have developed a novel technique to measure ablation threshold that is independent of the ablated size and reported unexpected deviation from the threshold model, we also investigated the influence of different dielectric substrates and the effect of the presence of graphene grain boundaries. From our experimental results we conclude that direct single shot laser patterning is a very effective method to pattern features above  $1\ \mu\text{m}$ , but below this dimension, novel illumination strategies are needed.

**Keywords:** Graphene, Ablation, Femtosecond laser

